

Photometry of outer Solar System objects from the Dark Energy Survey II: a joint analysis of trans-Neptunian absolute magnitudes, colors, lightcurves and dynamics

PEDRO H. BERNARDINELLI , GARY M. BERNSTEIN , T. M. C. ABBOTT, M. AGUENA, S. S. ALLAM , D. BROOKS , A. CARNERO ROSELL , J. CARRETERO , L. N. DA COSTA, M. E. S. PEREIRA, T. M. DAVIS , J. DE VICENTE , S. DESAI , H. T. DIEHL , P. DOEL, S. EVERETT, B. FLAUGHER , J. FRIEMAN , J. GARCÍA-BELLIDO , E. GAZTANAGA , R. A. GRUENDL, G. GUTIERREZ , K. HERNER , S. R. HINTON, D. L. HOLLOWOOD, K. HONSCHEID , D. J. JAMES , K. KUEHN , O. LAHAV , S. LEE, J. L. MARSHALL , J. MENA-FERNÁNDEZ , R. MIQUEL , J. MYLES, A. A. PLAZAS MALAGÓN , S. SAMUROFF, E. SANCHEZ , B. SANTIAGO, I. SEVILLA-NOARBE , M. SMITH , E. SUCHYTA , G. TARLE , D. L. TUCKER , V. VIKRAM, A. R. WALKER , N. WEAVERDYCK,

(THE *DES* COLLABORATION)

ABSTRACT

To the extent that the physical properties of trans-Neptunian objects (TNOs) are determined before any migration, we can attempt to connect members of present-day TNO dynamical classes to their regions of birth by studying the classes’ distribution of physical properties. For the well-defined sample of 696 TNOs with absolute magnitudes $5.5 < H_r < 8.2$ detected in the Dark Energy Survey (DES), we characterize the relationships between their dynamical state and their physical properties—namely H_r , indicative of size; their colors $c = \{g - r, r - i, i - z\}$, indicative of surface composition; and their semi-amplitude A of flux variation, indicative of asphericity and surface inhomogeneity. We seek “birth” physical distributions $p_\beta(H_r, c, A)$ that can recreate all the distribution of these parameters in every dynamical class d as a mixture $p_d = \sum_\beta f_{\beta|d} p_\beta$ with fractions $f_{\beta|d}$. We first show that the observed colors of all 696 are consistent with arising from 2 Gaussian distributions in *griz* space, “near-IR bright” (NIRB) and “near-IR faint” (NIRF), presumably arising from an inner and outer birth population, respectively, quantifying the trend seen by Fraser et al. (2023). We find that the DES TNOs favor a model in which the H_r and A distributions of NIRF-colored objects are independent of their current dynamical state, and likewise for NIRB objects, supporting the assignment of NIRF and NIRB as birth populations. All objects are consistent with a common $p(H_r)$ that departs from a power law, but NIRF objects are significantly more time-variable. Cold classical (CC) TNOs are purely NIRF while hot classical (HC), scattered, and detached TNOs are consistent with $\approx 70\%$ NIRB, and

there are significant variations among resonances’ NIRB fractions. The NIRB component of HC TNOs (and of some resonances) have broader inclination distributions than the NIRF, *i.e.* the current dynamical state (inclination distribution) retains information about birth location. We also find potential evidence for radial stratification within the birth NIRB population, in that HC NIRBs are on average redder than detached or scattered NIRBs, and a similar effect distinguishes CC NIRF objects from dynamically excited NIRFs. We estimate total object counts and masses of each dynamical class’s members within our H_r range. These results will strongly constrain models of planetesimal formation and migration in the outer solar system.

1. INTRODUCTION

The present-day population of trans-Neptunian objects (TNOs) can be grouped into broadly defined classes of dynamical behavior (Gladman et al. 2008; Khain et al. 2020; Gladman & Volk 2021), with only the low-inclination ($I < 5^\circ$) *cold classicals* (CC) at semi-major axes $42 < a < 48$ AU believed to have been formed near their current heliocentric distance. The other dynamical classes include: the *resonant* population, trapped in mean motion resonances with Neptune; the *scattering* population, currently undergoing significant evolution in a , primarily because their lower perihelia expose them to significant dynamical influence from Neptune; the *hot classical* (HC) population, at higher inclinations than the CC’s in the $39 < a < 49$ region between the 3:2 and 2:1 mean-motion resonances with Neptune; and the *detached* population, with larger semi-major axes that are not experiencing any significant dynamical perturbations from any of the known planets. Most scenarios for the origin of these dynamical classes have them populated by objects created in quiescent orbits at heliocentric distances $\lesssim 42$ AU, and scattered into higher-excitation orbits by Neptune as it migrates outward to its current position (see review by Morbidelli & Nesvorný 2020).

This scenario is supported not just by dynamical modeling, but by observations of the physical properties of the TNOs. The photometric colors of TNOs are indicative of their surface composition. The bulk abundances of the TNOs will depend on the location of their formation within the protoplanetary disk that formed the Solar System; if surface processing is independent of heliocentric distance after any dynamical migrations begin, then surface colors will retain memory of the region of origin.

The color diversity of TNOs became clear from the first measurements of their colors by Luu & Jewitt (1996), Tegler & Romanishin (1998) and Jewitt & Luu (2001). Subsequent surveys have identified strong correlation between dynamical state and color; in particular, the CCs are seen to be exclusively red, in contrast to a mix of redder and bluer objects among the HCs and other classes (Tegler & Romanishin 2000; Doressoundiram et al. 2001; Trujillo & Brown 2002). Correlations between color and inclination have been extensively revisited in the literature for the distinct dynamical populations of the trans-Neptunian region (*e.g.* Peixinho et al. 2015; Marsset et al. 2019, 2023). There have been multiple attempts at creating a taxonomical classification for TNO colors, with two (Fraser & Brown 2012; Tegler et al. 2016; Wong & Brown 2017), three (Pike et al. 2017) and four (Barucci et al. 2001, 2005; Fulchignoni et al. 2008) color classes proposed out of small samples of optical and near-IR data, while Dalle Ore et al. (2013) combined color and albedo to suggest 10 distinct taxa. Recent detailed investigations, including a large sample of near-IR colors, by Fraser et al. (2023), suggests two sequences in the visible-NIR color space, with CC’s exclusively resident in one space.

In parallel with the study of TNO colors, the absolute magnitude distribution, a proxy for the size distribution, of the TNO populations has also been extensively studied. This distribution is known to transition from a steeper to a shallower behavior at diameters of roughly 100 km (Bernstein et al. 2004; Fraser et al. 2014; Lawler et al. 2018; Kavelaars et al. 2021; Napier et al. 2024) for the distinct trans-Neptunian populations. To date, Wong & Brown (2017) has been the only attempt at constraining TNO H distributions as a function of color, finding $n(H)$ for $7.5 \lesssim H \lesssim 9.5$ to be indistinguishable between dynamically cold and hot populations.

Further evidence of a distinct formation history for the CCs from the dynamically excited populations is the absence of large bodies ($H_r \lesssim < 5.5$, Napier & Adams 2022) from the CCs, also noted early in the study of TNOs (Bernstein et al. 2004; Petit et al. 2011; Kavelaars et al. 2021). Most recently, Bernardinelli et al. (2023) demonstrated that the CC’s have a distinct distribution of light-curve semi-amplitude A from the HCs, with higher variability (suggesting less-spherical shapes) for the CC’s within a fixed range of H_r .

In this work, we extend the work of Bernardinelli et al. (2023) to examine the joint distributions $p_d(H_r, c, A)$ of absolute magnitude (indicating size), color(s) c (surface composition), and light-curve amplitude (shape) of the 696 TNOs with $5.5 < H_r < 8.2$ found in different dynamical classes d by the Dark Energy Survey (DES, Bernardinelli et al. 2022). We will treat these physical properties purely as “birthmarks” tagging their heliocentric distance of formation, rather than investigating the physics of the formation or surface properties themselves. Since migration processes should be independent of the physical properties, we can, ideally, identify distributions $p_\beta(H_r, c, A)$ of physical properties that are characteristic of regions $\beta = \{1, 2, \dots\}$ of *birth*. Determining the coefficients $f_{\beta|d}$ such that $p_d = \sum_\beta f_{\beta|d} p_\beta$ would then indicate what fraction of each *dynamical* class originated at each formation distance range.

The DES sample is the best available for such studies at present, because it is the only large sample with well-defined selection function for which multi-band, multi-epoch observations are available for every object, as well as complete determination of dynamical state (i.e. orbital parameters) and variability estimates (i.e. lightcurve amplitudes). Bernardinelli et al. (2022) detail the detection process and selection function for TNOs in the DES—of particular note is that the selection function is largely independent of color or variability. Bernardinelli et al. (2023) produce photometric measurements D_i for TNO i consisting of flux measurements in the *griz* bands and their statistical uncertainties, from which they derive a posterior probability $p(H_r, c, A|D_i)$ for the physical observables of each object conditioned on its observations. These probability distributions are realized as “measurement swarms”—the results of a Monte Carlo sampling from the posterior probability for H_r, c , and A under an assumption of uniform prior on the mean fluxes of the source.

The principal goal of this paper is to determine the minimal number of distinct physical distributions N_β required to be consistent with the full sample of DES objects in all dynamical classes d . The known discrepancies between the CCs’ and the excited populations’ distributions of color, size, and variability require that $N_\beta \geq 2$. If each β is indeed the birthmark of a distinct formation distance, then the $f_{\beta|d}$ will tell us the distribution of formation distances for the TNOs that ended up in each dynamical class—a powerful constraint on scenarios for the dynamical evolution of the outer solar system, and potentially a constraint on models of the physics of planetesimal formation as well.

The largest TNOs are known to have color and albedo distributions that are quite distinct from smaller objects (Brown 2012), perhaps due to frost cycles, differentiation, and other processes clearly

evidenced by New Horizons observations of Pluto and Charon (Stern et al. 2015). Bernardinelli et al. (2023) also definitively detect lower photometric variability for larger objects. For these reasons we will restrict this paper’s analysis to a fixed, relatively narrow range of $5.5 < H_r < 8.2$, to keep size dependence from being confused with any trends of physical properties with formation region.

In Section 2, we find the Gaussian mixture model (GMM) which best describes the intrinsic distribution of the full DES TNO sample in the space of $g-r$, $r-i$, and $i-z$ colors. A GMM represents a distribution as a sum of multivariate normal distributions. There we find that the color distribution of the DES TNOs as a whole can be adequately fit as the sum of two Gaussian distributions, which we call “near-IR faint” (NIRF) and “near-IR bright” (NIRB) because of their relative i and z -band brightnesses for fixed $g-r$ visible color. These closely resemble the two color sequences proposed from independent data by Fraser et al. (2023). Our NIRB/NIRF families, like the two defined in Fraser et al. (2023), project onto visible colors to reproduce the “red/blue” bimodality identified in earlier work, but the inclusion of a NIR band better separates them. Section 3 presents a mathematical framework that enables the study of statistical properties (such as TNO size distribution slopes and the distribution of lightcurve amplitudes) to broadly defined “families” of objects. We then proceed in Section 4 to assess whether we can derive just two physical distributions $q_{\text{NIRF}}(H_r, c, A)$ and $q_{\text{NIRB}}(H_r, c, A)$, such that each dynamical class is constructed from a mixture of these two distributions. Section 5 assesses whether there is evidence in the DES catalog for $N_\beta > 2$ distinguishable physical components among the dynamical classes, *i.e.* evidence for further stratification of birth properties that has not yet been erased by dynamical mixing. Section 6 discusses the distribution of physical classes vs inclination, and derives population estimates for the distinct trans-Neptunian physical populations. Section 7 discusses our findings, and places them into the context of previous results and potential physical scenarios. We summarize our results in Section 8. The appendices give details of the statistical algorithms used in this work: Appendix A describes the optimization of the GMM in the presence of measurement errors and selection functions, Appendix B describes our approach to computing Bayesian evidence ratios, Appendix C presents our Hamiltonian Monte Carlo approach to sampling the complicated parameter space of our model, and Appendix D presents our strategy for deriving completeness estimates for our sample.

2. THE COLOR DISTRIBUTION OF THE TRANS-NEPTUNIAN REGION

We wish to model the underlying color distribution for TNOs, *i.e.* before any selection or noise, implied by our TNO sample. To this end, we will posit that the underlying distribution for the colors \mathbf{c} is a mixture model given by a combination of K components. For a general measurement \mathbf{x} in d dimensions, we have that the mixture model is

$$p(\mathbf{x}|\boldsymbol{\theta}) = \sum_{\alpha=1}^K f_\alpha p(\mathbf{x}|\boldsymbol{\theta}_\alpha), \quad (1)$$

where the α^{th} component is described by a probability distribution $p(\mathbf{x}|\boldsymbol{\theta}_\alpha)$, and the parameters $\boldsymbol{\theta} = \bigcup_\alpha \{\boldsymbol{\theta}_\alpha, f_\alpha\}$ are subject to the constraint $\sum_\alpha f_\alpha = 1$ to ensure that $p(\mathbf{x}|\boldsymbol{\theta})$ is normalized. In a *Gaussian* mixture model (GMM), the probability distribution $p(\mathbf{x}|\boldsymbol{\theta}_\alpha)$ is a multivariate Gaussian with mean $\boldsymbol{\mu}_\alpha$ and covariance matrix $\boldsymbol{\Sigma}_\alpha$, that is,

$$p(\mathbf{x}|\boldsymbol{\theta}_\alpha) = \mathcal{N}(\mathbf{x}|\boldsymbol{\mu}_\alpha, \boldsymbol{\Sigma}_\alpha) \equiv \frac{1}{\sqrt{(2\pi)^d \det(\boldsymbol{\Sigma}_\alpha)}} \exp \left[-\frac{1}{2} (\mathbf{x} - \boldsymbol{\mu}_\alpha)^\top \boldsymbol{\Sigma}_\alpha^{-1} (\mathbf{x} - \boldsymbol{\mu}_\alpha) \right]. \quad (2)$$

In our case the data space is $\mathbf{x} = (g - r, r - i, i - z)$. The output of the Markov chain executed in [Bernardinelli et al. \(2023\)](#) for each TNO yields a sample of its probability density over \mathbf{x} . Strictly for purposes of deriving the most likely GMM, we approximate this measurement probability as a normal distribution with mean and covariance equal to the mean and covariance matrix of the TNO’s samples; once the GMM components are defined, all other analyses in this paper use the measurement-error uncertainties defined by the Markov chain samples.

Appendix A describes our variant of the GMM method which optimizes the intrinsic distribution in the presence of known uncertainties and selection effects applied to each measurement. We also discuss there the algorithm’s method for selecting the number K of components to allow in the model. The derivation of the color selection function is described in Appendix D.

2.1. Resulting model

Applying the GMM method to all 800+ DES TNOs,¹ and testing $K \in [1, 50]$, the model robustly converges to a two-component model, independent of whether the color selection function is included in the training procedure. Before proceeding, we wish to determine if there are any objects whose colors are inconsistent with the model. Outliers would lead to a wider Σ_α [see Equation (A11)]. To investigate whether there are any such outliers, we need to determine a likelihood that any particular TNO’s measurements could have arisen from a member of a given component α of the mixture. Our target TNO’s measurement errors are defined by the samples $\{\mathbf{c}_j\}$, $1 \leq j \leq N_{\text{samp}}$, from its Markov chain. We first define a metric

$$\mathcal{L}_\alpha \equiv \frac{1}{N_{\text{samp}}} \sum_j p_\alpha(\mathbf{c}_j | \mu_\alpha, \Sigma_\alpha), \quad (3)$$

the mean probability of the color samples being drawn from the mixture component α in the absence of measurement errors. We compare the source’s \mathcal{L}_α value to the values that would be generated by objects drawn from the mixture. To do this, we first create the color uncertainty distribution $\{\Delta\mathbf{c}_j\} \equiv \{\mathbf{c}_j - \bar{\mathbf{c}}\}$ of differences between the chain values and their mean color $\bar{\mathbf{c}}$. Then we sample synthetic “truth” colors $\tilde{\mathbf{c}}_k$ ($k = 1, \dots, N_{\text{sim}}$) from $p_\alpha(\mathbf{c} | \mu_\alpha, \Sigma_\alpha)$ and compute

$$\mathcal{L}_{k,\alpha} = \frac{1}{N_{\text{samp}}} \sum_j p_\alpha(\tilde{\mathbf{c}}_k + \Delta\mathbf{c}_j | \mu_\alpha, \Sigma_\alpha) \quad (4)$$

yielding a value of \mathcal{L} that would be produced from a member of the mixture subject to measurement errors. We can derive a p -value by measuring the fraction of the N_{sim} draws yielding $\mathcal{L}_{k,\alpha} \leq \mathcal{L}_\alpha$. If indeed the measurement errors in color space were independent of the truth color of the source, then the p -value of objects drawn from mixture α would be uniformly distributed between 0 and 1.

We identify a first round of outliers as the 22 TNOs for which $p \leq 0.01$ for *both* mixture components. We then repeat the training procedure for the GMM parameters while excluding these outliers from the sample, keeping the number of components fixed, and ignoring the selection effects, which are seen to be unimportant. This yields our best estimates of the GMM parameters describing the intrinsic color distribution, which are given in Table 1. A visualization of this model is presented in Figure 1.

¹ The physical+dynamical analyses will be restricted to 696 of these sources that are not color outliers and lie within a specific range of H_r .

Note that the fractions f_α in the two components in the Table are given for the sample as a whole, and will depend upon how many members of each dynamical group are present in the training sample. We derive debiased estimates of the intrinsic fractions for each dynamical class in Section 4.

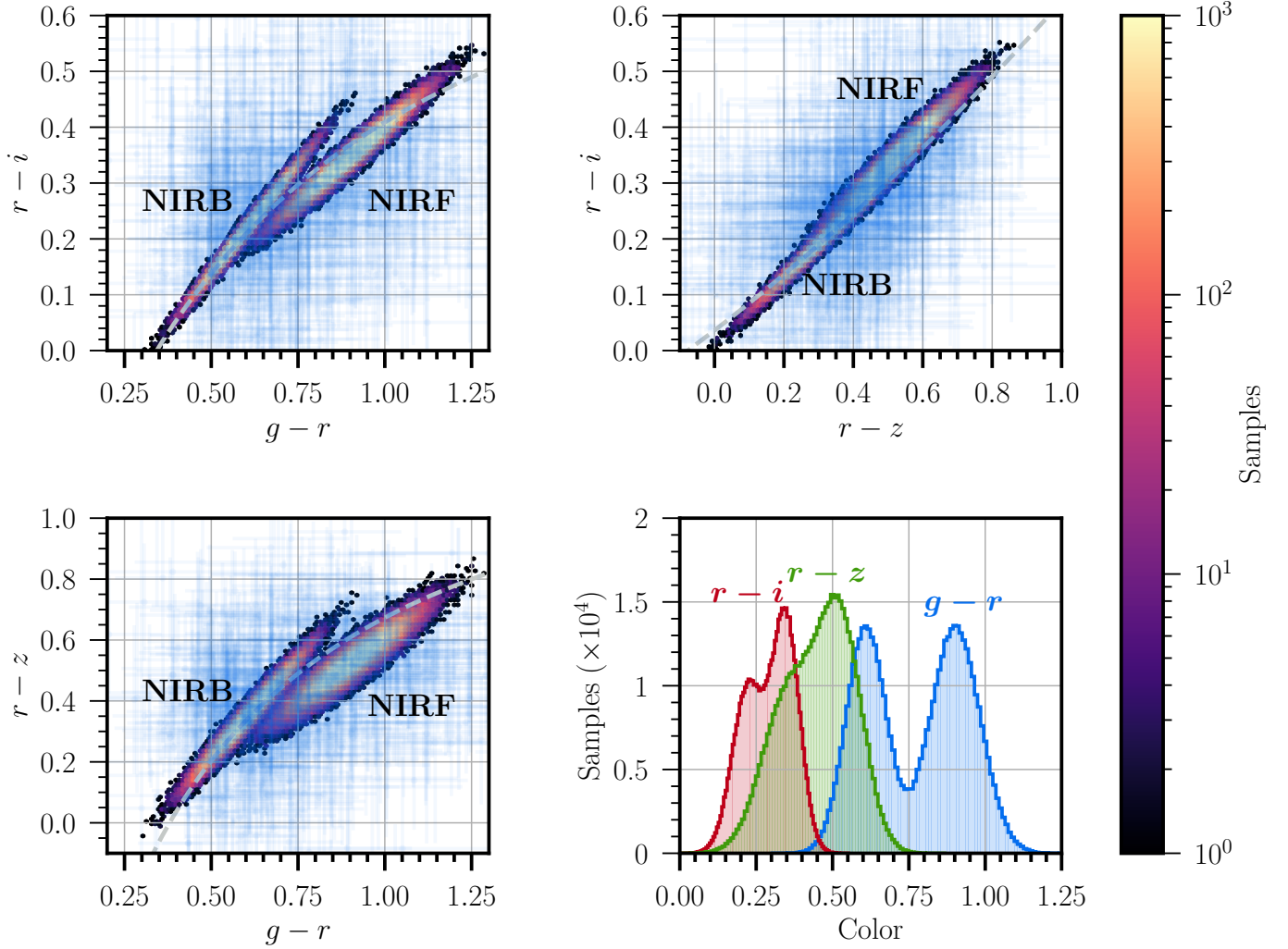


Figure 1. $g - r$, $r - i$ and $r - z$ histograms of 5×10^5 realizations of the model from Table 1, as well as all *DES* TNO color measurements and their respective error bars (in blue). The two upper panels and the lower left panel show the two-dimensional projections of the samples, and the lower right panel the one dimensional histograms of each color. In the two-dimensional panels, the gray dashed line is the locus for sources with reflectance $\propto 1 + \alpha(\lambda/550 \text{ nm})$ for varying α .

There is a striking visual resemblance between our GMM components and the color classes proposed by Fraser et al. (2023) (compare our Figure 1 to their Figure 7). The two models were independently developed from distinct datasets and with significantly different methodologies, strengthening the evidence that there are two distinct families of object surfaces in the trans-Neptunian region. Alluding to Fraser et al. (2023)’s nomenclature, we call our components “near-IR bright” (NIRB), and “near-IR faint” (NIRF), according to whether the near-IR bands i and z are brighter or fainter at a fixed visible color $g - r$.

Table 1. Parameters for the best-fit GMM

Component	Mean μ	Covariance matrix Σ	Amplitude f
NIRB	$(0.609 \ 0.223 \ 0.355)$	$\begin{pmatrix} 0.00434 & 0.00337 & 0.00547 \\ 0.00337 & 0.00268 & 0.00437 \\ 0.00547 & 0.00437 & 0.00727 \end{pmatrix}$	0.446
NIRF	$(0.902 \ 0.347 \ 0.524)$	$\begin{pmatrix} 0.00674 & 0.00362 & 0.00557 \\ 0.00362 & 0.00205 & 0.00321 \\ 0.00557 & 0.00321 & 0.00533 \end{pmatrix}$	0.554

2.2. Outliers

If we assume that the p -values derived from \mathcal{L}_α have a uniform distribution, then the expected number of targets with $(p_\alpha < p_0)$ for some threshold p_0 is $= N_{\text{TNO}}p_0$ if all objects arose from component α . For our 814 objects, $p_0 = 0.001$ leads to $N_{\text{expected}} < 1$. We have, however, two independent components—if we assign each object $p = \max(p_\alpha)$ from the two populations, then the expected number of sources with $p < p_0$ has a bound $\leq N_{\text{TNO}}p_0$, because outliers from one component might fall in a high-probability region for the other component. We can thus say with confidence that $\lesssim 1$ of the 814 TNOs should have $p < 0.001$ if they all arise from one of the two components.

In fact we find that 22 TNOs (not the same set as were outliers in the first round!) have $\max(p_\alpha) < 0.001$, a statistically significant level of outliers from the GMM. Figure 2 plots the colors of 15 outliers having at least one color measured with uncertainty < 0.2 mag, and lists the others.

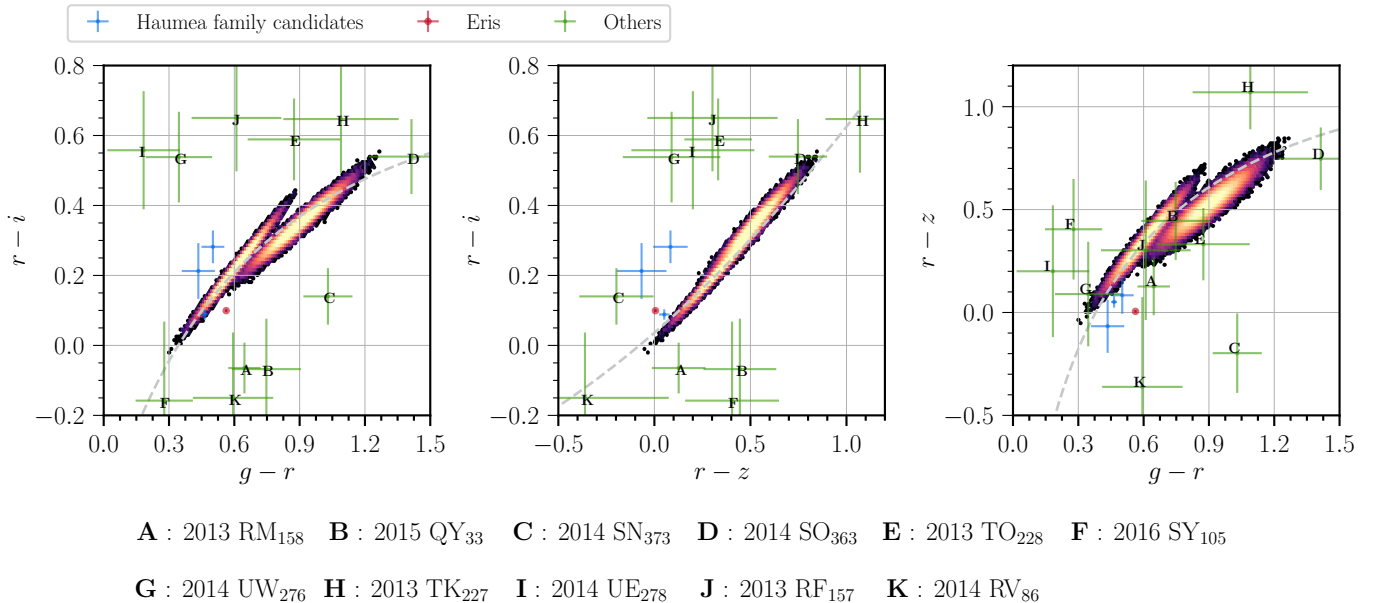


Figure 2. NIRB and NIRF realizations as in Figure 1, and, in green, the $g - r$, $r - i$ and $r - z$ colors and their respective uncertainties of the objects with $p_0 < 0.001$ for both components, and uncertainties < 0.5 (< 0.2) for the most (least) uncertain color. One of the outliers (in red) is Eris, and three of them in blue are potential Haumea family members. The other outliers are marked individually in the panels

Are there any discernible characteristics for the outliers? Eris is one, with $p \leq 10^{-5}$, which might be expected, considering this is one of the largest dwarf planets, with different physical processes than the smaller bodies; furthermore it is the brightest object in the DES sample, leading to the smallest color uncertainties.

A group of outliers with similar colors are candidates for the Haumea collisional family: 2013 UQ₁₅ has been identified both dynamically (Pike et al. 2019) through its colors (Schwamb et al. 2019) as a member of this family. Two other objects have similar colors: the orbital elements of 2010 RF₆₄ place it in the region of high probability for membership in the parameter space of Proudfoot & Ragozzine (2019), as confirmed by further dynamical studies by Proudfoot et al. (2024). 2014 UQ₂₇₇, while measurably redder in $r - i$ than Haumea and our other two candidates, is possibly in the 7:4 resonance, a potential dynamical state for escaped members of the Haumea family (Ragozzine & Brown 2007; Proudfoot & Ragozzine 2024). These objects are of dynamical interest, and motivate further study.

The other 18 $p < 0.001$ outliers are scattered around the color space with no particular distinguishing dynamical features, except that only one of them is a CC. Further observations would determine whether these objects are real outliers, indicative of other surface classes in the trans-Neptunian region, or if these identifications are the artifacts of poor photometric measurements from the DES images.

2.3. Probabilistic color class assignment

We can also use the summed probability in Equation 3 for both the NIRB and NIRF components to probabilistically assign objects to each of those classes. We define the (log) probability ratio $R_{\text{NIRF}} \equiv \log \mathcal{L}_{\text{NIRF}} - \log \mathcal{L}_{\text{NIRB}}$ to discriminate between these two color classes. $R_{\text{NIRF}} > 0$ ($R_{\text{NIRF}} < 0$) indicates a tendency for the object to belong to the NIRF (NIRB) component, with larger (smaller, that is, more negative) values indicating a stronger confidence in this assignment.

The semi-major axes, eccentricities and inclinations of all objects in the sample are presented in Figure 3, color-coded by their log probability ratio R_c . A few trends can be immediately seen from this figure: the cold Classical region ($42 \lesssim a \lesssim 48$ au, $I < 5^\circ$, $e < 0.2$) is composed almost exclusively of NIRF objects, and the majority of NIRF objects are found at lower inclinations in the other dynamical populations as well. The dynamically excited classes (hot Classicals; resonant, scattering and detached objects) appear to be NIRB dominated. Of the 10 Neptune Trojans in the DES sample, 4 are securely NIRB ($R_{\text{NIRB}} > 2$) and 2 are securely NIRF ($R_{\text{NIRF}} > 2$). This confirms the findings of Lin et al. (2019), Markwardt et al. (2023) and Bolin et al. (2023) that the absence of redder objects in this population seen by Jewitt (2018) was due to small sample size.

In the next Section, we turn these qualitative impressions into quantitative measurements of the intrinsic contributions of each color family to each dynamical class, while accounting for different observational biases in each class as well as potentially distinct absolute magnitude distributions that depend on color and dynamics.

3. LIKELIHOODS FOR COLOR/FAMILY MODELS

3.1. Mathematical framework

Consider the TNO population to be modelled as the union of subpopulations indexed by β . Each TNO has characteristics in the set $\{\mathbf{c}, H_r, A, \mathbf{P}\}$ where \mathbf{c} is an array of colors, H_r is the absolute magnitude in some reference color (assumed throughout this paper to be in r band), \mathbf{P} are the

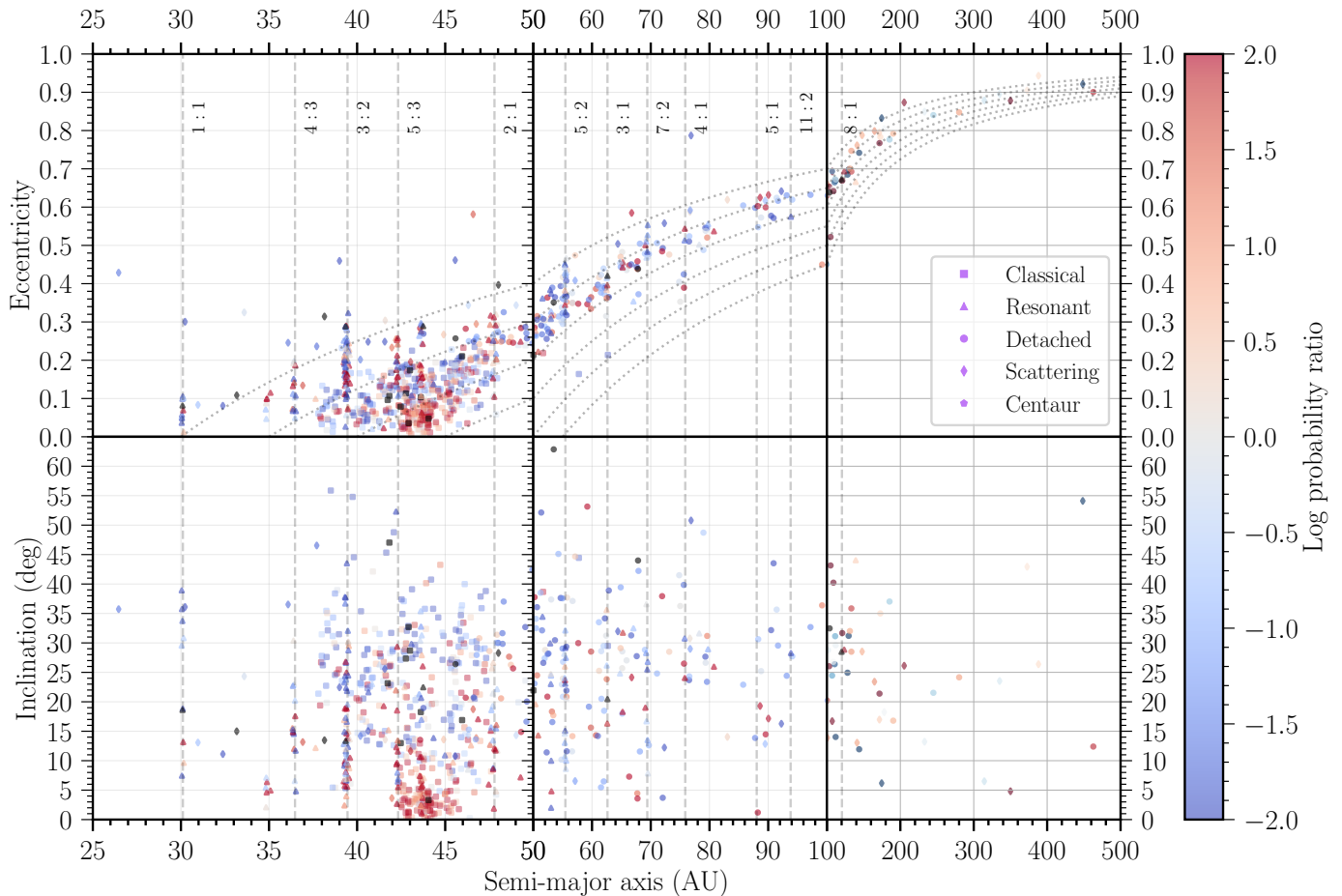


Figure 3. Semi-major axes, eccentricities and inclinations for all objects in the DES catalog. The shape of each marker indicates the dynamical classification of the object, and the color scale represents the probabilistic color assignment - objects with $|R_c| > 2$ are securely assigned to their respective classes. The outliers of Section 2.2 are marked in black. Also shown are the location of major Neptunian mean motion resonances (dashed lines), and lines of constant perihelion (dotted lines).

six orbital elements $\{a, e, i, \Omega, \omega, \mathcal{M}\}$, and A is the lightcurve amplitude. We posit that the full distribution of TNOs is a Poisson draw from a distribution over all of these parameters

$$N(\mathbf{c}, H, A, \mathbf{P}) \equiv \sum_{\beta} N_{\beta} p_{\beta}(\mathbf{c}, H, A, \mathbf{P}). \quad (5)$$

We will let \mathcal{S} be a boolean variable indicating successful selection of an object in the survey. If an object is successfully selected, our catalog gains an entry D_i containing the observation data for the object. The observational data consist of positional data that strongly constrain the orbital parameters \mathbf{P}_i , plus a flux for each exposure of the target.

We have a simulator that can give the odds of detecting and selecting a TNO of given truth features

$$p(\mathcal{S}|\mathbf{c}, H, A, \mathbf{P}). \quad (6)$$

Notice that this selection probability depends primarily upon which exposures the source hits—determined by \mathbf{P} —and upon the apparent magnitude $m_r \approx H_r - 10 \log_{10} \Delta$, where the distance Δ

to the source is another function of \mathbf{P} . There is a weaker dependence of $p(\mathcal{S})$ on the colors and lightcurve amplitude (at a given phase): Appendix D describes how this function can be estimated.

We also have an equation that gives the likelihood of obtaining the data D_i as a function of truth values. Remembering that the existence of D_i implies there has been a successful selection \mathcal{S}_i , the probability of obtaining data D_i from a member of the underlying population is

$$\mathcal{L}(D_i|\mathbf{c}, H, A, \mathbf{P}) = \mathcal{L}(D_i, \mathcal{S}_i|\mathbf{c}, H, A, \mathbf{P}) = \mathcal{L}(D_i|\mathcal{S}_i, \mathbf{c}, H, A, \mathbf{P})p(\mathcal{S}_i|\mathbf{c}, H, A, \mathbf{P}). \quad (7)$$

The likelihood of a given catalog $D = \{D_i\}$ being observed is then given by the Poisson formula for the TNO truth values, convolved with the likelihood of the observed data in terms of the truth values:

$$\begin{aligned} \mathcal{L}(D|\{N_\beta, \mathbf{q}_\beta\}) &= \prod_i \left[\sum_\beta N_\beta \int d\mathbf{c} dH dA d\mathbf{P} \mathcal{L}(D_i|\mathbf{c}, H, A, \mathbf{P}) p_\beta(\mathbf{c}, H, A, \mathbf{P}|\mathbf{q}_\beta) \right] \\ &\times \exp \left[- \sum_\beta N_\beta \int d\mathbf{c} dH dA d\mathbf{P} p(\mathcal{S}|\mathbf{c}, H, A, \mathbf{P}) p_\beta(\mathbf{c}, H, A, \mathbf{P}|\mathbf{q}_\beta) \right]. \quad (8) \end{aligned}$$

We've written this as conditioned on the subpopulation parent abundances N_β , and other hyperparameters \mathbf{q}_β of the subpopulations' $p_\beta(\mathbf{c}, H, A, \mathbf{P})$ distributions.

The MCMC procedure used in Bernardinelli et al. (2023) converts the observed D_i , which are a time series of observed fluxes for the source, into N_{samp} samples $\hat{D}_{ij} = \{\mathbf{c}_{ij}, H_{ij}, A_{ij}\}$ of color, H_r , and LCA for object i that approximate the posterior distribution of these quantities assuming a uniform prior $u(\bar{f}_g, \bar{f}_r, \bar{f}_i, \bar{f}_z, A)$ over the time-averaged, distance-adjusted mean fluxes \bar{f}_b in each band. Since we are working with magnitudes such as $H_r = \text{const} - 2.5 \log_{10} \bar{f}_r$ and $df/dH \propto 10^{-0.4H}$, the uniform prior in fluxes is equivalent to the prior

$$\Pr(\hat{D}) \equiv \Pr(\mathbf{c}, H, A) \propto \prod_{b \in g, r, i, z} 10^{-0.4H_b}. \quad (9)$$

This means that the \hat{D}_{ij} have been drawn from the distribution

$$\hat{D}_{ij} = \{\mathbf{c}_{ij}, H_{ij}, A_{ij}\} \sim \frac{1}{E(D_i)} \mathcal{L}(D_i|\hat{D}) \Pr(\hat{D}), \quad (10)$$

$$E(D_i) \equiv \int d\hat{D} \mathcal{L}(D_i|\hat{D}) \Pr(\hat{D}). \quad (11)$$

The normalizing quantity $E(D_i)$ is the evidence of the observations D_i under the assumed uniform-flux prior.

It is also true that the astrometric observations have determined the orbital parameters essentially perfectly for our current purposes, so that the \mathbf{P} dependence of $\mathcal{L}(D_i|\mathbf{c}, H, A, \mathbf{P})$ separates into $\delta(\mathbf{P} - \mathbf{P}_i)$. Given (10) and this delta function, the integral in the first term of the right-hand side of Equation (8) can be approximated using importance sampling of the \hat{D}_{ij} as

$$\int d\mathbf{c} dH dA d\mathbf{P} \mathcal{L}(D_i|\mathbf{c}, H, A, \mathbf{P}) p_\beta(\mathbf{c}, H, A, \mathbf{P}|\mathbf{q}_\beta) \approx \frac{E(D_i)}{N_{\text{samp}}} \sum_j \frac{p_\beta(\mathbf{c}_{ij}, H_{ij}, \mathbf{P}_i, A_{ij}|\mathbf{q}_\beta)}{\Pr(\mathbf{c}_{ij}, H_{ij})} \quad (12)$$

The factor to the left of the sum is determined by the measurement errors on the fluxes, which are independent of the subsample β or any of its parameters \mathbf{q}_β , leading to an irrelevant constant multiplicative scaling of the final likelihood in Equation (8). The likelihood of any given model can therefore be expressed as

$$\log \mathcal{L}(\{N_\beta, \mathbf{q}_\beta\} | D) = \sum_i \log \left[\sum_\beta N_\beta R_{i\beta} \right] - \sum_\beta N_\beta S_\beta + \log p(\{N_\beta, \mathbf{q}_\beta\}) + (\text{const}) \quad (13a)$$

$$R_{i\beta} \equiv \sum_j \left[p_\beta(\mathbf{c}_{ij}, H_{ij}, \mathbf{P}_i, A_{ij} | \mathbf{q}_\beta) \prod_{b \in \{g, r, i, z\}} 10^{0.4(H_{ij} + c_{br, ij})} \right] \quad (13b)$$

$$S_\beta \equiv \int d\mathbf{c} dH dA d\mathbf{P} p(\mathcal{S} | \mathbf{c}, H, A, \mathbf{P}) p_\beta(\mathbf{c}, H, A, \mathbf{P} | \mathbf{q}_\beta). \quad (13c)$$

Similar to the GMM procedure, we can reparametrize this function by defining $N \equiv \sum_\beta N_\beta$ and $f_\beta \equiv N_\beta/N$, so that $0 \leq f_\beta \leq 1$ and $\sum_\beta f_\beta = 1$. The f_β variables are thus constrained to lie on a simplex, so there is total number of free parameters is unchanged. The model becomes

$$N(\mathbf{c}, H, A, \mathbf{P} | \{\mathbf{q}_\beta\}) = N \sum_\beta f_\beta p_\beta(\mathbf{c}, H, A, \mathbf{P} | \mathbf{q}_\beta), \quad (14)$$

where, with no loss of generality, we posit that

$$\int d\mathbf{c} dH dA d\mathbf{P} p_\beta(\mathbf{c}, H, A, \mathbf{P} | \mathbf{q}_\beta) = 1. \quad (15)$$

The likelihood becomes

$$\log \mathcal{L}(\{N, f_\beta, \mathbf{q}_\beta\} | D) = (\text{const}) + \log p(\{N, f_\beta, \mathbf{q}_\beta\}) + \sum_i \log \left[N \sum_\beta f_\beta R_{i\beta} \right] - N \sum_\beta f_\beta S_\beta. \quad (16)$$

We can solve for N analytically, under the assumption of a uniform prior distribution, as follows. The maximum likelihood is found where $\partial_N \log \mathcal{L} = 0$:

$$\frac{\partial \log \mathcal{L}}{\partial N} = \frac{N_{\text{obj}}}{N} - \sum_\beta f_\beta S_\beta = 0 \implies N = \frac{N_{\text{obj}}}{\sum_\beta f_\beta S_\beta}. \quad (17)$$

Substituting back in the likelihood, we have that

$$\log \mathcal{L}(\{f_\beta, \mathbf{q}_\beta\} | D) = (\text{const}) + \log p(\{f_\beta, \mathbf{q}_\beta\}) + \sum_i \log \left[\sum_\beta f_\beta R_{i\beta} \right] - N_{\text{obj}} \log \left[\sum_\beta f_\beta S_\beta \right]. \quad (18)$$

3.2. Choice of functional forms and interpreting f_β

To this point, we have made no strong restrictions as to what defines membership in the families β of TNOs that comprise the mixture model defined in Equation (5): β could represent TNOs with some particular physical characteristics, such as colors (as in Section 2, where $\beta \rightarrow \alpha$), or a dynamical state d of the object (*e.g.* as in Gladman et al. 2008), or a joint physical+dynamical distribution

with subpopulations enumerated by a pair $\beta = (\alpha, d)$. In the subsequent analyses, we will assume that, within a family β , the orbital parameters, absolute magnitudes, colors and lightcurve amplitude functional forms are separable, that is,

$$p_\beta(\mathbf{c}, H_r, A, \mathbf{P}) = p_\beta(\mathbf{c})p_\beta(H_r)p_\beta(\mathbf{P})p_\beta(A). \quad (19)$$

This means that we can choose a functional form for each underlying distribution, and maximize the likelihood in Equation 18 to find the most likely values of the parameters \mathbf{q}_β of the p_β functions. Note that we require our distributions to be normalized.

We initially fix the color functions $p_\beta(\mathbf{c})$ to be one of the Gaussians derived by the GMM, *i.e.* defined in Equation (2) with the parameters given in Table 1 for $\alpha \in \{\text{NIRF}, \text{NIRB}\}$. This naturally incorporates probabilistic color classification into our dissection of the full TNO population. The GMM parameters will *not* be maximized with the rest of the likelihood, although we will in Section 5 explore cases where we subdivide each GMM component to create > 2 possible color subpopulations.

For $p_\beta(H)$ distributions, we adopt a rolling power law (as in Bernstein et al. 2004), which adds curvature to a simpler power-law distribution:

$$p_\beta(H_r | \theta_\beta, \theta'_\beta) \propto 10^{\theta_\beta(H_r - 7) + \theta'_\beta(H_r - 7)^2}. \quad (20)$$

We will restrict all of our further analyses to TNOs with $5.5 < H_r < 8.2$, assume all H values are in the r band, and normalize $p_\beta(H)$ to unit integral over this range. In this case, a numerical normalization is more convenient, although an analytic normalization is possible. Some care is needed when comparing population counts or fractions f_β that have been derived for different ranges of H_r .

For $p_\beta(A)$, we adopt the β -distribution models of Bernardinelli et al. (2023).

$$p_\beta(A | \bar{A}_\beta, s_\beta) = A^{\bar{A}_\beta 10^{s_\beta} - 1} (1 - A)^{(1 - \bar{A}_\beta) 10^{s_\beta} - 1} \times \frac{\Gamma(10^{s_\beta})}{\Gamma(\bar{A}_\beta 10^{s_\beta}) \Gamma((1 - \bar{A}_\beta) 10^{s_\beta})}, \quad (21)$$

where \bar{A} is the mean lightcurve amplitude, and s is a sharpness parameter. At fixed \bar{A} , a larger s implies a narrower distribution about \bar{A} . As shown in Bernardinelli et al. (2022), for a fixed apparent magnitude m_r , the completeness function is virtually independent of A , so $p(A | \mathcal{S}) \approx \text{const}$. This means that, while computing the S_β terms, the $p_\beta(A)$ integrals always evaluate to 1, simplifying the likelihood calculation.

The classification of TNOs into dynamical classes indexed by d is incorporated by having each β be associated with one d using an indicator function

$$p_\beta(\mathbf{P}) = \begin{cases} 1, & \text{if } \mathbf{P} \text{ implies the object belongs to dynamical class } d \\ 0 & \text{otherwise} \end{cases}. \quad (22)$$

Our analyses will define subpopulations by a combination of a physical family α and a dynamical family d , *i.e.* $\beta = (\alpha, d)$, so we will be using Equation (18) to constrain population fractions $f_{\alpha d}$ with data from *all* of our objects (in our chosen H_r range) simultaneously, as well as constrain the hyperparameters \mathbf{q}_β constraining size and lightcurve distributions. This allows us to test whether distinct dynamical families share their physical parameters.

We can also define the fraction of a dynamical class d that is made of a physical class α as

$$f_{\alpha|d} \equiv \frac{f_{\alpha d}}{\sum_{\alpha'} f_{\alpha' d}}. \quad (23)$$

The $f_{\alpha|d}$ are independent of the relative contribution of class d to the overall model in Equation 1, so $f_{\alpha|d}$ and $f_{\alpha|d'}$ can be meaningfully compared to each other. In other words, our approach of leaving one overall N for the full population and a single simplex constraint $\sum_{\alpha d} f_{\alpha d} = 1$ is mathematically equivalent to having a free number density N_d for each dynamical class, and distinct simplex constraint $\sum_{\alpha} f_{\alpha|d} = 1$ for each.

Other investigators have reported ‘‘X-to-Y’’ ratio of physical properties (for example, neutral-to-red) within a dynamical class d . The results of our MCMC chains for the f values can be converted to such an estimate in some range $H_1 < H_r < H_2$ for class d as

$$R = \frac{f_{Xd} \int_{H_1}^{H_2} dH p_X(H)}{f_{Yd} \int_{H_1}^{H_2} dH p_Y(H)}. \quad (24)$$

4. THE NIRB AND NIRF PHYSICAL PARAMETER DISTRIBUTIONS

In this section, we will assess decompositions of the members of various dynamical classes into two physical components, one with color distribution $p_{\beta}(\mathbf{c})$ following the NIRB component of the GMM, the other drawn from NIRF colors. The hyperparameters describing the H and A distributions for some component β are $\mathbf{q}_{\beta} = \{\theta_{\beta}, \theta'_{\beta}, \bar{A}_{\beta}, s_{\beta}\}$. Our inference will proceed as follows:

1. Evaluate the log-likelihood of Equation (18) for each dynamical class independently, yielding the posterior probability distribution $p_d(f_{\text{NIRB}|d}, \mathbf{q}_{\text{NIRB},d}, \mathbf{q}_{\text{NIRF},d} | D_d)$ of the NIRB fraction and the NIRB/NIRF size and variability distributions within each d .
2. Test the hypothesis that all d share a common set of parameters, $\mathbf{q}_{\text{NIRF},d} = \mathbf{q}_{\text{NIRF}}$ and $\mathbf{q}_{\text{NIRB},d} = \mathbf{q}_{\text{NIRB}}$, against the hypothesis that there are distinct \mathbf{q} 's for each dynamical class. If the shared-value hypothesis is favored, or at least not disfavored, then the data allow for each dynamical class to be composed of its own mixture of just two global physical populations, $\beta \in \{\text{NIRB}, \text{NIRF}\}$.
3. We can refit the full sample simultaneously to this model of shared parameters across distributions to obtain $p(\{f_{\beta,d}\}, \mathbf{q}_{\text{NIRB}}, \mathbf{q}_{\text{NIRF}}, |D)$.
4. Marginalizing over the fractions $f_{\beta,d}$ yields the allowed physical hyperparameters for the NIRB and NIRF populations.
5. Marginalizing over the physical parameters yields estimates of the fractions $f_{\text{NIRB}|d}$ of each population that is in NIRB, and also of the total number of sources in our chosen H range in each dynamical component.

Our analysis uses only DES TNOs with $5.5 < H_r < 8.2$, and we will exclude all outliers from Section 2.2 (of which 16 are in this size range), which leaves us with 696 objects. The left column of Table 2 lists the 5 distinct dynamical classes d into which we divide these. The right column gives a subdivision of the Resonant class members for investigation of their dependence vs semi-major axis.

Table 2. Sample definitions

Comprehensive subsets			Resonant subsets		
Subset	# objects	f_{NIRB}	Subset	# objects	f_{NIRB}
Cold Classical (CC)	102	0.019 ± 0.015	Neptunian Trojan (1:1)	6	0.682 ± 0.156
Hot Classical (HC)	254	0.631 ± 0.034	Inner belt (5:4 & 4:3)	13	0.551 ± 0.139
Scattering	33	0.686 ± 0.090	3:2	49	0.559 ± 0.075
Resonant	172	...	Main belt (5:3 & 7:4)	42	0.279 ± 0.075
Detached	135	0.710 ± 0.045	2:1	18	0.408 ± 0.126
			5:2	12	0.792 ± 0.110
Total	696		Distant ($a > 50$ au, excluding 5:2)	32	0.614 ± 0.091

NOTE—The dynamical definitions follow the scheme of Gladman et al. (2008), and the Classicals are subdivided by their free inclinations following Huang et al. (2022) - objects with $I_{\text{free}} \leq 5^\circ$ are considered Cold Classicals, objects with higher free inclinations are Hot Classicals. A complete description of the dynamical classification procedure is presented in Bernardinelli et al. (2022). The left column lists the 5 distinct dynamical classes which span the entire set of 696 DES TNOs with $5.5 < H_r < 8.2$. The right column lists some subsets of the resonant class, which will be compared in Section 4.3. The mean and standard deviation of the fraction of the dynamical class coming from the NIRB physical class is given, assuming common $p(H)$ slopes across all dynamical classes as in Section 4.1. We do not provide f_{NIRB} for the Resonant objects because the different resonances have significantly distinct values.

4.1. Do dynamical distributions share physical hyperparameters?

The left panel of Figure 4 shows the posterior distributions of the NIRB $p(A)$ distribution parameters $\bar{A}_{\text{NIRB},d}$ and $s_{\text{NIRB},d}$, computed for each individual dynamical class d , and the distribution of \bar{A}_{NIRB} and s_{NIRB} if all classes are required to share the share common parameters. The right panel shows the same thing for the NIRF class. The means of these posterior distributions satisfy $\bar{A}_{\text{NIRF}} > \bar{A}_{\text{NIRB}}$ in every case; and all of the classes' 68% credible regions overlap with the common model. The variability amplitude of the NIRF TNOs is significantly higher than that of the collected NIRB TNOs, which remains true even when CC's are removed from the NIRF population, suggesting that this is a birth characteristic of the population rather than a consequence of migration history.

When producing these posterior distributions for a single dynamical class d in isolation, there are 9 free parameters: 2 $p(A)$ parameters (\bar{A}, s), plus two $p(H)$ parameters (θ, θ') for each of the NIRB and NIRF components, plus the contribution fraction $f_{\text{NIRB}|d}$. In the case of shared distributions, there are 8 free physical parameters, plus 9 degrees of freedom among the 2×5 simplex-constrained fractions $f_\beta = f_{\alpha,d}$. This is too many dimensions to evaluate the likelihood over a comprehensive grid; instead, we sample the posterior distribution using a Hamiltonian Monte Carlo (HMC) chain. The HMC generates less-correlated samples with a higher acceptance rate than the simpler Metropolis-Hastings Monte Carlo approach, and readily adapts to simplex constraint(s) on the f_β in an arbitrary number of dimensions. We present a short introduction to HMC in Appendix C.

For a quantitative test of whether all d share the same $p(A)$ within a color class, we can compute the log Bayesian evidence ratio \mathcal{R} between hypothesis \mathcal{H}_1 (one shared $p(A)$ distribution for all NIRB objects, and one for all NIRF objects), and hypothesis \mathcal{H}_2 (each subpopulation has its own values

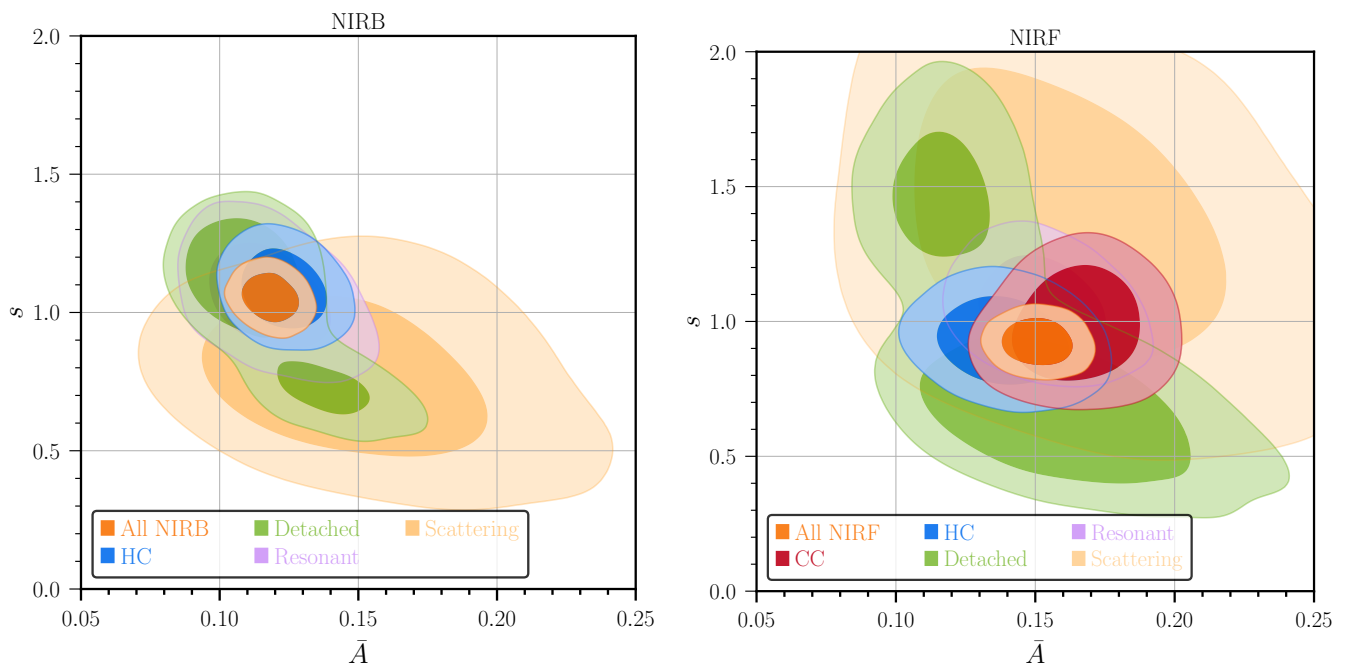


Figure 4. 68% and 95% posterior contours for the HMC-derived samples for the NIRB (left) and NIRF (right) parameters \bar{A} and s parameters of the LCA distribution. Each figure contains the posterior for all disjoint sets of objects from the distinct dynamical classes, and the posterior derived from fitting all the subsets simultaneously (the smallest, orange contours). Note there is no cold-classical constraint on the NIRB component because the CC’s are purely NIRF.

of the \bar{A}_α and s_α parameters). Appendix B reviews the definition of the evidence ratio and how we measure it from the MCMC chain outputs. In the [Jeffreys \(1961\)](#) scale, evidence ratios of $\mathcal{R} > 2.30$, 3.45, 4.61 are said to be “strong”, “very strong” and “decisive” in favor of \mathcal{H}_2 . As this is a logarithmic scale, negative values of \mathcal{R} imply that \mathcal{H}_1 is preferred over \mathcal{H}_2 , and its significance is measured on the same absolute scale.

The resultant log evidence ratios for a shared set of $p(A)$ parameters are 5.016 and 6.143 for the NIRB and NIRF components, both showing *decisive* evidence in favor of the shared-parameter models. Evidence ratios are sensitive to the priors assumed on the parameters. We have taken uniform priors for $\bar{A}_{\text{NIRF,NIRB}} \in [0.05, 0.25]$ and $s_{\text{NIRF,NIRB}} \in [0.4, 1.9]$, and the evidence is decisively in favor of the shared model for any reasonable choice of prior.

We also test whether the NIRF $p(A)$ is driven by the CC population. The resulting posteriors for the non-CC NIRF distribution are near identical to the case when the CCs are included, and we have that the evidence ratio for a scenario where the non-CC NIRF population is distinct (and therefore more variable) than the NIRB TNOs is $\mathcal{R} = 4.22$, showing very strong evidence for two distinct populations.

We can similarly turn our attention to the parameters θ and θ' of the $p(H)$ distributions. Figures 5 plot the posterior distributions of the slope parameters for NIRB (left) and NIRF (right) components of each individual dynamical class, and for a model in which these parameters are shared across dynamical classes. There is again visual agreement between all the classes, and we can calculate the evidence ratios between the hypotheses of common vs separate H distributions per class d .

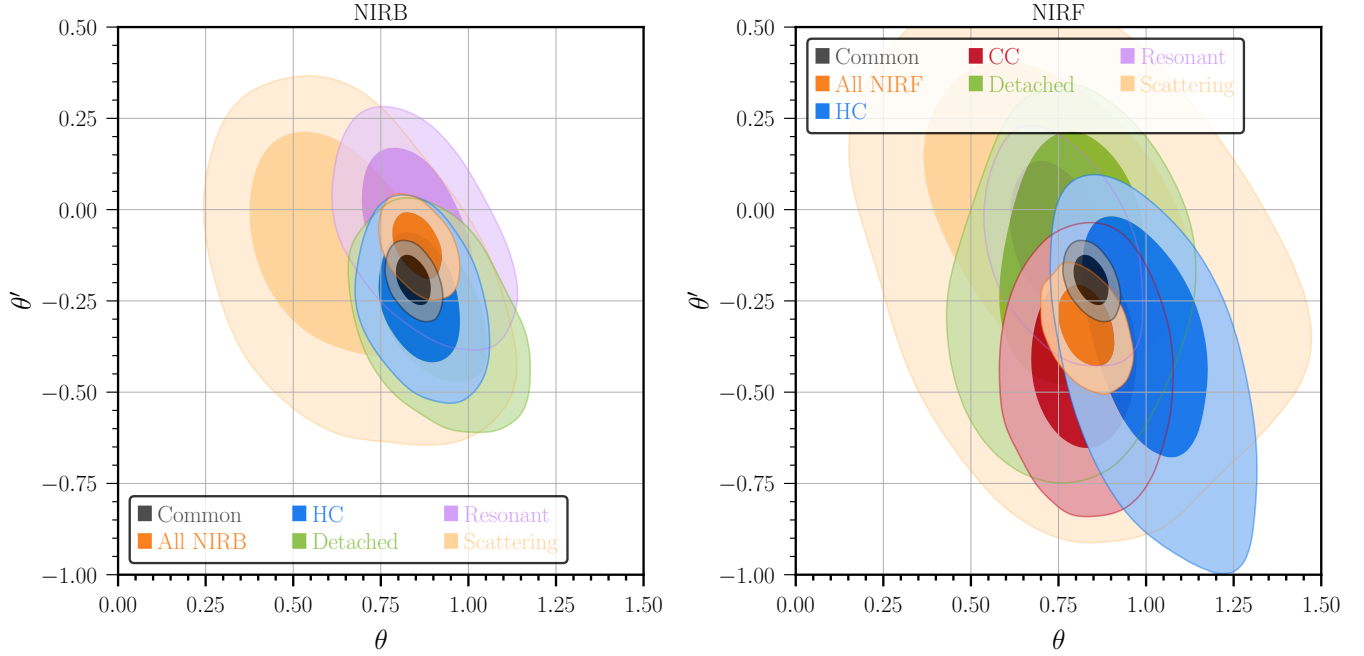


Figure 5. Similar to Figure 4, this figure shows posterior contours for the NIRB (left) and NIRF (right) (θ, θ') parameters of the rolling power law H_r distribution. In addition to the disjoint sets of distinct dynamical classes, the posteriors in orange represent a single rolling power law for all members of either the NIRB or the NIRF class, and the black posterior shows a common distribution for all samples, independently of their color families.

A common distribution is preferred for all NIRB or NIRF objects: the evidence ratio for a 4 parameter $(\theta_{\text{NIRB}}, \theta'_{\text{NIRB}}, \theta_{\text{NIRF}}, \theta'_{\text{NIRF}})$ distribution, assuming a uniform prior that restricts $0 \leq \theta \leq 1.5$ and $-1 \leq \theta' \leq 1$, is $\mathcal{R} = 13.556$, showing decisive evidence for a common distribution instead of one H_r distribution per dynamical class. We should again take note of sensitivity of \mathcal{R} to the prior, *e.g.* the width W of the prior on θ appears once per dynamical subpopulation d in the numerator of the evidence ratio, while in the denominator it appears only once, which means that the evidence ratio scales as W^{-8} . Hence \mathcal{R} would drop by ≈ 6 if we were to halve the width of our prior. A large reduction in the prior width could change the Bayes ratio from being decisively in favor of shared $p(H)$ slopes to being inconclusive. At that point, however, most of the dynamical classes would have their posterior probabilities determined primarily by the prior, with the data being unimportant. So it is fair to say that, to the extent that the data inform the $p(H)$ slopes and derivatives, they favor the common model.

We conclude that the DES data support a model in which each of the two GMM color components has a population with size and variability distributions that are the same in every dynamical state, *i.e.* the various dynamical classes are each composed of a mixture of shared NIRF and NIRB populations, within the selected H range.

4.2. Physical characteristics of NIRF and NIRB

We now adopt the two-component physical model and examine the H and A distributions implied by the 696-element sample. The variability distributions of the NIRF and NIRB classes are distinct, in agreement with the results of [Bernardinelli et al. \(2023\)](#). In this model, the NIRF population is more

variable: $\bar{A}_{\text{NIRB}} = 0.118 \pm 0.007$, vs $\bar{A}_{\text{NIRF}} = 0.151 \pm 0.008$, a 3σ difference; while the s parameters are similar, $s_{\text{NIRB}} = 1.054 \pm 0.058$ vs $s_{\text{NIRF}} = 0.922 \pm 0.087$. We show the posterior distributions for the NIRB and NIRF parameters, and illustrate the resulting shape of the β distribution, in Figure 6.

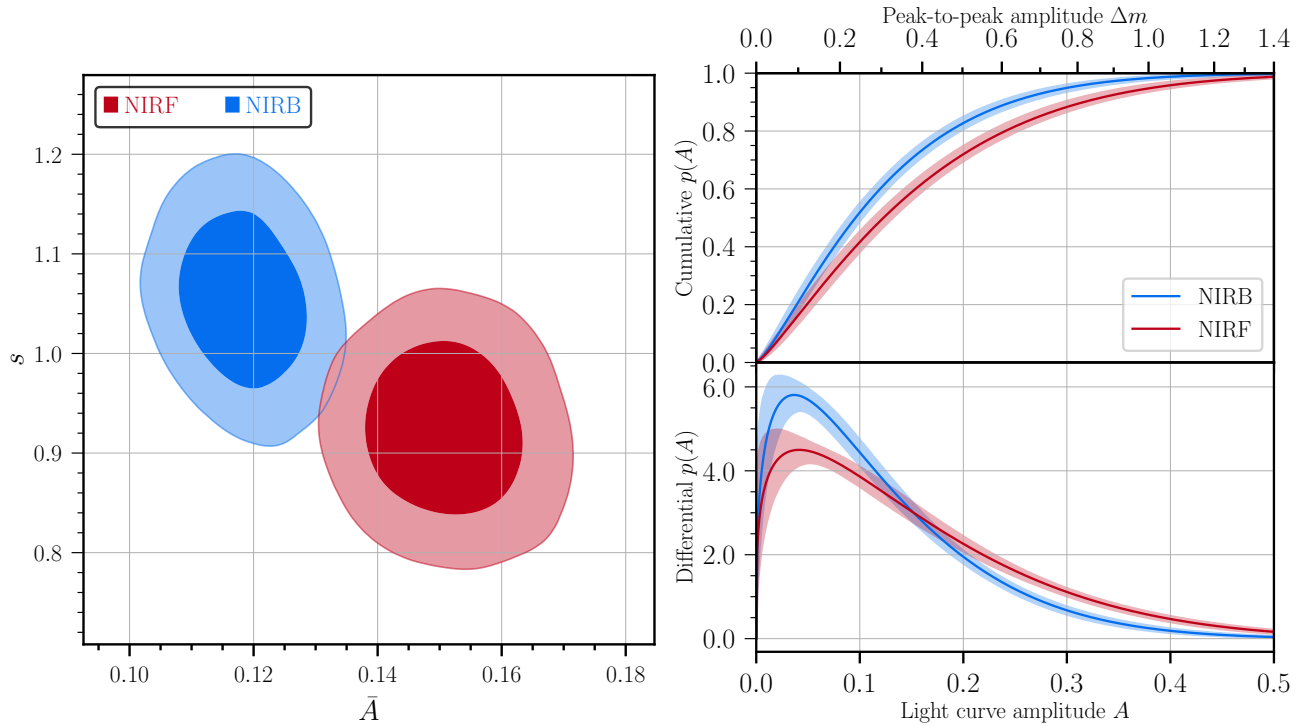


Figure 6. *Left:* 68% and 95% posterior contours of the NIRB (blue) and NIRF (red) LCA distribution parameters. *Right:* Visualization of the mean and 68% limits of the cumulative (top) and differential (bottom) distributions for the NIRB and NIRF distributions. The horizontal axis shows both the LCA A and the peak-to-peak amplitude $\Delta m \equiv 2.5 \log_{10}((1 + A)/(1 - A))$.

Bernardinelli et al. (2023) show (using the same data) a decisive distinction between the detached and CC LCA distributions, and very strong distinction between the HC and CC distributions, setting the constraint that there are at least two distinct LCA distributions. This is consistent with the newer results, since the CCs are almost entirely NIRF members (with higher variability) while the scattering and HC populations are NIRB-dominated. Thus the variability amplitude can be associated either with another physical property (color), or with dynamical state. The data are not of sufficient power to determine whether color or dynamical state is the stronger predictor of \bar{A} .

The posteriors of the H distributions of NIRF and NIRB, on the other hand, overlap substantially: we have that $\theta_{\text{NIRB}} = 0.856 \pm 0.047$, $\theta'_{\text{NIRB}} = -0.099 \pm 0.059$ and $\theta_{\text{NIRF}} = 0.829 \pm 0.053$, $\theta'_{\text{NIRF}} = -0.321 \pm 0.073$. We can test whether a single distribution is sufficient to describe the data, that is, if the NIRF and NIRB H_r distributions are distinguishable from each other assuming a rolling power law. The evidence ratio is $\mathcal{R} = 2.370$, showing strong evidence for a common distribution. In this case, $\theta = 0.844 \pm 0.033$ and $\theta' = -0.227 \pm 0.045$. This is in concurrence with the observation by Petit et al. (2023) that the H distribution of CC's in the OSSOS survey has the same shape as the dynamically “hot” population in the range $5.5 < H_r < 8.3$, nearly the same as we examine.

Furthermore, as has been well established in [Bernstein et al. \(2004\)](#) and reproduced in subsequent works (*e.g.* [Napier et al. 2024](#)), we find that $\theta' < 0$ to high significance, indicating a deficit of small objects relative to power-law extrapolations of brighter sources.

Our range of H_r is sufficient to clearly exclude a single-power-law $p(H_r)$, however it is too narrow to differentiate between different formulae for the departure from power-law. For instance the exponentially tapered power law of [Kavelaars et al. \(2021\)](#), motivated by simulations of the streaming instability hypothesis ([Youdin & Goodman 2005](#)), can fit our data equally well with the proper choice of parameters. We do not quantify other $p(H_r)$ models because the data lack the power to discriminate them from the rolling power law.

4.3. NIRF/NIRB fractions of dynamical classes

We next examine the posterior probability distributions of the NIRB fraction $f_{\text{NIRB}|d}$ for each class d by marginalizing over the shared parameters \mathbf{q} . These are plotted on the left half of [Figure 7](#), and the means and standard deviations are given in [Table 2](#). As expected, there is substantial variation among the 5 dynamical classes, and the Bayesian evidence test completely rules out the hypothesis that all classes share a common f_{NIRB} with $\mathcal{R} = 62.185$. If we accept the NIRB and NIRF classes are representing two different birth regions in the solar system, these values constrain the fraction of each class that was born in the nearer heliocentric distance range.

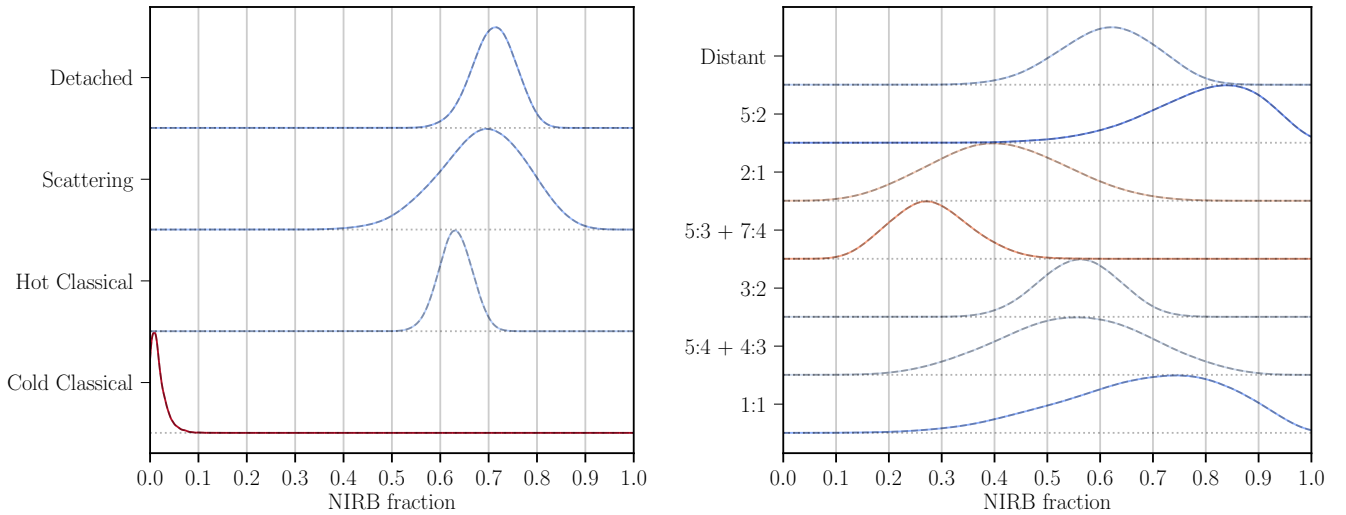


Figure 7. Posterior distributions of $f_{\text{NIRB}|d}$ after marginalizing over physical hyperparameters of the NIRF and NIRB populations. The vertical axis represents the distinct subsets of the data, and, inside a certain subset, this axis represents the relative probability of the posterior. The color of each curve relates to the peak of the distribution, going from red (NIRF-dominated) to blue (NIRB-dominated). The left panel shows the posteriors for the 4 main dynamical subsets (cold and hot Classicals, scattering and detached objects), while the right panel shows the posteriors for resonant subpopulations, stacked in order of a .

As expected, the CC dynamical class is consistent with 100% NIRF composition, with the dynamically excited classes mixing the NIRF and NIRB populations.

It is also of interest to divide the Resonant class into subclasses for different resonances with corresponding distinct values of semi-major axes a . In this case the values of θ are still being informed

by the other dynamical classes, but each resonance subset has its own free f_{NIRB} . These are shown on the right side of Figure 7, and the means and standard deviations are given in Table 2, and indicate a diversity of physical origins for distinct resonances’ populations. In particular, the resonances amidst the “main belt” of classical TNOs, the 5:3 and 7:4, are unique in being dominated by the NIRF population, similar to the CCs. A common f_{NIRB} distribution for all resonant subgroups is also “strongly” excluded by the Bayesian evidence ratio, at $\mathcal{R} = 2.403$.

In summary, the CC populations is essentially pure NIRF, and all of the dynamically excited populations are consistent with f_{NIRB} in the 0.6–0.8 range, with the notable exception that the “main belt” resonances (definitely) and 2:1 resonance (probably) have a larger fraction of NIRF objects.

4.4. Inclination dependence of NIRF/NIRB fractions

Figure 8 shows the evolution of f_{NIRB} among subsets of the TNOs defined by inclination angle (for the Classical population, we use free inclinations). At left, the merged CC+HC sample is divided into 8 bins of increasing I and the model with 2 physical components is fit to the ensemble with free $f_{\text{NIRB},d}$ for each inclination bin d . By definition, the 2 lowest- I bins are the CC’s, where a pure-NIRF population is favored. As expected, higher- I bins (the HC’s) show higher f_{NIRB} , but it also seems that this fraction is strongly inclination-dependent within the HC population. This is quantitatively confirmed by a decisive Bayesian evidence ratio, $\mathcal{R} = 6.588$, favoring distinct f_{NIRB} values for each HC inclination bin over a common f_{NIRB} for all the HC bins. We note that this gradient in NIRF/NIRB population could underlie much of the correlation between inclination and visible spectral slope reviewed by Marsset et al. (2019). But analysis of the ColOSSOS data by Marsset et al. (2023), separating TNOs into their BrightIR and FaintIR color groups analogous to our own NIRB/NIRF, suggest that an anticorrelation between visible spectral slope and inclination exists even within the BrightIR class. This suggests that we investigate potential differences between the red and blue ends of the NIRB sequence, which we will do in the Section 5.

The center and right panels of Figure 8 slice the Plutino and the combined scattering+detached classes into inclination bins. The visually apparent trend toward higher f_{NIRB} at higher inclinations—with the $I > 40^\circ$ bin consistent with 100% NIRB—is not, however, quantitatively significant. Indeed the evidence ratio for distinct vs common f_{NIRB} across inclination bins is $\mathcal{R} = -0.27$ for the Plutinos, and $\mathcal{R} = 0.743$ for the joint scattering+detached classes, offering no strong preference for either scenario. We revisit and quantify the f_{NIRB} dependency with inclination in Section 6.

4.5. Goodness of fit

We conclude this section by testing whether the 2-component model is a good description of the underlying data. To do so, we first evaluate whether the GMM color model derived in Section 2 is a good fit to the observed color distribution (with the outliers excluded). Our goodness-of-fit statistic will be the $\log \mathcal{L}$ in Equation 18 (including only the color terms). We produce a distribution of expected $\log \mathcal{L}$ by drawing 10^5 sets of 696 TNOs from the best-fit GMM to the data. For each sampled TNO, we create a color “swarm” by shifting the measurement distribution of a real TNO to the newly sampled colors as in Section 2.2. For each set k of 696 simulated measurements, we repeat the GMM training procedure of Section A to find the best GMM for this realization of the full population, and then retain the resultant $\log \mathcal{L}_k$ of the realization. A p -value for the real data

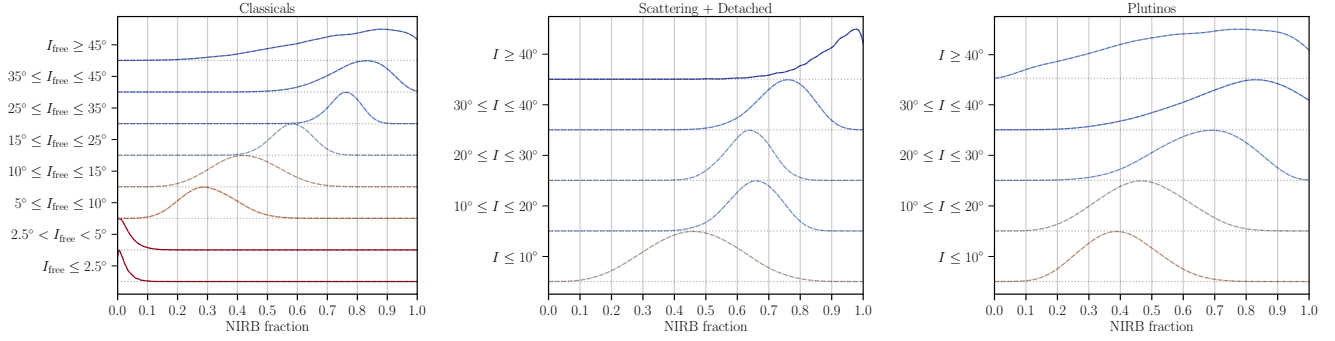


Figure 8. Similar to Figure 7, where the TNOs are now split into bins of inclination. The left panel shows the Classical population (HC+CC), the center panel shows the joint set of Scattering and Detached objects, and the right panel shows the Plutinos.

is defined as the fraction of the realizations for which $\log \mathcal{L}_k < \log \mathcal{L}_{\text{data}}$. We arrive at $p = 0.918$, indicating that the real data (with outliers excluded) are a plausible realization of the GMM.

The same goodness-of-fit process is repeated for the rolling-power-law distributions of H_r . We create a realization of the 696 truth values of H_r for TNOs by sampling from the model with the likelihood-maximizing values of $\{\theta, \theta'\}$ and $\{f_\alpha\}$, preserving the number of objects per dynamical class. To place measurement errors to these synthetic H_r measurements, we assign the measurement errors in H of the n^{th} -brightest real TNO in each dynamical class to the n^{th} -brightest TNO of the dynamical class in the realization. This gives the smallest objects the largest uncertainties in H , as in the real data. Then, we re-minimize the likelihood in Equation 18. Repeating this procedure 5×10^4 times, we find that the resultant (θ, θ') values are shifted by $(0.039 \pm 0.022, -0.024 \pm 0.019)$ from the input values, suggesting immaterially small biases in the process. We can also use this procedure to derive a p -value from $\log \mathcal{L}$ as above, obtaining $p = 0.860$, once again indicating a good fit.

As a further test of the rolling-power-law parameterization of $p(H_r)$, we compare the observed cumulative distributions of H_r in each dynamical class to the cumulative distributions obtained from draws from the rolling power law that have been subjected to our selection criteria and measurement errors. Figure 9 shows the resulting data and model curves, and Table 3 presents the p -values obtained by comparison of the data to the model distributions with the Kolmogorov-Smirnov (KS) and Anderson-Darling statistics (Press 2007). Both tests show that for all dynamical subsets are consistent with the null hypothesis that the data are sampled from the best-fit models.

Table 3. p -values of the KS and AD statistics for the H_r distribution

Subset	KS	AD	Subset	KS	AD	Subset	KS	AD
CC	0.878	0.697	HC	0.748	0.241	Detached	0.989	0.916
Scattering	0.255	0.301	Trojan	0.622	0.787	Inner belt	0.051	0.213
Plutino	0.982	0.999	Main Belt	0.231	0.466	2:1	0.221	0.408
5:2	0.677	0.574	Distant	0.621	0.747			

5. ARE TWO COMPONENTS ENOUGH?

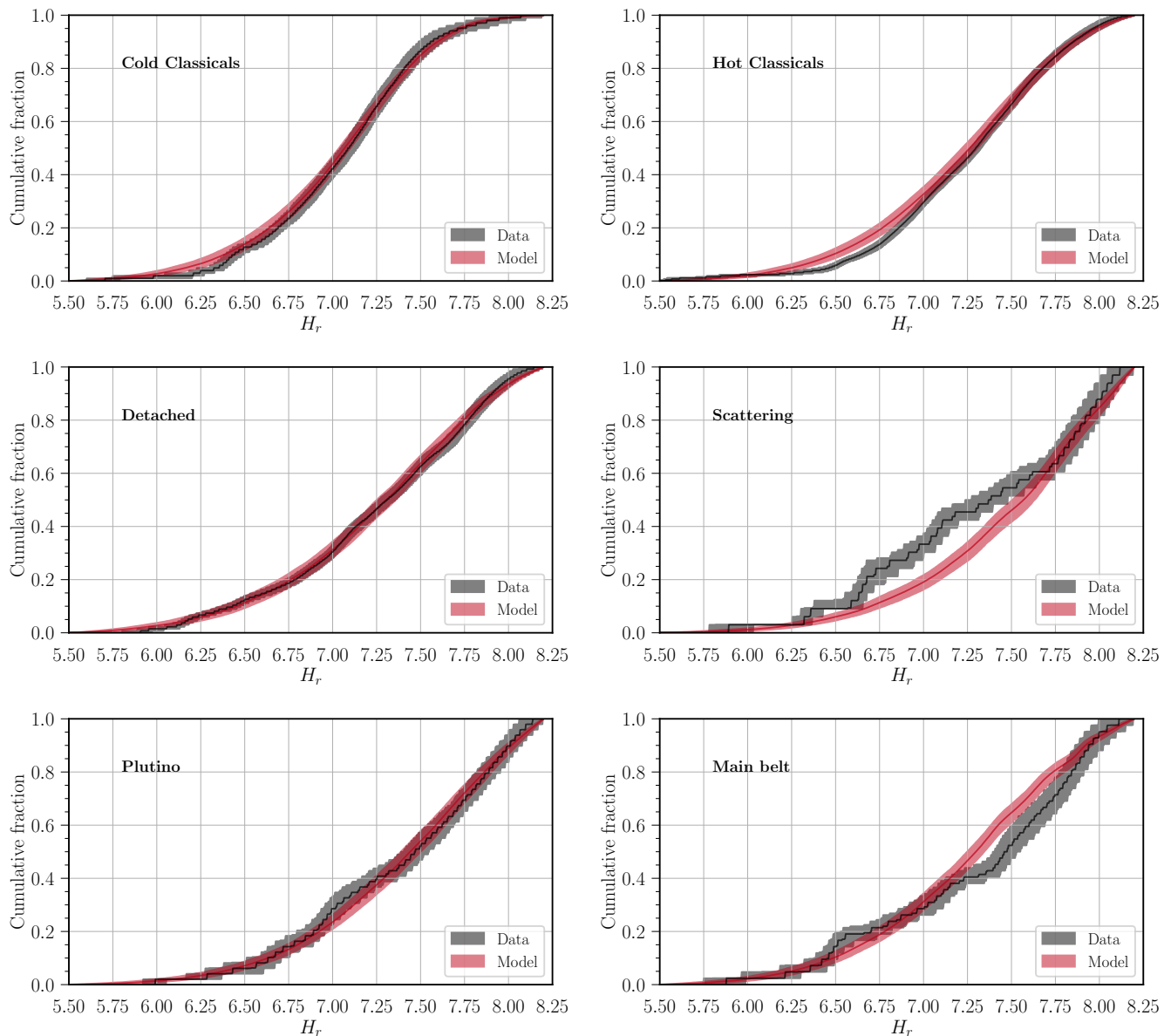


Figure 9. Each panel shows the 68% limits of the data distributions per dynamical class (black) as well as the best-fit $p(H_r)$ distribution multiplied by the selection function for the corresponding dynamical subset (red). In all cases, the data distribution has been constructed by sampling independent realizations of the H_r for each object, while the model distribution samples from the posterior of the likelihood.

In the previous section we constructed physical families based on 2 components of color distributions, and showed that the populations of the current dynamical families within a given color distributions have statistically indistinguishable H and A distributions, supporting the hypothesis that each dynamical family is a mixture of two common origin populations. Here we ask: Is there any evidence for the current dynamical classes to consist of *more* than 2 distinct physical families?

We approach this question by repeating the procedures of Section 4 but beginning with 3 color distributions instead of 2. Each of the GMM components listed in Table 1 is nearly a one-dimensional sequence through the 3-dimensional color space, as can be seen if one takes the eigenvalues $\lambda_1 >$

$\lambda_2 > \lambda_3$ of the covariance matrices: for both NIRB and NIRF, $\lambda_1 \approx 100\lambda_2 \approx 1000\lambda_3$. We split the NIRB component in half along its major axis, leaving us with three color components indexed by $\alpha \in \{\text{NIRB+}, \text{NIRB-}, \text{NIRF}\}$, where the + and - denote the redder and bluer halves of the sequence, respectively. We can then model each DES TNO dynamical population d as a mixture of components $\beta = (\alpha, d)$. If the H and A distributions of a given color component are consistent across dynamical classes, then these 3 color components are consistent with being the underlying constituents of all dynamical distributions. If we find evidence that $f_{\text{NIRB+}|d} \neq f_{\text{NIRB-}|d}$ for some class d , this would show that there is more differentiation of physical properties among the dynamical classes than can be fully described by our 2-component model. We can likewise ask these questions when splitting the NIRF component into redder and bluer halves to look for differential contributions to the dynamical classes.

Mathematically, this construction can be defined by changing the vector basis of the vector $\mathbf{c} - \boldsymbol{\mu}_{\text{NIRB}}$ in Equation 1 to the basis formed by the eigenvectors of Σ_{NIRB} . Calling this new vector $\mathbf{c}' = (c'_1, c'_2, c'_3)$, where the c'_i is the component corresponding to the eigenvalue λ_i , we can then define the probability distribution

$$p_{\text{NIRB}\pm}(\mathbf{c} | \boldsymbol{\mu}_{\text{NIRB}}, \Sigma_{\text{NIRB}}) \equiv \begin{cases} 2\mathcal{N}(\mathbf{c} | \boldsymbol{\mu}_{\text{NIRB}}, \Sigma_{\text{NIRB}}), & \text{if } c'_1 \geq 0 \\ 0, & \text{otherwise} \end{cases}. \quad (25)$$

These $p(\mathbf{c})$ distributions are properly normalized to $\int d\mathbf{c} p_{\text{NIRB}\pm}(\mathbf{c}) = 1$, although they are no longer Gaussian, and their mean colors are no longer $\boldsymbol{\mu}_{\text{NIRB}}$. The original 2-component GMM is nested within this model, as the case $f_{\text{NIRB+}|d} = f_{\text{NIRB-}|d}$.

5.1. Splitting the NIRB component

We begin by evaluating differentiation within the more populous NIRB component. The model now has 3 physical components for each dynamical subpopulation d , with the fractions constrained to the triangular face of a simplex defined by $f_{\text{NIRB+}|d} + f_{\text{NIRB-}|d} + f_{\text{NIRF}|d} = 1$. The natural prior for the f 's is uniformity across this triangle, which is described by the Dirichlet distribution (a.k.a. multivariate β distribution) with parameters $\alpha_i = -1$.

As in Section 4.1, we test whether the lightcurve parameters (\bar{A} and s) vary across the two halves of the NIRB component by finding a log evidence ratio of $\mathcal{R} = 1.771$, slightly favoring a shared distribution but not reaching Jeffrey's "strong" level. Similarly, the evidence that the two absolute magnitude distribution parameters θ, θ' are shared is $\mathcal{R} = -0.475$. The evidence that all four parameters physical parameters are shared is $\mathcal{R} = 1.180$. The DES data thus neither favor nor disfavor a shared distribution strongly. For simplicity, we proceed with the model where the NIRB+ and NIRB- populations do share H_r and A distributions.

After marginalizing over the $p_\beta(H)$ and $p_\beta(A)$ parameters, we test for differences in the ratio of NIRB+ to NIRB- occupation in the $f_{\text{NIRB},\pm}$ posterior distributions for the NIRB-dominated classes. The posterior samples of the set of $\{f_\alpha\}$ for the HC, detached and scattering populations are presented in Figure 10. In each panel, we also show the contours of the Dirichlet distribution that best fits the sampled $\{f_\alpha\}$ values, using the maximum likelihood method of (Minka 2000) to derive Dirichlet parameters.

The visual impression is that the detached TNOs (and probably the scattering objects) preferentially lie on the red side of the NIRB locus, with the HCs favoring the blue side. This difference is confirmed by an evidence ratio of $\mathcal{R} = -4.043$ showing very strong evidence that the HC and

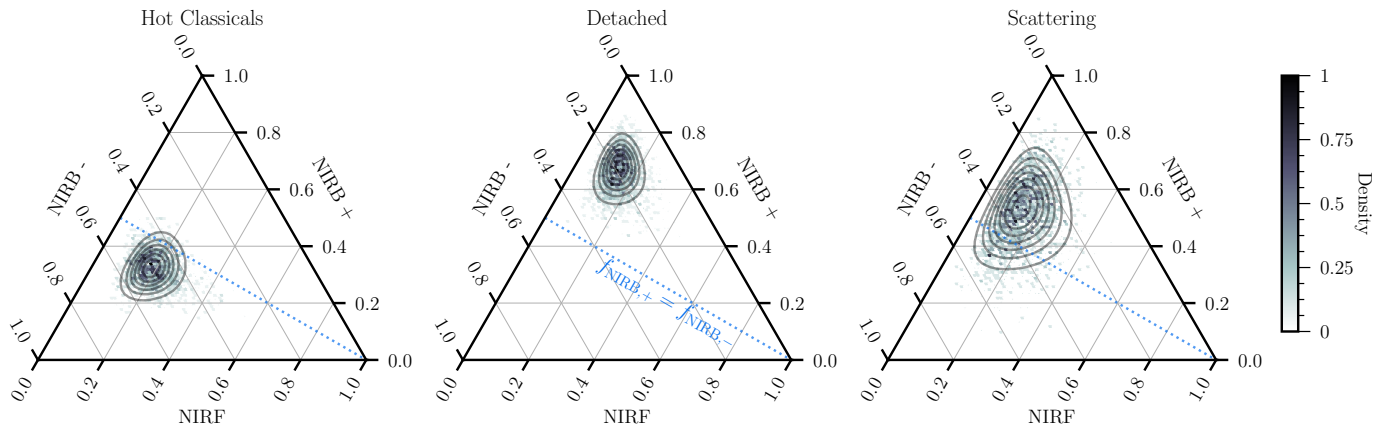


Figure 10. Ternary histograms of $(f_{\text{NIRF}}, f_{\text{NIRB}+}, f_{\text{NIRB}-})$ posterior samples HC, detached, and scattering populations are plotted as gray points in the three panels. Also plotted are contours of the 3-dimensional Dirichlet distribution that best fits the sampled $\{f_{\alpha}\}$. The blue dotted line represents the locus where $f_{\text{NIRB}+} = f_{\text{NIRB}-}$, indicating equal occupancy of the two sides of the NIRB Gaussian distribution.

detached populations do *not* share a common ratio of $f_{\text{NIRB}+}$ to $f_{\text{NIRB}-}$. A shared ratio for the scattering and detached objects is strongly favored by $\mathcal{R} = 2.673$, while the evidence for shared HC and scattering parameters is inconclusive at $\mathcal{R} = 0.224$.

While the fraction f_{NIRB} is nearly identical for the HC, detached, and scattering populations, their distributions *within* the NIRB color sequence do not agree, indicating a deviation from the two-component model. This would require the existence of a spatial gradient of color within the NIRB birth population, with subsequent differential migration into the HC vs the detached (and possibly scattering) population. Alternatively, post-migration surface color changes were different for the HCs than the detached objects.

5.2. Splitting the NIRF component

Next we test for differences in the occupation of the NIRF component. This time, we can include constraints for the primarily-NIRF CC population. We begin by allowing distinct values of (\bar{A}, s) on the red and blue sides of the NIRF component. We see that the two values for \bar{A} are nearly identical in the two populations. The sharpness parameters disagree, however: $s_{\text{NIRF},+} = 1.12 \pm 0.10$, $s_{\text{NIRF},-} = 0.66 \pm 0.10$. This 3.1σ difference in s leads to an evidence ratio $\mathcal{R} = -4.552$ against a common distribution. This implies that the distribution of lightcurve amplitudes is broader for redder NIRF TNOs. We do not see a significant difference in the (θ, θ') parameters between the NIRF+ and NIRF- populations, with evidence ratio $\mathcal{R} = -1.398$. Thus, we proceed with two NIRF components that differ only in their LCA distributions, but share their H_r distributions.

We can also evaluate the distribution of the $f_{\text{NIRF},\pm}$ for each of the dynamical classes. Figure 11 shows the distribution of $\{f_{\alpha}\}$ for the CC, HC, detached and scattering objects. Defining $f_{-|\text{NIRF}} = f_{\text{NIRF}-}/(f_{\text{NIRF}+} + f_{\text{NIRF}-})$ to denote the fraction of NIRFs on the blue side of the sequence, we have that the CC population has $f_{-|\text{NIRF}} = 0.57 \pm 0.07$, consistent with equal membership in the two components. The evidence ratio for the hot Classicals, detached and scattering objects is $\mathcal{R} = 5.504$, showing decisive evidence for a shared distribution among the three populations, where we find $f_{-|\text{NIRF}} = 0.247 \pm 0.039$, 4σ below the CC value.

6. THE INCLINATION DISTRIBUTION FOR THE NIRB AND NIRB POPULATIONS

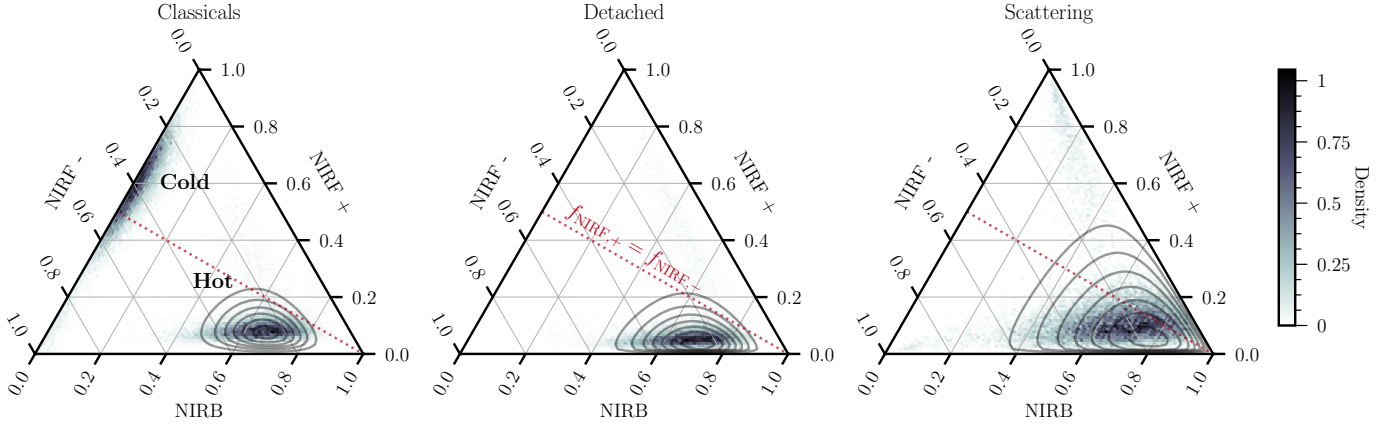


Figure 11. Similar to Figure 10, but showing $(f_{\text{NIRB}}, f_{\text{NIRF}+}, f_{\text{NIRF}-})$ posterior samples. The red dotted line represents the locus where $f_{\text{NIRF}+} = f_{\text{NIRF}-}$. The first panel shows both the Hot and Cold Classical posterior samples.

6.1. Measuring the inclination distribution

As demonstrated in Section 4 and Figure 8, f_{NIRB} seems to depend on inclination within the HC population. To quantify this trend, we measure the inclination distribution of the NIRB and NIRF components of the trans-Neptunian populations. Since *DES* has substantial coverage to high ecliptic latitudes, this test will also provide strong constraints to the shape of the inclination distribution for each dynamical subpopulation. In addition, Huang et al. (2022) compute “free” inclinations (I_{free}) for all *DES* main belt TNOs. This quantity is better conserved over the age of the Solar System for members of the classical population, and so is preferred to the ecliptic inclination when measuring the inclination distribution of this population. We also use this methodology to estimate I_{free} for the simulated objects used to determine the completeness functions, so that we can measure $p(\mathcal{S}|I_{\text{free}})$.

The framework presented in Section 3 still applies for this test, as we can safely assume that the measurements of inclination for each object are essentially noiseless.

We use the von Mises-Fischer distribution (Matheson et al. 2023; Malhotra & Roy 2023) as a convenient and statistically well-motivated functional family for the inclination distribution,

$$p(I|\kappa) = \frac{\kappa}{e^{\kappa} - e^{-\kappa}} \exp(\kappa \cos I) \sin I, \quad (26)$$

where κ is the concentration parameter. For large κ , the distribution peaks at inclinations $I \approx \kappa^{-1/2}$ radians (see Matheson et al. 2023 for a full derivation and discussion). This means that larger κ imply a more concentrated distribution, that is, a distribution with lower inclination objects. To improve the numerical stability of the HMC procedure and impose the (necessary) constraint that $\kappa > 0$, we will use $\log \kappa$ as the free parameter in our likelihoods.

6.2. Inclination distribution of the joint physical + dynamical subpopulations

Figure 12 shows the $\log \kappa$ posterior distributions within each dynamical subset, in models where there are distinct κ_{NIRB} and κ_{NIRF} (in blue and red, respectively), or when the whole dynamical subpopulation shares a common κ (in gray). Among the non-resonant classes, only the HCs decisively favor a “color-inclination bimodality,” with a more concentrated NIRF component (larger κ). This does not mean, however, that there are no NIRF objects with high inclinations: as can be seen

from Figure 3, the most inclined NIRF HC has $I = 42.3^\circ$. It does mean, however, that the current dynamical states of the HCs retain some memory of whether they originated in the birth region of the NIRF colors vs the NIRB colors. For the scattering and detached classes, the NIRB and NIRF classes have been mixed by migration processes so that they are dynamically indistinguishable in the DES catalogs.

A similarly decisive result is also seen for the resonant TNOs within the main belt range of a . The Plutinos yield an \mathcal{R} that is slightly above Jeffreys’s threshold for “strong” evidence favoring inclination segregation of the NIRB and NIRF members.

In the previous sections, we have treated the classical component of the Kuiper belt as two distinct subpopulations, HC and CC, split by I_{free} . By dividing the classicals strictly by NIRB or NIRF color and introducing distinct inclination parameters κ_{NIRB} and κ_{NIRF} , we can ask whether the HC NIRFs are consistent with being the high- I tail of the CC population, as opposed to having the HC and CC NIRFs be distinct. Our data decisively rule out this scenario of a single NIRF component describing the (free) inclination distribution of both the cold and hot classical populations. The very negative \mathcal{R} value in the lower row of the left panel of Figure 12 rejects this case in favor of a trimodal classical distribution composed of a CC population heavily concentrated on the invariable plane, a less concentrated group of NIRF HCs, and an even more inclined group of NIRB HCs.

We also test whether there is any detectable distinction between the inclination distributions of the blue and red halves of the NIRB distribution, as defined in Section 5. This is done by comparing the evidence ratio between a hypothesis with a single κ_{NIRB} vs a model with distinct $\kappa_{\text{NIRB+}}$ and $\kappa_{\text{NIRB-}}$. Neither the HCs ($\mathcal{R} = 0.678$), nor scattering ($\mathcal{R} = -0.805$), nor detached ($\mathcal{R} = -0.438$) populations exhibit any strong preference between a joint vs common inclination width of the red and blue ends of the NIRB sequence.

Figure 13 allows visual examination of whether the von Mises-Fischer distributions are a good model for the inclination distributions of each dynamical classes. For the CC, scattering, Plutino and main belt resonant populations, the best-fit von Mises-Fischer distributions for the NIRF and NIRB components sum to a cumulative I distribution that is a good visual match to the data. The HC and detached populations however, indicate poor fits, as has also been noticed by Malhotra & Roy (2023) for the HC case—the actual distributions are more “hollowed out” at low inclinations than the models. Further investigation of alternative functional forms, then, is needed to find a more statistically appropriate description of these populations. Despite these differences, the HC NIRF/NIRB bimodality is still statistically robust. Furthermore, it explains the trend seen in Figure 8 (which does not impose any model to the inclination distribution).

6.3. Population estimates

With the outputs of all the Markov chains in hand, we can use the Poisson distribution for N derived in Equation 16 to infer the number of objects in a range of H_r for each trans-Neptunian subpopulation. For dynamical subset d with $N_{\text{sample},d}$ objects in our sample, maximum-posterior estimate of the total number of objects N_d in the $H_{r,\text{min}} \leq H_r \leq H_{r,\text{max}}$ range (from Equation 17) is

$$N_d = \frac{N_{\text{sample},d}}{\sum_{\beta} f_{\beta} S_{\beta}} \int_{H_{r,\text{min}}}^{H_{r,\text{max}}} dH_r \sum_{\beta} f_{\beta} p_{\beta}(H_r). \quad (27)$$

In principle, the total number of objects over ranges of other characteristics can be similarly computed. The uncertainty in these numbers can be directly estimated by sampling from the chains, and

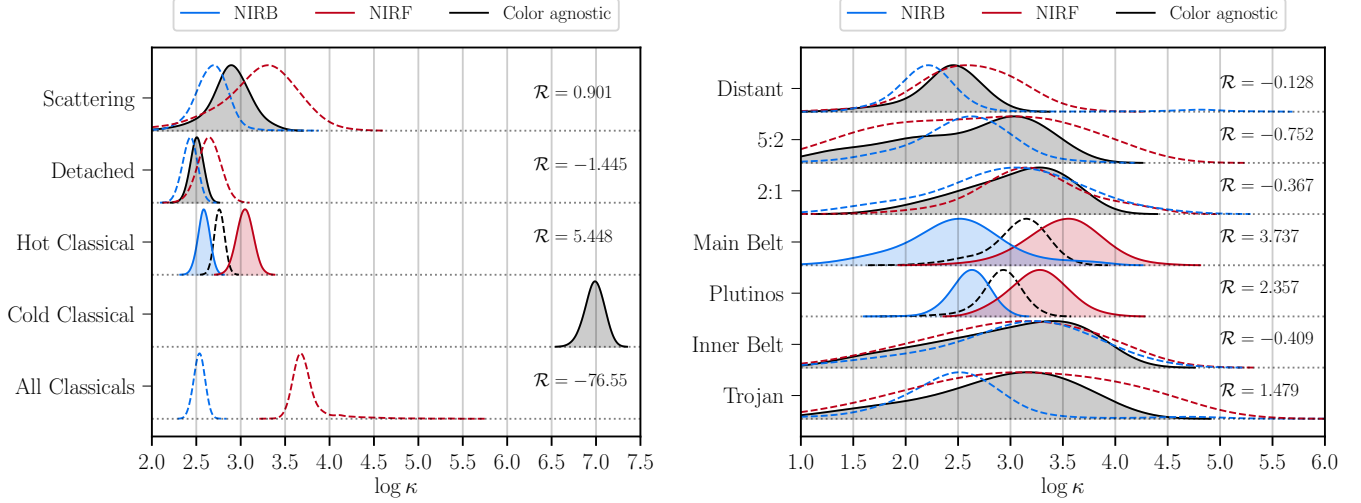


Figure 12. Histograms of the posterior samples for the inclination distribution concentration $\log \kappa$, with each row representing one dynamical subpopulation. The blue (red) curves represent the NIRB (NIRF) component, while the black curves represents the case where the two color components share their inclination distribution. In all cases, the shaded curve with the solid line represents the statistically preferred model, with the alternative option having a dashed curve. The evidence ratio \mathcal{R} for each subset is also shown, and a positive value shows a preference for the two component model. The left panel shows the non-resonant populations, with the last set of distributions representing the posteriors for the set of all Classical objects, while the two rows above it represent the Cold and Hot Classical subsets. The right panel shows the resonant populations. The Cold Classicals are dominated by the NIRF component, so the NIRB distribution is unconstrained. In this case, we present only the color agnostic model. Similarly, the Trojan and 5:2 resonators are primarily dominated by the NIRB component, and so the NIRF component is poorly constrained.

accounting for Poisson fluctuations in the number of detections by replacing $N_{\text{sample},d}$ by a random draw from a Poisson distribution with this mean value. We present these estimates for all of our subsets in Table 4. For each population d , we use either a single inclination distribution or distinct NIRB and NIRF inclination distributions, whichever is preferred by the Bayesian evidence ratios in Section 4. Our uncertainty estimates do *not* include uncertainties in the completeness corrections derived in Appendix D. The S_β have the most noise for types of orbits and H values that are likely to generate $\lesssim 1$ detection in the DES observations, and the number estimates will not include any portions of a dynamical class whose H and orbits bring them into observability by DES. One must be careful in comparing population estimates of the detached objects, in particular, to others results, to insure that the selection regions and/or extrapolation into unselectable regions are comparable.

We can also use these results to derive mass estimates, for a given choice of albedo and density. To relate our absolute magnitude to a TNO volume, following Russell (1916), we have for a spherical body with uniform surface:

$$H_r = m_{\odot,r} - 2.5 \log_{10} \frac{\nu_r R^2}{(1 \text{ au})^2} \quad (28)$$

$$\implies R(H_r) = \frac{1.496 \times 10^8 \text{ km}}{\nu_r^{1/2}} 10^{-0.2(H_r - m_{\odot,r})} \quad (29)$$

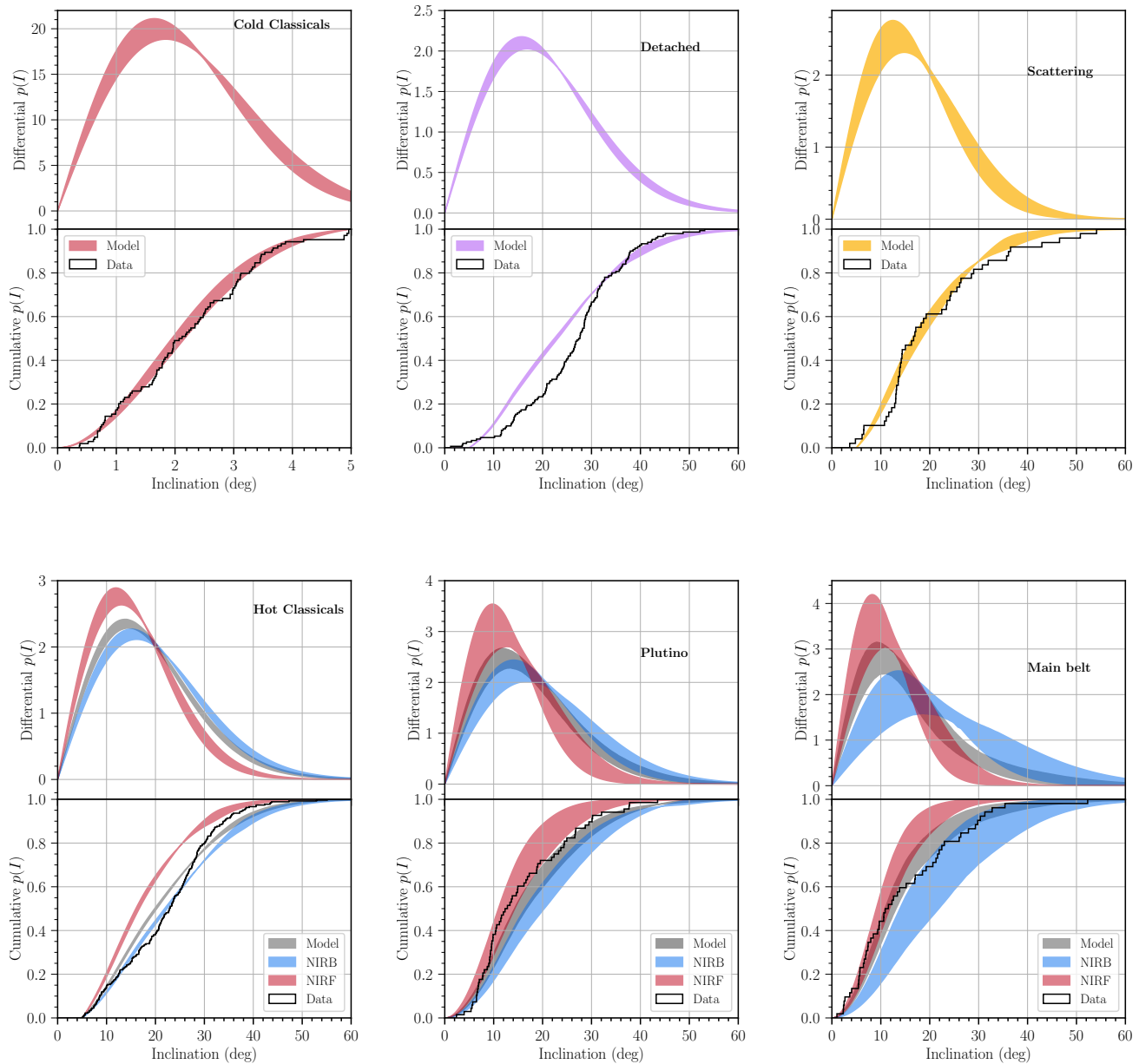


Figure 13. Each panel has differential (top) and cumulative (bottom) histograms of the 68% confidence range of the model inclination distributions fit to the labelled dynamical class, where the model either a single von Mises-Fischer distribution or the sum of two for the NIRF and NIRB components (whichever is preferred by the evidence ratio). The model curves include the observational selection function. The cumulative distribution of the detected TNOs is shown in black. The cold and hot Classicals show the free inclination (instead of the ecliptic inclination), and had their cumulative histograms truncated to $I_{\text{free}} < 5$ deg and $I_{\text{free}} > 5$ deg, respectively. In addition to the best-fit model, the hot Classical, Pluto and main belt resonant population also shows the confidence limits for the NIRB (blue) and NIRF (red) model components. The detached and HC inclination distributions are not as well fit by the models.

where $m_{\odot,r} = -26.96$ is the magnitude of the Sun (Willmer 2018), ν_r is the geometric albedo in the r band and R is the radius. For a spherical object, $V = 4\pi R^3/3$, but approximately zero of our TNOs are likely to be spherical. A crude estimate of the effect of asphericity on the volume estimate of a TNO with given lightcurve-averaged apparent magnitude H_r comes from considering an oblate spheroid rotating around a short axis normal to the line of sight. If the short and long semi-major axes of the body are a and c , respectively, then the minimum apparent flux is $f_{\text{mean}}(1 - A) \propto a^2$, and the lightcurve maximum is $f_{\text{mean}}(1 + A) \propto ac$, hence $c/a = (1 + A)/(1 - A)$. The volume is $V = 4\pi a^2 c/3 = 4\pi R^3(1 + A)\sqrt{1 - A}/3$ if R is derived from Equation 29 using the mean flux to estimate H . Integrating the $(1 + A)\sqrt{1 - A}$ factor over the A distributions that best fit the NIRB and NIRF populations leads to $\lesssim 5\%$ changes in the estimated mean volume from the spherical ($A = 0$) case. This is much smaller than the uncertainties in albedo and density, so we will ignore shape effects.

The total mass of the population, then, becomes:

$$M = \int dH_r n(H_r)M(H_r) = N \sum_{\beta} f_{\beta} \int dH_r p_{\beta}(H_r)M(H_r) \quad (30a)$$

$$= N \times K \times \sum_{\beta} f_{\beta} \frac{\langle \rho_{\beta} \rangle}{\langle \nu_{r,\beta} \rangle^{3/2}} \int dH_r p_{\beta}(H_r) 10^{-0.6H_r}, \quad (30b)$$

where

$$K = \frac{4\pi}{3} \times 10^{0.6m_{\odot,r}} \times (1.496 \times 10^8 \text{ km})^3 \quad (31)$$

is a constant. Note that we have taken the average albedo ν_r and density ρ for each family β . As we can adopt $p_{\text{NIRF}}(H_r) = p_{\text{NIRB}}(H_r)$ within the accuracy of the DES survey, the sum over the species β then only depends on potential differences in albedos and densities.

Lacerda et al. (2014) use thermal-IR measurements to estimate albedos, finding that the bluer objects have a mean albedo $\nu_r = 0.05$, while redder objects (such as CCs) are more reflective with $\nu_r = 0.15$. We adopt these values to be representative of our NIRB and NIRF classes, respectively. Trans-Neptunian densities are less constrained for objects in our size range, requiring a combination of a well measured binary system and either occultation even or thermal measurements are needed to obtain the size of each object. Following Müller et al. (2020), we adopt a reference value of $\rho = 1 \text{ g/cm}^3$ for both classes.

We report our mass estimates in our reference size range, as well as extrapolations to $5 \leq H_r \leq 12$, in Table 4. We note that while DES can only observe the L4 Trojan cloud (Lin et al. 2019), the simulation of Appendix D implies that the figures given for total Trojan counts inherit an assumption of equal occupation of the L4 and L5 clouds.

7. DISCUSSION AND IMPLICATIONS

The analysis presented herein is purely data-driven: no pre-existing population models of the TNO population were assumed, aside from the separability of the \mathbf{c} , H_r , and A distributions within a physical family, and rotational symmetry round the ecliptic plane for the populations of non-resonant TNOs. This leads to statistically robust constraints—our measurements are “observable” properties of the TNO sample that are valid for any population model. We have not coupled the color distributions with specific models of planetesimal formation and migration models, as done *e.g.*

Table 4. Population estimates

Subset	Number of objects $5.5 \leq H_r \leq 8.2$			Mass estimates ($\times 10^{-4} M_{\oplus}$)			
	Joint	NIRB	NIRF	$5.5 \leq H_r \leq 8.2$	NIRB	NIRF	$5 \leq H_r \leq 12$
CKBO	5556^{+606}_{-595}	64^{+72}_{-40}	5477^{+607}_{-583}	$2.69^{+0.41}_{-0.36}$	$0.15^{+0.17}_{-0.09}$	$2.51^{+0.35}_{-0.33}$	$7.39^{+1.12}_{-0.93}$
HKBO	11487^{+816}_{-815}	6599^{+636}_{-612}	4866^{+612}_{-566}	$18.0^{+1.4}_{-1.3}$	$15.8^{+2.2}_{-2.2}$	$2.23^{+0.36}_{-0.31}$	$49.4^{+5.7}_{-4.9}$
Detached	17878^{+1775}_{-1627}	12147^{+1524}_{-1373}	5654^{+1078}_{-948}	$31.7^{+4.9}_{-4.7}$	$29.0^{+4.8}_{-4.3}$	$2.59^{+0.58}_{-0.48}$	$87.2^{+11.6}_{-10.3}$
Scattering	2298^{+448}_{-419}	1525^{+380}_{-341}	738^{+284}_{-228}	$3.97^{+1.06}_{-0.86}$	$3.62^{+1.04}_{-0.85}$	$0.34^{+0.14}_{-0.11}$	$10.9^{+2.6}_{-2.3}$
Trojan	139^{+78}_{-56}	93^{+57}_{-41}	43^{+38}_{-24}	$0.25^{+0.15}_{-0.10}$	$0.22^{+0.15}_{-0.11}$	$0.02^{+0.01}_{-0.01}$	$0.68^{+0.39}_{-0.28}$
Inner belt	621^{+173}_{-173}	342^{+145}_{-119}	253^{+130}_{-96}	$0.94^{+0.37}_{-0.30}$	$0.81^{+0.37}_{-0.29}$	$0.12^{+0.06}_{-0.05}$	$2.59^{+0.96}_{-0.80}$
Plutinos	2453^{+372}_{-343}	1312^{+289}_{-248}	1312^{+274}_{-236}	$3.66^{+0.81}_{-0.371}$	$3.13^{+0.78}_{-0.68}$	$0.51^{+0.14}_{-0.12}$	$10.1^{+2.1}_{-1.8}$
Main belt	6042^{+1026}_{-921}	1682^{+726}_{-709}	4292^{+1100}_{-888}	$5.9^{+1.8}_{-1.5}$	$4.0^{+1.8}_{-1.7}$	$1.9^{+0.5}_{-0.4}$	$16.5^{+4.8}_{-4.3}$
2:1	3358^{+866}_{-769}	1186^{+569}_{-470}	2092^{+736}_{-604}	$3.8^{+1.5}_{-1.1}$	$2.8^{+1.4}_{-1.1}$	$0.96^{+0.35}_{-0.29}$	$10.6^{+3.8}_{-3.2}$
5:2	2818^{+894}_{-771}	2189^{+695}_{-803}	553^{+444}_{-294}	$5.5^{+2.0}_{-1.7}$	$5.2^{+2.0}_{-1.6}$	$0.25^{+0.20}_{-0.13}$	$15.1^{+5.5}_{-4.6}$
Distant	15146^{+2610}_{-2800}	8969^{+2318}_{-2029}	5913^{+2024}_{-1625}	$24.2^{+6.2}_{-5.3}$	$21.3^{+6.2}_{-5.1}$	$2.7^{+1.0}_{-0.8}$	67^{+17}_{-14}
Total	77155^{+11795}_{-6242}	36250^{+4488}_{-6190}	38678^{+18649}_{-5531}	104^{+14}_{-14}	85^{+15}_{-17}	18^{+8}_{-3}	288^{+34}_{-30}

NOTE—All values correspond to the 68% confidence limits derived from the HMC chains.

by [Buchanan et al. \(2022\)](#), instead discussing herein the general properties that any model must have to be consistent with our data, and supplying enough information that any investigator can check quantitative compatibility of their model with our inferences on the true population.

7.1. Framework

The analysis of the full DES population requires novel techniques for statistical inference of physical and dynamical properties from the largest catalog to date of trans-Neptunian objects orbital elements, absolute magnitudes, colors, and lightcurve amplitudes. The DES catalog differs from the ColOSSOS data used by [Fraser et al. \(2023\)](#) to investigate color distributions in that ColOSSOS obtains followup multiband observations, usually 1 object at a time, of a subset of OSSOS discoveries, aiming to integrate long enough to place each source unambiguously in *e.g.* one of the modes of the $g - r$ color distribution, which is a substantial investment in telescope time, and requires careful treatment of the selection process and success rate for followup. DES, on the other hand, has color data over the complete sample without the need for expensive followup data or additional selection effects—but the per-object color uncertainties for many members of the sample are too large to resolve the color differences between families. Our methods must therefore accommodate probabilistic assignment of individual objects to test population models. The reliability of such results depends critically on having accurate estimates of the flux uncertainties and selection criteria of the survey. Fortunately, for a multi-purpose sky survey such as DES or the upcoming LSST, there are many science pursuits that require, and will share the effort to obtain, careful point-source characterization.

Characterization of the variability distribution of TNOs has also generally been limited to sources with dedicated followup observations, which are expensive and involve some bias in the choice of followup targets. Studies such as [Showalter et al. \(2021\)](#) that collect data from the literature are additionally subject to a strong unknown “publication bias,” in that many observers will only publish light-curve data if variability is strongly detected, with poor or absent characterization of upper limits

for other sources. The many observations per source in DES allow us to produce a well-characterized $p(A)$ for every source, even if there is no definitive detection of variability, and combine these into constraints on the underlying distributions.

We have adapted the Gaussian mixture model technique to accommodate the inference of underlying color distributions from data with varying levels of measurement error and unknown number of clusters. The method allows us to infer, for example, a bimodality in the intrinsic $r - i$ color distribution (Figure 1), which is not visible in the ColOSSOS data of Fraser et al. (2023) and would not be apparent in a histogram of our point-estimate $r - i$ colors either. While tailored for our analysis of the color distribution of TNOs, the algorithm can be applied to any other similar clustering problems. The mathematical framework established in Section 3 substantially extends previous Bayesian analyses of trans-Neptunian size distributions, and enables a joint characterization of TNO colors, sizes, and lightcurve properties, as a function of families of objects and with rigorous treatment of measurement uncertainties, as well as perform robust hypothesis tests between competing representations of the data. Our methodology will scale gracefully to future data sets, particularly from the LSST (Ivezić et al. 2019), that will produce catalogs of 10–100× more TNOs than DES with multi-year astrometric and photometric data.

7.2. Two physical families across dynamical groups

Our unsupervised Gaussian mixture analysis independently arrives at a similar conclusion to Fraser et al. (2023): there are (at least) two color families in the TNO region, with the main color sequences “NIRB” and “NIRF” seen in Figure 1. The HC, detached and scattering objects, and most of the mean-motion resonances, are all NIRB-dominated, while the CCs are exclusively NIRF to within our measurement accuracy. With the fundamental assumption that surface colors in our H regime were established at birth, and the current paradigm that CCs were born *in situ* but the excited populations have been scattered outwards to their current locations, our data very strongly supports the conclusion that the NIRF population formed external to the region that sourced the NIRB component.

The interpretation of the color families as birth populations is bolstered by our finding that all members of the NIRB color sequence are consistent with a common absolute magnitude distribution, and a common variability distribution, independent of which dynamical class they currently occupy, and likewise for the NIRF TNOs.

Assuming that NIRF and NIRB colors are indeed established at birth, the NIRB/NIRF fractions of current dynamical populations inform their dynamical histories. We find that the populations of HC, scattering, and detached TNOs, plus the Neptune Trojans and most resonances, are consistent with $f_{\text{NIRB}} = 0.6$ to 0.7 . A common f_{NIRB} would mean that, to first order, these dynamical classes’ members are drawn from a common range of heliocentric birth distance, as would occur if their dynamical pathways all involved the same first step with a randomized final placement. An important exception is that the 5:3, 7:4, and possible 2:1 resonances each contain significantly larger fraction of NIRF TNOs than the other dynamically excited classes. This would be the case if many of the 5:3 and 7:4 resonators were formed as CCs close to their current semi-major axes, fell into their resonances after or in the late stages of Neptune’s migration, then had their inclinations excited by, for example, Kozai cycles (Lykawka & Mukai 2005). They would be mixed in these resonances with NIRB objects transported during migration.

With the larger samples from LSST, it should be possible to measure f_{NIRB} more precisely in each class and resonance, and see if any further differentiation of dynamical pathways is discernible.

7.3. Comparing NIRF and NIRB

The DES data are consistent with *all* TNOs sharing a common H (and presumably size) distribution in the range $5.5 < H_r < 8.2$ (Figure 5). This pushes the agreement in $p(H)$ noted among dynamical classes by Adams et al. (2014) to a magnitude deeper, and extends the common $p(H)$ noted between the two modes of $g - i$ color by Wong & Brown (2017), and between the dynamically cold and hot populations by Petit et al. (2023). The preference for a rolling power-law distribution for all dynamical subpopulations also agrees with the deviation from a single power law seen in the Plutino population by Alexandersen et al. (2016) and in the scattering population by Lawler et al. (2018). Our result, then, brings together several hints of a universal $p(H)$ in this size range seen in other datasets. This is a strong argument that the physical process of planetesimal formation was coherent across the entire span of TNO’s birth populations, despite the change in local environments implied by the NIRF/NIRB color transition and some heliocentric radius. Any subsequent collisional evolution of the size distribution would need to be small and/or similar enough in the dynamically hot and cold populations to maintain the observed $p(H)$ agreement.

The light-curve amplitude distributions $p(A)$ are discernibly different between the NIRF and NIRB populations, in contrast to the common $p(H)$, with the NIRF TNOs being more photometrically variable than the NIRBs (Figures 4 and 6). This difference can be induced by the NIRF objects being less homogeneous in surface albedo; comprising higher-ellipticity bodies; having a higher fraction of contact binaries; having a stronger tendency of rotation poles to be normal to the ecliptic; or any combination of these effects (see Showalter et al. 2021, for a review). One economical hypothesis would be that all TNOs were created with spin poles close to normal to the ecliptic plane, which the NIRFs maintain, but having spin poles randomized during migration to make the NIRF objects more isotropic and less apparently variable. A weak argument against this scenario is that the only small CC with a known spin pole, Arrokoth, has its pole close to the ecliptic plane (Stern et al. 2019). This scenario also seems to be ruled out by our very strong determination that the dynamically excited NIRF population is more variable than the NIRB TNOs even when removing the CCs. As such, our analysis points towards surface features and shapes as the likely scenario, motivating further investigations of these trends using the upcoming LSST data.

7.4. Inclination information

The inclination-distribution measurements of the DES TNO populations in Section 6.2 improve on previous efforts by having larger numbers of sources, and by the substantial high-ecliptic-latitude coverage of the DES imaging. TNO emplacement models first must be able to reproduce the observed widths of each dynamical group’s inclination distribution (as measured by $\log \kappa$ in the von Mises-Fisher distribution), but also must reproduce any correlations with color.

7.4.1. Population widths

Figure 12 shows that the detached population has the broadest inclination distribution of all dynamical subpopulations (lowest $\log \kappa$), with the NIRB HCs and scattering populations similar or wider, as expected due to dynamical effects related to Neptune’s migration (Gomes 2003). Comparisons between our results and the inclination distributions produced by different migration scenarios, then,

are of interest (see, *e.g.* Nesvorný 2015a; Volk & Malhotra 2019). Similarly, our analysis also shows a rich structure in the inclination distribution of the resonant subpopulations, being an additional constraint for migration scenarios.

Our measurement of the cold Classical inclination distribution is in direct agreement with previous measurements (Van Laerhoven et al. 2019; Malhotra & Roy 2023), indicating the undisturbed nature of this population (Dawson & Murray-Clay 2012; Nesvorný 2015b; Batygin et al. 2020). Our data also conclusively exclude any hope that the the NIRF HCs are the high- I tail of the *in-situ* CC population, despite their similar physical properties.

The inclination distribution of our NIRF component of the HCs, $\kappa_{\text{NIRF}} = 20.9 \pm 1.9$, agrees with that measured for full HC population by Malhotra & Roy (2023), who report $\kappa = 19.7 \pm 1.9$, (2σ limits). Our analysis, however, demonstrates the need for two distributions, with a more inclined NIRB component with $\kappa_{\text{NIRB}} = 13.25 \pm 0.88$. As Malhotra & Roy (2023) used the entire Minor Planet Center (MPC) sample for their analysis, the agreement between their measurements and our NIRF components indicates that high- I HCs are relatively poorly represented in the MPC, reflecting the tendency for TNO surveys to target fields near the ecliptic plane. Furthermore, without the color information as a discriminant, there is no other simple way to decouple these two distributions, which explains why, since Brown (2001), the HC inclination distribution has been treated as a single component.

7.4.2. Inclination-color relations

Several of the tests in this paper search for additional information on the birth-to-present dynamical pathways beyond the basic NIRB/NIRF split. Essentially, we ask whether the current dynamical groups “remember” anything further about their birth circumstances beyond their f_{NIRB} value. Section 6.2 tests whether the current dynamical state, namely inclination, differs for the NIRF vs NIRB components of a given dynamical family. For the HC, detached, and scattering TNOs, we can consider the NIRF and NIRB members of the dynamical family to represent TNOs born in the outer and inner regions of their source population, respectively. As seen in Figure 12, the HCs show conclusive differences between the inclination distributions of their NIRF and NIRB populations. In each case, the NIRB population has lower κ (\Rightarrow higher inclinations) than the NIRF. For the HCs, this means that those that have migrated further in a (the NIRBs) have ended up with larger present-day inclinations.

The difference in inclination widths of the HCs’ NIRF and NIRB populations seen in Figure 12 also manifests as the inclination dependence of f_{NIRB} visible in Figure 8, and seen in previous works (*e.g.* Marsset et al. 2019). Such a correlation has been posited in the dynamical models of Nesvorný et al. (2020), but we note that our sample span a broader range of inclinations than those produced by their model. Marsset et al. (2023) claim that, beyond the color-inclination correlation, colors and inclinations are also correlated *within* their “brightIR” class for the HCs—similar to our NIRB population. Despite a $\gtrsim 3\times$ larger sample of HCs that span a broader range of inclinations than those used by Marsset et al. (2023), we were not able to detect differences in the inclination distributions for the redder and bluer halves of the HC NIRB population.

The right panel of Figure 12 shows that statistically significant differences in inclination widths are present between the NIRF and NIRB components of the combined 7:4 and 5:3 resonances lying within the classical belt; likewise for the 3:2 Plutinos just interior to the classical belt. These are the two resonance samples with the largest number of DES detections, hence similar patterns could be

present but undetected within other resonances. If the Main Belt resonants are a mix of migrated objects (mostly NIRB) with former CCs (which are NIRF) captured into the resonance near the end of (or after) Neptune’s migration, then the implication of our observations is that the migrated objects have moved into higher-inclination orbits than the former CC’s. The Plutinos also show evidence that higher inclinations are currently held by objects that have migrated longer distances within the resonance.

We also note an apparent disagreement between our f_{NIRB} for the Plutinos and the equivalent quantity measured by Pike et al. (2023): in our units, they report $f_{\text{NIRB}} \approx 0.11$, while we see $f_{\text{NIRB}} \approx 0.56$. This discrepancy could result from an underestimate of the high-inclination population in their sample, because we find that the higher- I Plutinos are more likely to be NIRB, leading to an underestimate of f_{NIRB} . The most inclined Plutino in the Pike et al. (2023) sample has $I = 24.9^\circ$, while our Plutinos extend to $I = 43.0^\circ$. This has also been noted by Collyer et al. (2024). Another point of comparison for the Plutinos is the measurement by Matheson et al. (2023) of $\kappa \in [27.3, 36.3]$ (3σ bounds) for the full sample of 431 reliably known Plutinos. Our result for the full DES Plutino population is $\kappa = 17.9 \pm 4.0$, which is 2σ below the lower 3σ bound of Matheson et al. (2023). We measure $\kappa_{\text{NIRF}} = 25.6 \pm 7.5$ and $\kappa_{\text{NIRB}} = 13.7 \pm 2.6$ —the former is consistent with their result, and it is possible that the methods for correcting for completeness of the full MPC sample are under-representing the higher- I , NIRB-dominated Plutinos.

7.5. Departures from a two-component model

A simple scenario has all CCs born exterior to some heliocentric radius while all dynamically excited TNOs form interior to this radius, with the boundary lying somewhat exterior to the primordial transition from NIRB to NIRF surfaces. The inclination studies provide strong evidence this scenario is inadequate, since the HCs and Main Belt resonators show different inclination distributions for NIRF and NIRB members, a “memory” of location within their birth regions. There are other statistically significant trends in the DES catalog that are in conflict with the simple two-zone scenario.

First, there are objects in the selected H_r range whose colors deviate significantly from the NIRB/NIRF model. While some of these can be assigned to the Haumea collisional family, whose unusual colors have been attributed to a relatively recent exposure of the interior of a large parent body, the other color outliers we identify require a different mechanism. One simple explanation is that these objects have poor photometric measurements, and high- S/N follow-up observations would show that these belong to the NIRB or NIRF classes. However, if our color measurements are accurate, another explanation will be needed: have these objects formed in different regions of the Solar System, then transported as interlopers into the trans-Neptunian region? Have these objects experienced unusual surface evolution, or, less likely, are these objects part of some other (unidentified) collisional family? These questions motivate followup observations of the outliers.

Second, we find in Section 5, and illustrated in Figures 10 and 11, that not all the dynamical classes sample equally from the red and blue ends of the NIRB and NIRF color sequences. Let us postulate (as per Nesvorný et al. 2020; Buchanan et al. 2022) that color distribution was determined by radius in the Solar System’s natal protoplanetary disk, with each color family being formed in a different stratum of the protoplanetary disk, and that migration processes are color-independent. Then if each of these regions (namely NIRF and NIRB) had a homogeneous color distribution, then any sampling of objects formed inside them would also produce a homogeneous distribution, and the NIRF (or NIRB) members of all dynamical classes must share a color distribution within the

NIRF (NIRB) locus. It is clear from our analysis, however, that this is not the case: The HC NIRBs are bluer, on average, than detached+scattering NIRBs. HC and detached NIRFs are significantly bluer, on average, than CC NIRFs. Two possibilities exist: one is that post-natal processing changes surface colors, *e.g.* some collisional evolution or radiolysis that depends on late-time location and/or dynamical state. A more interesting scenario, though, might be that there is some further radial compositional stratification or gradient within both the NIRB and NIRF formation regions, coupled with radius-dependent transport into the current HC and detached dynamical states. With the larger TNO samples and more definitive color assignments to be available from LSST, we might be able to better localize (in the current dynamical space) the regions of gradients in occupancy of the color loci, and use this to unwind the originating natal gradients and the differential transport mechanisms.

7.6. Population estimates

Comparison of our total population estimates (Table 4) with previous estimates reveals agreements and some puzzling discrepancies. Our estimates for the Plutino, 2:1 and 5:2 resonant populations agree with (at similar or better precision than) the OSSOS estimates (Volk et al. 2016; Chen et al. 2019); and our main belt populations (5:3 and 7:4) agree with the estimates given by Gladman et al. (2012), once we convert their H_g using the nominal $g - r$ for the NIRF population.

Our population estimate for the detached population is consistent with (and less uncertain than) that of Beaudoin et al. (2023), and shows that the size of the detached population is comparable to that of the main Kuiper belt. This large population size and the broad inclination distribution of the detached populations imply that a substantial fraction of TNOs that the upcoming LSST will find are from this population, although this population will be less represented in surveys of the ecliptic plane such as DEEP (Trilling et al. 2024). We should reiterate that detached TNOs with high perihelia that have zero selection probabilities at DES depth regardless of orbital phase will not be counted in our population estimates—direct comparison of different surveys’ estimates for this population should probably include careful matching of selection criteria.

Crompvoets et al. (2022) estimated that a large population of objects in distant resonances is needed to explain the number of such objects in the OSSOS (and accompanying) surveys. Here, we directly confirm their measurement: we see that the population of objects in resonances beyond 60 au is comparable to the detached population. These objects also have a wide inclination distribution and have a similar color occupation distribution to the detached population. It has been posited that a portion of the detached population is composed of “resonant dropouts,” objects that were transported by Neptune’s migration and were dropped off sunward of the resonance (see Nesvorný & Vokrouhlický 2016; Kaib & Sheppard 2016, see also Lawler et al. 2019 and Bernardinelli et al. 2022 for observational tests of this hypothesis). Such similarities, then, favor this common origin scenario for these two populations.

One discrepancy is that our total CC and HC population inferences are $1.5 - 1.8\times$ smaller than those of Kavelaars et al. (2021) and Petit et al. (2023) for the same H_r range. The best-fit absolute magnitude distribution from Kavelaars et al. (2021) with the normalization in Petit et al. (2023) predicts that DES would have discovered ≈ 150 CCs with the CFEPS-L7 orbital distribution model (Petit et al. 2011), whereas we find 102 (Table 2). The underlying surveys are fairly complementary: OSSOS is deeper, while DES is wider (with an effective CC search area of $\approx 200 \text{ deg}^2$). A careful joint analysis of the surveys would resolve this inconsistency. Despite such differences, Petit et al. (2023) report their ratio of HCs to CCs as 2.2, consistent with our 1.9 ± 0.2 .

Our total size for the scattering population is also inconsistent with that of [Lawler et al. \(2018\)](#): after scaling their absolute magnitude distribution to our limits: their reported population size is $\approx 2.3\times$ larger than ours. This discrepancy can be partially attributed to differences in the dynamical classification, that is, the distinction between scattering and detached objects, but also derived from our shallower H_r distribution. We note, however, that our population estimate for this population agrees with (and is less uncertain than) that of [Petit et al. \(2011\)](#).

Our population estimates show that the number of NIRB and NIRF objects are comparable in the entire TNO region: while the NIRB population is clearly dominant in the dynamically excited populations, these numbers are balanced by the large number of CKBOs and the abundance of NIRF in the main belt resonances and the 2:1 population. However, even with the comparable numbers, the majority of the trans-Neptunian mass comes from the NIRB population. This is primarily due to the smaller albedos, therefore demanding larger objects at the same H_r . This is compatible with scenarios where there is a transition in surface density in the protoplanetary disk (see, for example, [Nesvorný et al. 2020](#)). We note that, in the same size range, our mass estimates for the cold Classical belt are substantially smaller than those of [Petit et al. \(2023\)](#), who reports a $\approx 2.8\times$ larger mass for the entire cold belt when compared to ours, and [Napier et al. \(2024\)](#), who reports a $2.3\times$ larger mass. This difference can partially be traced to our inconsistent population sizes compared to [Petit et al. \(2023\)](#) (note that [Napier et al. 2024](#)’s small area leads to a poor constraint of the normalization or the bright end of the H_r distribution), and the less steep behavior of our best-fit $p(H)$ when extrapolated to $H_r > 8.2$.

8. SUMMARY

We examine the relations between the physical properties (color, size, shape) and the dynamical properties of the sample of 696 trans-Neptunian objects with $5.5 < H_r < 8.2$ detected in the Dark Energy Survey, which yield constraints on the “birth” locations and emplacement processes of TNOs currently in different dynamical states. All objects have, in addition to multiple years of astrometric observations, measurements of absolute magnitudes, colors, and lightcurve amplitudes, as well as well-characterized discoverability conditions. While the measurements of individual TNOs’ colors and lightcurve amplitudes are not all sufficiently precise to assign definitive color classifications or variability states, the uncertainties on all measurements are carefully characterized so that we can infer accurate population-level statistics using probabilistic assignments. Our main findings are as follows:

- We confirm and strengthen the observation by [Fraser et al. \(2023\)](#) that the colors of the great majority of TNOs lie within two narrow loci in *griz* color space, which we call near-infrared bright or faint (NIRB or NIRF), according to their relative *i* and *z*-band magnitudes at a fixed visible $g - r$ color. The parameters of the modelled Gaussian NIRB/NIRF color distributions are in [Table 1](#). There are statistically significant outliers, including but not limited to Haumea-family members, which could be interlopers from the inner solar system. ([Section 2](#), [Figure 1](#), discussion in [Section 7.2](#))
- The NIRB-colored members of all dynamical classes are consistent with sharing a common H_r distribution and common variability distribution. Likewise, the physical properties of NIRF-colored objects are independent of dynamical state, to the accuracy attained by the DES catalog. This is consistent with a scenario in which NIRF and NIRB color families are in fact

birth populations that have been dispersed into present-day dynamical states. (Sections 4.1, 7.2)

- The NIRB and NIRF populations share a common absolute-magnitude distribution over our H_r range, broadening the similarities in H distributions noted by Adams et al. (2014), Wong & Brown (2017), and Petit et al. (2023) among more limited TNO subsets. This implies a similarity in the planetesimal formation process in this size range across the heliocentric distance range that spans both the NIRF and NIRB birth regions. We fit a rolling power law to $p(H_r)$ and decisively exclude a simple power-law (no rolling) case, but we cannot distinguish between a rolling power law and other parameterizations of the curvature. (Section 4.2, Figure 5)
- On the other hand, objects from the NIRF component have significantly larger lightcurve amplitudes than those from the NIRB family, suggesting either some difference in birth shape/spin distributions, or some alteration during the migration of NIRB objects. The DES data do not have the power to discriminate these scenarios, but LSST data should. (Section 4.2, Figure 6, Section 7.3)
- We determine the fraction f_{NIRB} of each dynamical population, finding that the CCs are consistent with $f_{\text{NIRB}} = 0$, in agreement with many previous color-dynamic studies. Assuming the CCs were formed *in situ*, the NIRB population was formed interior to the NIRF. The HC, scattered, and detached TNOs are, at present precision, consistent with a common $f_{\text{NIRB}} \approx 0.7$, suggesting they share a common origin “footprint” (but see below). The mean motion resonances do, however, show significant variation in f_{NIRB} , with resonances lying within the classical belt being relatively rich in NIRF sources, consistent with some of these being CCs captured after the main Neptune migration was complete. (Section 4.3, Figure 7, Section 7.2)
- The inclination distribution of NIRF HCs is narrower than the inclination distribution of NIRB HCs, implying that the current HCs “remember” to some extent whether they were born in the inner NIRB vs outer NIRF part of the HC birth regions. Post-formation dynamics have *not* mixed all birth orbits into a common present-day phase space. A similar pattern of narrower inclination widths for NIRF colors is detected among Plutinos (3:2) and the Main Belt (7:3, 5:4) resonators. (Section 6.2, Figure 12, Section 7.4.)
- Features in the joint color-dynamics distribution of the DES TNOs require a more complex history than having just 2 physically homogeneous birth populations. The NIRB members of the HC population tend to be bluer than the NIRB members of the detached and scattering populations, and the NIRF members of the CC population favor the redder end of the NIRF sequence relative to the HC, detached, and (possibly) scattering populations. Unless there are post-migration surface color shifts, these observations require the occupation of each sequence to have differed as a function of heliocentric birth distance, along with radius-dependent selection into the current dynamical classes. (Section 5, Figures 10 and 11, Section 7.5)
- The combination of characterization in absolute magnitude and inclination allows us to derive population and mass estimates for all trans-Neptunian subpopulations represented in the DES dataset. We find that there are similar numbers of NIRB and NIRF objects in the trans-Neptunian region, but the NIRB population accounts for most of the trans-Neptunian mass

if the albedo trends described by [Lacerda et al. \(2014\)](#) are correct. The population number estimates are in apparent disagreement with other recent estimates, motivating some future joint analyses across surveys. (Section 6.3, Table 4, Section 7.6)

Our analysis is the first to our knowledge to try to simultaneously characterize multiple physical properties (color, size, lightcurve amplitudes) and dynamical information. While our own discussion offers general comments on the interpretation of the patterns that we have detected in the joint dynamical-physical space, we have not tested any specific scenarios against the data. We hope these results will serve as strong quantitative constraints for future models of the planetesimal formation and migration in the outer solar system, and motivate the creation of models that track both dynamical state and color/size of TNOs. The DES results show that the dynamical evolution from birth to present has *not* completely mixed the different birth regions into indistinguishable current states; there does remain information beyond the 2-population model in the current physical-dynamical distribution which can be used to discriminate dynamical histories. The > 10 -fold increase in sample size from LSST should sharpen these measures of differential birth properties and migration.

The HMC and likelihood computation software, as well as all data produced (completeness estimates and HMC chains) will be available for open use at https://github.com/berardinelli/des_tno_likelihood after acceptance of this contribution to the journal. The GMM package is provided as a standalone package at https://github.com/berardinelli/gmm_anyk.

ACKNOWLEDGMENTS

Contribution Statements: P. H. B. led the analysis, developed the GMM algorithm, implemented the numerical calculations and produced the figures and results. G. M. B. derived the likelihood form and produced the initial HMC code. P. H. B. and G. M. B. contributed equally to the text. All other authors have contributed to the construction and operation of the Dark Energy Survey.

Software: This work made use of the following public libraries: NUMPY ([Oliphant 2015](#)), SCIPY ([Jones et al. 2001–](#)), ASTROPY ([Astropy Collaboration 2013, 2018](#)), MATPLOTLIB ([Hunter 2007](#)), IPYTHON ([Pérez & Granger 2007](#)), NUMBA ([Lam et al. 2015](#)), JAX ([Bradbury et al. 2018](#)), SYMPY ([Meurer et al. 2017](#)), REBOUND and WHFast ([Rein & Liu 2012; Rein & Tamayo 2015](#)), GETDIST ([Lewis 2019](#)), MPLTERN ([Ikeda 2023](#))

We thank B. Proudfoot and D. Ragozzine for discussions related to the Haumea family, J. J. Kavelaars for discussions about the OSSOS absolute magnitude distribution, M. Belyakov for discussions about the color distribution results, and H. W. Lin for a thorough review of this manuscript prior to submission.

P.H.B. acknowledges support from the DIRAC Institute in the Department of Astronomy at the University of Washington. The DIRAC Institute is supported through generous gifts from the Charles and Lisa Simonyi Fund for Arts and Sciences, and the Washington Research Foundation. G.M.B. acknowledges support from NSF grants AST-1515804 and AST-2205808 during the course of this work.

This work used Anvil at Purdue University ([Song et al. 2022](#)) through allocation PHY240190 from the Advanced Cyberinfrastructure Coordination Ecosystem: Services & Support (ACCESS, [Boerner et al. 2023](#)) program, which is supported by National Science Foundation grants #2138259, #2138286, #2138307, #2137603, and #2138296

Funding for the DES Projects has been provided by the U.S. Department of Energy, the U.S. National Science Foundation, the Ministry of Science and Education of Spain, the Science and Technology Facilities Council of the United Kingdom, the Higher Education Funding Council for England, the National Center for Supercomputing Applications at the University of Illinois at Urbana-Champaign, the Kavli Institute of Cosmological Physics at the University of Chicago, the Center for Cosmology and Astro-Particle Physics at the Ohio State University, the Mitchell Institute for Fundamental Physics and Astronomy at Texas A&M University, Financiadora de Estudos e Projetos, Fundação Carlos Chagas Filho de Amparo à Pesquisa do Estado do Rio de Janeiro, Conselho Nacional de Desenvolvimento Científico e Tecnológico and the Ministério da Ciência, Tecnologia e Inovação, the Deutsche Forschungsgemeinschaft and the Collaborating Institutions in the Dark Energy Survey.

The Collaborating Institutions are Argonne National Laboratory, the University of California at Santa Cruz, the University of Cambridge, Centro de Investigaciones Energéticas, Medioambientales y Tecnológicas-Madrid, the University of Chicago, University College London, the DES-Brazil Consortium, the University of Edinburgh, the Eidgenössische Technische Hochschule (ETH) Zürich, Fermi National Accelerator Laboratory, the University of Illinois at Urbana-Champaign, the Institut de Ciències de l'Espai (IEEC/CSIC), the Institut de Física d'Altes Energies, Lawrence Berkeley National Laboratory, the Ludwig-Maximilians Universität München and the associated Excellence Cluster Universe, the University of Michigan, the National Optical Astronomy Observatory, the University of Nottingham, The Ohio State University, the University of Pennsylvania, the University of Portsmouth, SLAC National Accelerator Laboratory, Stanford University, the University of Sussex, Texas A&M University, and the OzDES Membership Consortium.

Based in part on observations at Cerro Tololo Inter-American Observatory, National Optical-Infrared Astronomy Observatory, which is operated by the Association of Universities for Research in Astronomy (AURA) under a cooperative agreement with the National Science Foundation.

The DES data management system is supported by the National Science Foundation under Grant Numbers AST-1138766 and AST-1536171. The DES participants from Spanish institutions are partially supported by MINECO under grants AYA2015-71825, ESP2015-66861, FPA2015-68048, SEV-2016-0588, SEV-2016-0597, and MDM-2015-0509, some of which include ERDF funds from the European Union. IFAE is partially funded by the CERCA program of the Generalitat de Catalunya. Research leading to these results has received funding from the European Research Council under the European Union's Seventh Framework Program (FP7/2007-2013) including ERC grant agreements 240672, 291329, and 306478. We acknowledge support from the Australian Research Council Centre of Excellence for All-sky Astrophysics (CAASTRO), through project number CE110001020, and the Brazilian Instituto Nacional de Ciência e Tecnologia (INCT) e-Universe (CNPq grant 465376/2014-2).

This manuscript has been authored by Fermi Research Alliance, LLC under Contract No. DE-AC02-07CH11359 with the U.S. Department of Energy, Office of Science, Office of High Energy Physics. The United States Government retains and the publisher, by accepting the article for publication, acknowledges that the United States Government retains a non-exclusive, paid-up, irrevocable, world-wide license to publish or reproduce the published form of this manuscript, or allow others to do so, for United States Government purposes.

REFERENCES

- | | |
|--|--|
| <p>Adams, E. R., Gulbis, A. A., Benecchi, S. D., et al. 2014, <i>Astronomical Journal</i>, 148, 55, doi: 10.1088/0004-6256/148/3/55</p> | <p>Alexandersen, M., Gladman, B., Kavelaars, J. J., et al. 2016, <i>The Astronomical Journal</i>, 152, 111, doi: 10.3847/0004-6256/152/5/111</p> |
|--|--|

- Astropy Collaboration. 2013, *A&A*, 558, A33, doi: [10.1051/0004-6361/201322068](https://doi.org/10.1051/0004-6361/201322068)
- . 2018, *AJ*, 156, 123, doi: [10.3847/1538-3881/aabc4f](https://doi.org/10.3847/1538-3881/aabc4f)
- Barucci, M. A., Belskaya, I. N., Fulchignoni, M., & Birlan, M. 2005, *The Astronomical Journal*, 130, 1291, doi: [10.1086/431957](https://doi.org/10.1086/431957)
- Barucci, M. A., Fulchignoni, M., Birlan, M., et al. 2001, *Astronomy and Astrophysics*, 371, 1150, doi: [10.1051/0004-6361:20010501](https://doi.org/10.1051/0004-6361:20010501)
- Batygin, K., Adams, F. C., Batygin, Y. K., & Petigura, E. A. 2020, doi: [10.3847/1538-3881/ab665d](https://doi.org/10.3847/1538-3881/ab665d)
- Beaudoin, M., Gladman, B., Huang, Y., et al. 2023, *The Planetary Science Journal*, 4, 145, doi: [10.3847/PSJ/ace88d](https://doi.org/10.3847/PSJ/ace88d)
- Bernardinelli, P. H., Bernstein, G. M., Sako, M., et al. 2020a, *The Astrophysical Journal Supplement Series*, 247, 32, doi: [10.3847/1538-4365/ab6bd8](https://doi.org/10.3847/1538-4365/ab6bd8)
- . 2020b, *The Planetary Science Journal*, 1, 28, doi: [10.3847/PSJ/ab9d80](https://doi.org/10.3847/PSJ/ab9d80)
- . 2022, *The Astrophysical Journal Supplement Series*, 258, 41, doi: [10.3847/1538-4365/ac3914](https://doi.org/10.3847/1538-4365/ac3914)
- Bernardinelli, P. H., Bernstein, G. M., Jindal, N., et al. 2023, *The Astrophysical Journal Supplement Series*, 269, 18, doi: [10.3847/1538-4365/acf6bf](https://doi.org/10.3847/1538-4365/acf6bf)
- Bernstein, G. M., Trilling, D. E., Allen, R. L., et al. 2004, *The Astronomical Journal*, 128, 1364, doi: [10.1086/422919](https://doi.org/10.1086/422919)
- Betancourt, M. 2017, doi: [10.48550/arXiv.1701.02434](https://doi.org/10.48550/arXiv.1701.02434)
- Boerner, T. J., Deems, S., Furlani, T. R., Knuth, S. L., & Towns, J. 2023, in *Practice and Experience in Advanced Research Computing 2023: Computing for the Common Good*, PEARC '23 (New York, NY, USA: Association for Computing Machinery), 173–176, doi: [10.1145/3569951.3597559](https://doi.org/10.1145/3569951.3597559)
- Bolin, B. T., Fremling, C., Morbidelli, A., et al. 2023, *Monthly Notices of the Royal Astronomical Society: Letters*, 521, L29, doi: [10.1093/mnras/slad018](https://doi.org/10.1093/mnras/slad018)
- Bovy, J., Hogg, D. W., & Roweis, S. T. 2011, *The Annals of Applied Statistics*, 5, 1657, doi: [10.1214/10-AOAS439](https://doi.org/10.1214/10-AOAS439)
- Bradbury, J., Frostig, R., Hawkins, P., et al. 2018, *JAX: composable transformations of Python+NumPy programs*, 0.3.13. <http://github.com/google/jax>
- Brown, M. E. 2001, *The Astronomical Journal*, 121, 2804, doi: [10.1086/320391](https://doi.org/10.1086/320391)
- . 2012, *Annual Review of Earth and Planetary Sciences*, 40, 467, doi: [10.1146/annurev-earth-042711-105352](https://doi.org/10.1146/annurev-earth-042711-105352)
- Brubaker, M., Salzman, M., & Urtasun, R. 2012, in *Proceedings of Machine Learning Research*, Vol. 22, *Proceedings of the Fifteenth International Conference on Artificial Intelligence and Statistics*, ed. N. D. Lawrence & M. Girolami (La Palma, Canary Islands: PMLR), 161–172. <https://proceedings.mlr.press/v22/brubaker12.html>
- Buchanan, L. E., Schwamb, M. E., Fraser, W. C., et al. 2022, *The Planetary Science Journal*, 3, 9, doi: [10.3847/PSJ/ac42c9](https://doi.org/10.3847/PSJ/ac42c9)
- Chen, Y.-T., Gladman, B., Volk, K., et al. 2019, *AJ*, 158, 214, doi: [10.3847/1538-3881/ab480b](https://doi.org/10.3847/1538-3881/ab480b)
- Collyer, C., Pike, R., Alexandersen, M., et al. 2024, in *AAS/Division for Planetary Sciences Meeting Abstracts*, Vol. 56, *AAS/Division for Planetary Sciences Meeting Abstracts*, 211.08
- Crompvoets, B. L., Lawler, S. M., Volk, K., et al. 2022, *The Planetary Science Journal*, 3, 113, doi: [10.3847/PSJ/ac67e0](https://doi.org/10.3847/PSJ/ac67e0)
- Dalle Ore, C. M., Dalle Ore, L. V., Roush, T. L., et al. 2013, *Icarus*, 222, 307, doi: [10.1016/j.icarus.2012.11.015](https://doi.org/10.1016/j.icarus.2012.11.015)
- Dawson, R. I., & Murray-Clay, R. 2012, *The Astrophysical Journal*, 750, 43, doi: [10.1088/0004-637X/750/1/43](https://doi.org/10.1088/0004-637X/750/1/43)
- Dempster, A. P., Laird, N. M., & Rubin, D. B. 1977, *Journal of the Royal Statistical Society: Series B (Methodological)*, 39, 1, doi: [10.1111/j.2517-6161.1977.tb01600.x](https://doi.org/10.1111/j.2517-6161.1977.tb01600.x)
- Doressoundiram, A., Barucci, M. A., Romon, J., & Veillet, C. 2001, *Icarus*, 154, 277, doi: [10.1006/icar.2001.6724](https://doi.org/10.1006/icar.2001.6724)
- Figueiredo, M., & Jain, A. 2002, *IEEE Transactions on Pattern Analysis and Machine Intelligence*, 24, 381, doi: [10.1109/34.990138](https://doi.org/10.1109/34.990138)
- Fraser, W. C., & Brown, M. E. 2012, *Astrophysical Journal*, 749, 33, doi: [10.1088/0004-637X/749/1/33](https://doi.org/10.1088/0004-637X/749/1/33)

- Fraser, W. C., Brown, M. E., Morbidelli, A., Parker, A., & Batygin, K. 2014, *Astrophysical Journal*, 782, 100, doi: [10.1088/0004-637X/782/2/100](https://doi.org/10.1088/0004-637X/782/2/100)
- Fraser, W. C., Pike, R. E., Marsset, M., et al. 2023, *The Planetary Science Journal*, 4, 80, doi: [10.3847/PSJ/acc844](https://doi.org/10.3847/PSJ/acc844)
- Fulchignoni, M., Belskaya, I., Barucci, M. A., de Sanctis, M. C., & Doressoundiram, A. 2008, *Transneptunian Object Taxonomy*. <https://ui.adsabs.harvard.edu/abs/2008ssbn.book..181F>
- Gelman, A., Carlin, J., Stern, H., et al. 2013, *Bayesian Data Analysis, Third Edition*, Chapman & Hall/CRC Texts in Statistical Science (Taylor & Francis). <https://books.google.com/books?id=ZXL6AQAQAQBAJ>
- Gladman, B., Marsden, B. G., & Vanlaerhoven, C. 2008, *Nomenclature in the Outer Solar System*, ed. M. A. Barucci, H. Boehnhardt, D. P. Cruikshank, A. Morbidelli, & R. Dotson (University of Arizona Press), 43–57
- Gladman, B., & Volk, K. 2021, *Annual Review of Astronomy and Astrophysics*, 59, 203, doi: [10.1146/annurev-astro-120920-010005](https://doi.org/10.1146/annurev-astro-120920-010005)
- Gladman, B., Lawler, S. M., Petit, J. M., et al. 2012, *Astronomical Journal*, 144, 23, doi: [10.1088/0004-6256/144/1/23](https://doi.org/10.1088/0004-6256/144/1/23)
- Gomes, R. S. 2003, *Icarus*, 161, 404, doi: [10.1016/S0019-1035\(02\)00056-8](https://doi.org/10.1016/S0019-1035(02)00056-8)
- Huang, Y., Gladman, B., & Volk, K. 2022, *The Astrophysical Journal Supplement Series*, 259, 54, doi: [10.3847/1538-4365/ac559a](https://doi.org/10.3847/1538-4365/ac559a)
- Hunter, J. D. 2007, *Computing in Science & Engineering*, 9, 90, doi: [10.1109/MCSE.2007.55](https://doi.org/10.1109/MCSE.2007.55)
- Ikeda, Y. 2023, yuzie007/mpltern: 1.0.0, 1.0.0, Zenodo, doi: [10.5281/zenodo.8025024](https://doi.org/10.5281/zenodo.8025024)
- Ivezić, Ž., Kahn, S. M., Tyson, J. A., et al. 2019, *The Astrophysical Journal*, 873, 111, doi: [10.3847/1538-4357/ab042c](https://doi.org/10.3847/1538-4357/ab042c)
- Jeffreys, H. 1961, *Theory of Probability*, 3rd edn. (Oxford, UK: Oxford University Press)
- Jewitt, D. 2018, *The Astronomical Journal*, 155, 56, doi: [10.3847/1538-3881/aaa1a4](https://doi.org/10.3847/1538-3881/aaa1a4)
- Jewitt, D. C., & Luu, J. X. 2001, *The Astronomical Journal*, 122, 2099, doi: [10.1086/323304](https://doi.org/10.1086/323304)
- Jones, E., Oliphant, T., Peterson, P., et al. 2001–, *SciPy: Open source scientific tools for Python*. <http://www.scipy.org/>
- Kaib, N. A., & Sheppard, S. S. 2016, *The Astronomical Journal*, 152, 133, doi: [10.3847/0004-6256/152/5/133](https://doi.org/10.3847/0004-6256/152/5/133)
- Kavelaars, J. J., Petit, J.-M., Gladman, B., et al. 2021, *The Astrophysical Journal Letters*, 920, L28, doi: [10.3847/2041-8213/ac2c72](https://doi.org/10.3847/2041-8213/ac2c72)
- Khain, T., Becker, J. C., Lin, H. W., et al. 2020, *The Astronomical Journal*, 159, 133, doi: [10.3847/1538-3881/ab7002](https://doi.org/10.3847/1538-3881/ab7002)
- Lacerda, P., Fornasier, S., Lellouch, E., et al. 2014, *The Astrophysical Journal*, 793, L2, doi: [10.1088/2041-8205/793/1/L2](https://doi.org/10.1088/2041-8205/793/1/L2)
- Lam, S. K., Pitrou, A., & Seibert, S. 2015, in *Proceedings of the Second Workshop on the LLVM Compiler Infrastructure in HPC, LLVM '15* (New York, NY, USA: Association for Computing Machinery), doi: [10.1145/2833157.2833162](https://doi.org/10.1145/2833157.2833162)
- Lawler, S. M., Shankman, C., Kavelaars, J. J., et al. 2018, *The Astronomical Journal*, 155, 197, doi: [10.3847/1538-3881/aab8ff](https://doi.org/10.3847/1538-3881/aab8ff)
- Lawler, S. M., Pike, R. E., Kaib, N., et al. 2019, *The Astronomical Journal*, 157, 253, doi: [10.3847/1538-3881/ab1c4c](https://doi.org/10.3847/1538-3881/ab1c4c)
- Lewis, A. 2019, arXiv e-prints, arXiv:1910.13970, doi: [10.48550/arXiv.1910.13970](https://doi.org/10.48550/arXiv.1910.13970)
- Lewis, S. M., & Raftery, A. E. 1997, *Journal of the American Statistical Association*, 92, 648, doi: [10.2307/2965712](https://doi.org/10.2307/2965712)
- Lin, H. W., W. Gerdes, D., J. Hamilton, S., et al. 2019, *Icarus*, 321, 426, doi: [10.1016/j.icarus.2018.12.006](https://doi.org/10.1016/j.icarus.2018.12.006)
- Luu, J., & Jewitt, D. 1996, *The Astronomical Journal*, 112, 2310, doi: [10.1086/118184](https://doi.org/10.1086/118184)
- Lykawka, P. S., & Mukai, T. 2005, *Planet. Space Sci.*, 53, 1175, doi: [10.1016/j.pss.2004.12.015](https://doi.org/10.1016/j.pss.2004.12.015)
- Malhotra, R., & Roy, S. 2023, *Research Notes of the American Astronomical Society*, 7, 143, doi: [10.3847/2515-5172/ace4c3](https://doi.org/10.3847/2515-5172/ace4c3)
- Markwardt, L., Wen Lin, H., Gerdes, D., & Adams, F. C. 2023, *The Planetary Science Journal*, 4, 135, doi: [10.3847/PSJ/ace528](https://doi.org/10.3847/PSJ/ace528)
- Marsset, M., Fraser, W. C., Pike, R. E., et al. 2019, *The Astronomical Journal*, 157, 94, doi: [10.3847/1538-3881/aaf72e](https://doi.org/10.3847/1538-3881/aaf72e)
- Marsset, M., Fraser, W. C., Schwamb, M. E., et al. 2023, *The Planetary Science Journal*, 4, 160, doi: [10.3847/PSJ/ace7d0](https://doi.org/10.3847/PSJ/ace7d0)

- Matheson, I. C., Malhotra, R., & Keane, J. T. 2023, *Monthly Notices of the Royal Astronomical Society*, 522, 3298, doi: [10.1093/mnras/stad1208](https://doi.org/10.1093/mnras/stad1208)
- Melchior, P., & Goulding, A. D. 2018, *Astronomy and Computing*, 25, 183, doi: [10.1016/j.ascom.2018.09.013](https://doi.org/10.1016/j.ascom.2018.09.013)
- Meurer, A., Smith, C. P., Paprocki, M., et al. 2017, *PeerJ Computer Science*, 3, e103, doi: [10.7717/peerj-cs.103](https://doi.org/10.7717/peerj-cs.103)
- Minka, T. 2000, *Estimating a Dirichlet distribution*, Technical report, MIT
- Morbideilli, A., & Nesvorný, D. 2020, in *The Trans-Neptunian Solar System*, ed. D. Prialnik, M. A. Barucci, & L. Young, 25–59, doi: [10.1016/B978-0-12-816490-7.00002-3](https://doi.org/10.1016/B978-0-12-816490-7.00002-3)
- Müller, T., Lellouch, E., & Fornasier, S. 2020, in *The Trans-Neptunian Solar System*, ed. D. Prialnik, M. A. Barucci, & L. Young, 153–181, doi: [10.1016/B978-0-12-816490-7.00007-2](https://doi.org/10.1016/B978-0-12-816490-7.00007-2)
- Napier, K. J., & Adams, F. C. 2022, *Research Notes of the American Astronomical Society*, 6, 46, doi: [10.3847/2515-5172/ac5b6c](https://doi.org/10.3847/2515-5172/ac5b6c)
- Napier, K. J., Lin, H. W., Gerdes, D. W., et al. 2024, *The Planetary Science Journal*, 5, 50, doi: [10.3847/PSJ/ad1528](https://doi.org/10.3847/PSJ/ad1528)
- Neal, R. 2011, in *Handbook of Markov Chain Monte Carlo*, ed. S. Brooks, A. Gelman, G. Jones, & X.-L. Meng, Vol. 20116022 (Chapman and Hall/CRC), doi: [10.1201/b10905-6](https://doi.org/10.1201/b10905-6)
- Nesvorný, D. 2015a, *Astronomical Journal*, 150, 73, doi: [10.1088/0004-6256/150/3/73](https://doi.org/10.1088/0004-6256/150/3/73)
- . 2015b, *Astronomical Journal*, 150, 68, doi: [10.1088/0004-6256/150/3/68](https://doi.org/10.1088/0004-6256/150/3/68)
- Nesvorný, D., & Vokrouhlický, D. 2016, *The Astrophysical Journal*, 825, 94, doi: [10.3847/0004-637x/825/2/94](https://doi.org/10.3847/0004-637x/825/2/94)
- Nesvorný, D., Vokrouhlický, D., Alexandersen, M., et al. 2020, *The Astronomical Journal*, 160, 46, doi: [10.3847/1538-3881/ab98fb](https://doi.org/10.3847/1538-3881/ab98fb)
- Nielsen, S. F. 2000, *Bernoulli*, 6, 457, doi: [10.2307/3318671](https://doi.org/10.2307/3318671)
- Oliphant, T. E. 2015, *Guide to NumPy*, 2nd edn. (USA: CreateSpace Independent Publishing Platform)
- Peixinho, N., Delsanti, A., & Doressoundiram, A. 2015, *Astronomy and Astrophysics*, 577, A35, doi: [10.1051/0004-6361/201425436](https://doi.org/10.1051/0004-6361/201425436)
- Petit, J.-M., Gladman, B., Kavelaars, J. J., et al. 2023, *The Astrophysical Journal Letters*, 947, L4, doi: [10.3847/2041-8213/acc525](https://doi.org/10.3847/2041-8213/acc525)
- Petit, J. M., Kavelaars, J. J., Gladman, B. J., et al. 2011, *Astronomical Journal*, 142, doi: [10.1088/0004-6256/142/4/131](https://doi.org/10.1088/0004-6256/142/4/131)
- Pike, R. E., Fraser, W. C., Schwamb, M. E., et al. 2017, *The Astronomical Journal*, 154, 101, doi: [10.3847/1538-3881/aa83b1](https://doi.org/10.3847/1538-3881/aa83b1)
- Pike, R. E., Proudfoot, B. C., Ragozzine, D., et al. 2019, *Nature Astronomy*, doi: [10.1038/s41550-019-0867-z](https://doi.org/10.1038/s41550-019-0867-z)
- Pike, R. E., Fraser, W. C., Volk, K., et al. 2023, *The Planetary Science Journal*, 4, 200, doi: [10.3847/PSJ/ace2c2](https://doi.org/10.3847/PSJ/ace2c2)
- Press, W. 2007, *Numerical Recipes 3rd Edition: The Art of Scientific Computing*, Numerical Recipes: The Art of Scientific Computing (Cambridge University Press). <https://books.google.com/books?id=1aAOdzK3FegC>
- Proudfoot, B., & Ragozzine, D. 2024, personal communication
- Proudfoot, B. C. N., Fernández-Valenzuela, E., Stansberry, J. A., et al. 2024, *The Astronomical Journal*, 168, 269, doi: [10.3847/1538-3881/ad864e](https://doi.org/10.3847/1538-3881/ad864e)
- Proudfoot, B. C. N., & Ragozzine, D. 2019, *The Astronomical Journal*, 157, 230, doi: [10.3847/1538-3881/ab19c4](https://doi.org/10.3847/1538-3881/ab19c4)
- Pérez, F., & Granger, B. E. 2007, *Computing in Science & Engineering*, 9, 21, doi: [10.1109/MCSE.2007.53](https://doi.org/10.1109/MCSE.2007.53)
- Ragozzine, D., & Brown, M. E. 2007, *The Astronomical Journal*, 134, 2160, doi: [10.1086/522334](https://doi.org/10.1086/522334)
- Rein, H., & Liu, S.-F. 2012, *Astronomy & Astrophysics*, 537, A128, doi: [10.1051/0004-6361/201118085](https://doi.org/10.1051/0004-6361/201118085)
- Rein, H., & Tamayo, D. 2015, *Monthly Notices of the Royal Astronomical Society*, 452, 376, doi: [10.1093/mnras/stv1257](https://doi.org/10.1093/mnras/stv1257)
- Rubin, D. B. 1976, *Biometrika*, 63, 581, doi: [10.1093/biomet/63.3.581](https://doi.org/10.1093/biomet/63.3.581)
- Russell, H. N. 1916, *ApJ*, 43, 173, doi: [10.1086/142244](https://doi.org/10.1086/142244)
- Schwamb, M. E., Fraser, W. C., Bannister, M. T., et al. 2019, *The Astrophysical Journal Supplement Series*, 243, 12, doi: [10.3847/1538-4365/ab2194](https://doi.org/10.3847/1538-4365/ab2194)

- Showalter, M. R., Benecchi, S. D., Buie, M. W., et al. 2021, *Icarus*, 356, 114098, doi: [10.1016/j.icarus.2020.114098](https://doi.org/10.1016/j.icarus.2020.114098)
- Song, X. C., Smith, P., Kalyanam, R., et al. 2022, in *Practice and Experience in Advanced Research Computing 2022: Revolutionary: Computing, Connections, You*, PEARC '22 (New York, NY, USA: Association for Computing Machinery), doi: [10.1145/3491418.3530766](https://doi.org/10.1145/3491418.3530766)
- Stern, S. A., Bagenal, F., Ennico, K., et al. 2015, *Science*, 350, aad1815, doi: [10.1126/science.aad1815](https://doi.org/10.1126/science.aad1815)
- Stern, S. A., Weaver, H. A., Spencer, J. R., et al. 2019, *Science*, 364, doi: [10.1126/science.aaw9771](https://doi.org/10.1126/science.aaw9771)
- Tegler, S. C., & Romanishin, W. 1998, *Nature*, 392, 49, doi: [10.1038/32108](https://doi.org/10.1038/32108)
- . 2000, *Nature*, 407, 979, doi: [10.1038/35039572](https://doi.org/10.1038/35039572)
- Tegler, S. C., Romanishin, W., & G. J. Consolmagno, S. J. 2016, *The Astronomical Journal*, 152, 210, doi: [10.3847/0004-6256/152/6/210](https://doi.org/10.3847/0004-6256/152/6/210)
- Trilling, D. E., Gerdes, D. W., Jurić, M., et al. 2024, *The Astronomical Journal*, 167, 132, doi: [10.3847/1538-3881/ad1529](https://doi.org/10.3847/1538-3881/ad1529)
- Trujillo, C. A., & Brown, M. E. 2002, *The Astrophysical Journal*, 566, L125, doi: [10.1086/339437](https://doi.org/10.1086/339437)
- Van Laerhoven, C., Gladman, B., Volk, K., et al. 2019, *The Astronomical Journal*, 158, 49, doi: [10.3847/1538-3881/ab24e1](https://doi.org/10.3847/1538-3881/ab24e1)
- Volk, K., & Malhotra, R. 2019, *The Astronomical Journal*, 158, 64, doi: [10.3847/1538-3881/ab2639](https://doi.org/10.3847/1538-3881/ab2639)
- Volk, K., Murray-Clay, R., Gladman, B., et al. 2016, *The Astronomical Journal*, 152, 23, doi: [10.3847/0004-6256/152/1/23](https://doi.org/10.3847/0004-6256/152/1/23)
- Willmer, C. N. A. 2018, doi: [10.3847/1538-4365/aabfdf](https://doi.org/10.3847/1538-4365/aabfdf)
- Wong, I., & Brown, M. E. 2017, *The Astronomical Journal*, 153, 145, doi: [10.3847/1538-3881/aa60c3](https://doi.org/10.3847/1538-3881/aa60c3)
- Wu, C. F. J. 1983, *The Annals of Statistics*, 11, 95. <http://www.jstor.org/stable/2240463>
- Youdin, A. N., & Goodman, J. 2005, *The Astrophysical Journal*, 620, 459, doi: [10.1086/426895](https://doi.org/10.1086/426895)

APPENDIX

A. ESTIMATING DISTRIBUTIONS WITH GAUSSIAN MIXTURE MODELS

A.1. *Gaussian mixture model review*

We wish to determine the optimal underlying color distribution implied by our TNO sample. To this end, we will posit that the underlying distribution for the colors \mathbf{c} is a mixture model given by a combination of K components. For a general measurement \mathbf{x} in d dimensions, we have that the mixture model is

$$p(\mathbf{x}|\boldsymbol{\theta}) = \sum_{\alpha=1}^K f_{\alpha} p(\mathbf{x}|\boldsymbol{\theta}_{\alpha}), \quad (\text{A1})$$

where the α^{th} component is described by a probability distribution $p(\mathbf{x}|\boldsymbol{\theta}_{\alpha})$, and the parameters $\boldsymbol{\theta} = \bigcup_{\alpha} \{\boldsymbol{\theta}_{\alpha}, f_{\alpha}\}$ are subject to the constraint $\sum_{\alpha} f_{\alpha} = 1$ to ensure that $p(\mathbf{x}|\boldsymbol{\theta})$ is normalized. In a Gaussian mixture model (GMM), the probability distribution $p(\mathbf{x}|\boldsymbol{\theta}_{\alpha})$ is a multivariate Gaussian with mean $\boldsymbol{\mu}_{\alpha}$ and covariance matrix $\boldsymbol{\Sigma}_{\alpha}$, that is,

$$p(\mathbf{x}|\boldsymbol{\theta}_{\alpha}) = \mathcal{N}(\mathbf{x}|\boldsymbol{\mu}_{\alpha}, \boldsymbol{\Sigma}_{\alpha}) \equiv \frac{1}{\sqrt{(2\pi)^d \det(\boldsymbol{\Sigma}_{\alpha})}} \exp \left[-\frac{1}{2} (\mathbf{x} - \boldsymbol{\mu}_{\alpha})^{\top} \boldsymbol{\Sigma}_{\alpha}^{-1} (\mathbf{x} - \boldsymbol{\mu}_{\alpha}) \right]. \quad (\text{A2})$$

We define the likelihood of the N data points $\mathcal{X} \equiv \bigcup_{i=1}^N \{\mathbf{x}_i\}$ as

$$\mathcal{L}(\mathcal{X}|\boldsymbol{\theta}) \equiv \prod_{i=1}^N \sum_{\alpha=1}^K f_{\alpha} p(\mathbf{x}_i|\boldsymbol{\theta}_{\alpha}). \quad (\text{A3})$$

This is an *uncategorized* likelihood, as we do not have the information of which component k is the parent for sample i . We define the indicator $\mathcal{Z} = \bigcup_i \{\mathbf{z}^{(i)}\}$, such that the α^{th} entry of $\mathbf{z}^{(i)}$ is $z_{\alpha}^{(i)} = 1$ if i was generated by component α , and 0 otherwise. We define the likelihood of the complete data $\mathcal{D} = \{\mathcal{X}, \mathcal{Z}\}$ as

$$\mathcal{L}(\mathcal{D}|\boldsymbol{\theta}) \equiv \prod_{i=1}^N \sum_{\alpha=1}^K [f_{\alpha} p(\mathbf{x}_i|\boldsymbol{\theta}_{\alpha}) p(z_{\alpha}^{(i)}|\mathbf{x}_i, \boldsymbol{\theta}_{\alpha})]^{z_{\alpha}^{(i)}}. \quad (\text{A4})$$

From Bayes' theorem,

$$q_{i\alpha} \equiv p(z_{\alpha}^{(i)}|\mathbf{x}_i, \boldsymbol{\theta}_{\alpha}) = \frac{p(\mathbf{x}_i|z_{\alpha}^{(i)}, \boldsymbol{\theta}_{\alpha}) p(z_{\alpha}^{(i)})}{\sum_{\beta} p(\mathbf{x}_i|z_{\beta}^{(i)}, \boldsymbol{\theta}_{\beta}) p(z_{\beta}^{(i)})}. \quad (\text{A5})$$

We set $p(z_{\alpha}^{(i)}) \propto 1$, that is, all components are equally likely.

The expectation-maximization (EM) algorithm for GMMs works by alternating the expectation (E) step by computing Equation A5 and using its value to update the model parameters by taking

weighted moments of \mathbf{x} :

$$f_\alpha = \frac{1}{N} \sum_i q_{i\alpha} \quad (\text{A6a})$$

$$\boldsymbol{\mu}_\alpha = \frac{1}{\sum_i q_{i\alpha}} \sum_i q_{i\alpha} \mathbf{x}_i \quad (\text{A6b})$$

$$\boldsymbol{\Sigma}_\alpha = \frac{1}{\sum_i q_{i\alpha}} \sum_i q_{i\alpha} (\mathbf{x}_i - \boldsymbol{\mu}_\alpha)(\mathbf{x}_i - \boldsymbol{\mu}_\alpha)^\top \quad (\text{A6c})$$

These steps, applied successfully, converge to a local maximum of $\mathcal{L}(\mathcal{D}|\boldsymbol{\theta})$ (Dempster et al. 1977; Wu 1983).

The standard GMM framework requires that the number of components K is known (or posited) a priori - something that we do not necessarily have in our case. The final values for $\boldsymbol{\mu}_\alpha$ are also dependent on the initialization algorithm, as the EM steps can converge to a local, but not necessarily global, maximum of the likelihood. We will modify the likelihood in Equation A3 to account for the unknown K , as well as make the algorithm more robust to the initial values and incorporate the generalizations by Bovy et al. (2011); Melchior & Goulding (2018) to account for measurement errors and selection effects.

A.2. Unsupervised Gaussian mixture model with noisy and incomplete data

Figueiredo & Jain (2002) proposed a modification of the general mixture model framework so that the number of components K does not need to be defined a priori. Rather, a range $K \in [K_{\min}, K_{\max}]$ is specified, and the modified E and M steps are such that components whose amplitudes α_k become too small are annihilated. Their algorithm is also more robust to the initialization as, by starting with a number of components $K_{\max} \gg K_{\text{true}}$, these are more likely to cover the entire parameter space, and redundant components compete with each other until all but one are annihilated. This means that the number of components K is a free parameter in the model, and the optimal number is found in an unsupervised manner.

Here, we combine the Figueiredo & Jain (2002) approach with the extreme de-convolution of Bovy et al. (2011) and its modifications for missing data by Melchior & Goulding (2018). We do not know, for any given sample i , the true value \mathbf{x}_i . What is known is the measured value $\mathbf{y}_i = \mathbf{x}_i + \mathbf{e}_i$, where \mathbf{e}_i is a (Gaussian) noise drawn from $\mathcal{N}(\mathbf{e}_i|\mathbf{0}, \mathbf{S}_i)$, where \mathbf{S}_i is the covariance matrix of the measurement. Following Bovy et al. (2011), we write the likelihood of \mathbf{y}_i by marginalizing over \mathbf{x}_i ,

$$p(\mathbf{y}_i|\mathbf{S}_i, \boldsymbol{\theta}) = \sum_\alpha f_\alpha \int d\mathbf{x}_i \mathcal{N}(\mathbf{y}_i|\mathbf{x}_i, \mathbf{S}_i) \mathcal{N}(\mathbf{x}_i|\boldsymbol{\mu}_\alpha, \boldsymbol{\Sigma}_\alpha) = \sum_\alpha f_\alpha \mathcal{N}(\mathbf{y}_i|\boldsymbol{\mu}_\alpha, \boldsymbol{\Sigma}_\alpha + \mathbf{S}_i). \quad (\text{A7})$$

We can modify our likelihood (Equation A3) for the noisy data $\mathcal{Y} = \bigcup_i \{\mathbf{y}_i, \mathbf{S}_i\}$ and also penalize it due to a selection process $p(\mathcal{S}|\mathbf{x})$

$$\mathcal{L}(\mathcal{Y}|\boldsymbol{\theta}) = \frac{\prod_i \sum_\alpha f_\alpha \mathcal{N}(\mathbf{y}_i|\boldsymbol{\mu}_\alpha, \boldsymbol{\Sigma}_\alpha + \mathbf{S}_i)}{[\int d\mathbf{x}' p(\mathbf{x}'|\boldsymbol{\theta}) p(\mathcal{S}|\mathbf{x}')]^N}. \quad (\text{A8})$$

Note that, implicitly, we are assuming that the data is “missing at random” (Rubin 1976), that is, $p(\mathcal{S}|\mathbf{x})$ is independent of $p(\mathbf{x}|\boldsymbol{\theta})$, so the likelihood is also independent of the missing data. The

corrections in the GMM due to missing samples are found by a rejection sampling procedure between the EM steps. We draw N' samples \mathbf{x}'_i from the current model, apply noise to these samples so that $\mathbf{y}'_i = \mathbf{x}'_i + \mathbf{e}'_i$, where \mathbf{e}'_i is obtained by sampling a Gaussian distribution with a covariance matrix \mathbf{S}'_i drawn from the distribution of $\{\mathbf{S}_i\}$ and applying the selection function: a given sample i is rejected if $p(\mathcal{S}|\mathbf{y}'_i) \leq u$, where $u \sim \text{Unif}(0, 1)$. This process is repeated until the number of accepted samples N'_{acc} is consistent with the 68% limits of a Poisson distribution given by N (Melchior & Goulding 2018). We define the subset of the rejected data with N'_{rej} samples as $\mathcal{M} = \bigcup_{i=1}^{N'_{\text{rej}}} \{\mathbf{y}'_i, \mathbf{S}'_i\}$.

Finally, we need to account for the unknown number of mixture components K . To do so, we apply the improper Dirichlet prior for the amplitudes $\{f_\alpha\}$ from Figueiredo & Jain (2002),

$$p(\{f_\alpha\}) = N^{-K(N_{\text{par}}+1)/2} \exp \left[-\frac{N_{\text{par}}}{2} \sum_{\alpha, f_\alpha > 0} \log f_\alpha \right], \quad (\text{A9})$$

where N_{par} is the number of free parameters in each component α . For a Gaussian mixture, $N_{\text{par}} = d + d(d+1)/2$. The inclusion of this prior translates to a modification in the amplitude calculation in the M step, so that the amplitudes $\{f_\alpha\}$ are penalized by the number of parameters each component needs to estimate, which allows for a component to have $f_\alpha = 0$ and, if this happens, the component is discarded by the algorithm. We refer the reader to Figueiredo & Jain (2002) for a full derivation of the procedure.

We now can write the full EM algorithm for this unsupervised mixture model. The expectation step is as in Melchior & Goulding (2018):

$$q_{i\alpha} = \frac{f_\alpha \mathcal{N}(\mathbf{y}_i | \boldsymbol{\mu}_\alpha, \boldsymbol{\Sigma}_\alpha + \mathbf{S}_i)}{\sum_\beta f_\beta \mathcal{N}(\mathbf{y}_i | \boldsymbol{\mu}_\beta, \boldsymbol{\Sigma}_\beta + \mathbf{S}_i)}, \quad (\text{A10a})$$

$$\mathbf{b}_{i\alpha} = \boldsymbol{\mu}_\alpha + \boldsymbol{\Sigma}_\alpha (\boldsymbol{\Sigma}_\alpha + \mathbf{S}_i)^{-1} (\mathbf{y}_i - \boldsymbol{\mu}_\alpha), \quad (\text{A10b})$$

$$\mathbf{B}_{i\alpha} = \boldsymbol{\Sigma}_\alpha - \boldsymbol{\Sigma}_\alpha (\boldsymbol{\Sigma}_\alpha + \mathbf{S}_i)^{-1} \boldsymbol{\Sigma}_\alpha. \quad (\text{A10c})$$

The two additional parameters, $\mathbf{b}_{i\alpha}$ and $\mathbf{B}_{i\alpha}$, are, respectively, the conditional estimates of \mathbf{y}_i and \mathbf{S}_i , given each component α (Bovy et al. 2011). An important detail here is that this is computed $\forall i \in \{\mathcal{Y}, \mathcal{M}\}$, that is, this is computed both for the observed data \mathcal{Y} and the realizations of the missing data \mathcal{M} . If there is no selection effect being considered, only the measurements in set \mathcal{Y} are required.

The maximization step includes the corrections for the noisy data as well as the prior in Equation A9:

$$f_\alpha = \frac{\max \left(0, \sum_{i \in \{\mathcal{Y}, \mathcal{M}\}} q_{i\alpha} - \frac{N_{\text{par}}}{2} \right)}{\sum_\beta \max \left(0, \sum_{i \in \{\mathcal{Y}, \mathcal{M}\}} q_{i\beta} - \frac{N_{\text{par}}}{2} \right)}, \quad (\text{A11a})$$

$$\boldsymbol{\mu}_\alpha = \frac{1}{\sum_{i \in \{\mathcal{Y}, \mathcal{M}\}} q_{i\alpha}} \sum_{i \in \{\mathcal{Y}, \mathcal{M}\}} q_{i\alpha} \mathbf{b}_{i\alpha}, \quad (\text{A11b})$$

$$\boldsymbol{\Sigma}_\alpha = \frac{1}{\sum_{i \in \{\mathcal{Y}, \mathcal{M}\}} q_{i\alpha}} \sum_{i \in \{\mathcal{Y}, \mathcal{M}\}} [q_{i\alpha} (\mathbf{b}_{i\alpha} - \boldsymbol{\mu}_\alpha) (\mathbf{b}_{i\alpha} - \boldsymbol{\mu}_\alpha)^\top + \mathbf{B}_{i\alpha}]. \quad (\text{A11c})$$

If a component is annihilated (that is, $f_\alpha = 0$), the E-step is recomputed so that its probability mass is redistributed for the other components. The procedure is repeated until $K = K_{\min}$. There is the possibility that, for a given K , no component is annihilated and the likelihood converges to a (potentially local) maximum. If that happens, the component with the smallest f_α is discarded, so that the entire range of K can be explored. The optimal model, as expected, maximizes $p(\{f_\alpha\})\mathcal{L}(\mathcal{Y}|\boldsymbol{\theta})$, which properly penalizes the likelihood with respect to number of components. The inclusion of the missing samples \mathcal{M} means that the converge is stochastic (Nielsen 2000), and either more computational steps or oversampling of the missing data \mathcal{M} are required to ensure convergence.

This software is available for open use at https://github.com/berardinelli/gmm_anyk.

B. THE BAYESIAN EVIDENCE RATIO

New appendix

Given two competing hypotheses \mathcal{H}_1 and \mathcal{H}_2 to explain observational data D , the (log) Bayesian evidence ratio is defined as

$$\mathcal{R} = \log \frac{p(D|\mathcal{H}_2)}{p(D|\mathcal{H}_1)} = \log \frac{\int d\mathbf{q}_1 \mathcal{L}(D|\mathbf{q}_1)p(\mathbf{q}_1)}{\int d\mathbf{q}_2 \mathcal{L}(D|\mathbf{q}_2)p(\mathbf{q}_2)}, \quad (\text{B12})$$

where $\mathbf{q}_{1,2}$ are the free parameters of the two competing hypotheses for the likelihood \mathcal{L} of obtaining data D , and $p(\mathbf{q}_{1,2})$ are priors on these parameters. In our typical application, our two hypotheses are that (1) each dynamical subset d has a distinct set of parameters \mathbf{q}_d to generate its data D_d , vs (2) all subsets share a common set of parameters \mathbf{q} for the distribution of physical parameters. In each case, the fractions f of mixtures are free to vary over the simplex to best fit the data. The evidence ratio is in this case

$$\mathcal{R} = \log \frac{\prod_d \int d\mathbf{q}_d p(\mathbf{q}_d)p(\mathbf{q}_d|D_d)}{\int d\mathbf{q} p(\mathbf{q}) \prod_d p(\mathbf{q}|D_d)}. \quad (\text{B13})$$

where

$$p(\mathbf{q}|D) \equiv \int df \mathcal{L}(\{\mathbf{q}, f\}|D) \quad (\text{B14})$$

is the likelihood of the parameters of interest after marginalizing over the other parameters of the overall model, including the occupation fractions.

In order to avoid performing the integrals in Equation B13 over the high-dimensional parameter spaces directly, we can use our HMC outputs to approximate this integral. We use the Laplace-Metropolis estimator of Lewis & Raftery (1997). We have that

$$p(D|\mathcal{H}) = \int d\mathbf{q} p(\mathbf{q})\mathcal{L}(\mathbf{q}|D) \approx (2\pi)^{P/2} |\mathbf{H}^*|^{1/2} p(\mathbf{q}^*)\mathcal{L}(\mathbf{q}^*|D). \quad (\text{B15})$$

Here, P is the number of parameters, \mathbf{q}^* is the value that maximizes $p(\mathbf{q})\mathcal{L}(\mathbf{q}|D)$, and \mathbf{H}^* is the inverse Hessian of this function evaluated at \mathbf{q}^* . In practice, these can be estimated by the mean and covariance of the HMC samples, respectively. Note that, while the HMC procedure also produces estimates for the f_β , these, by construction, cannot be used by the Laplace-Metropolis estimator: the simplex constraint imposes a Dirichlet prior on these variables, and Dirichlet-distributed variables have singular covariance matrices. To avoid this issue, we compute the integral over the f_β directly, using the fixed \mathbf{q}^* . This procedure is justified, as it is equivalent to changing the order of integration among two sets of variables.

C. HAMILTONIAN MONTE CARLO

We present here a simple introduction to the Hamiltonian Monte Carlo (HMC) algorithm—we refer the reader to [Neal \(2011\)](#), [Gelman et al. \(2013\)](#) and [Betancourt \(2017\)](#) for more complete presentations of this technique. As a variant of Markov Chain Monte Carlo, the goal of HMC is to produce samples \mathbf{q}_i from some probability distribution $p(\mathbf{q})$. In our case the parameters \mathbf{q} include both the population fractions f_β and any of the parameters $\theta, \theta', \bar{A}, s$ of our physical distributions. The probability distribution is the product of the likelihood in Equation 18 multiplied by any priors assigned to the parameters.

Following classical mechanics, we assume a Hamiltonian physical system with canonical positions \mathbf{q} and momenta \mathbf{p} . We define the kinetic energy of the system as $K(\mathbf{p})$ and the potential energy as $U(\mathbf{q})$. The Hamiltonian, a quantity analogous to the total energy of the system, is

$$\mathcal{H}(\mathbf{q}, \mathbf{p}) = K(\mathbf{p}) + U(\mathbf{q}). \quad (\text{C16})$$

For a HMC system, the target parameters are the canonical positions, and we assign the potential energy to be the log of the target probability:

$$U(\mathbf{q}) = -\log [p(\mathbf{q})\mathcal{L}(\mathbf{q})]. \quad (\text{C17})$$

We posit a kinetic energy term that is quadratic in the canonical momenta, with some chosen mass matrix \mathbf{M} :

$$K(\mathbf{p}) = \frac{1}{2}\mathbf{p}^\top \mathbf{M}^{-1}\mathbf{p}. \quad (\text{C18})$$

The key to HMC is to sample from a joint distribution $p(\mathbf{p}, \mathbf{q}) = \exp(-\mathcal{H})$. The first step of the HMC is simply the generation of new momenta \mathbf{p} from the conditional distribution $\sim p(\mathbf{p}|\mathbf{q})$; with the quadratic kinetic energy, this is a draw from a multivariate Gaussian, which is fast and exact. The second step updates the positions and the momenta by using the (Hamiltonian) dynamics of the system, following the standard equations of motion

$$\frac{d\mathbf{q}}{dt} = \frac{\partial \mathcal{H}}{\partial \mathbf{p}}; \quad \frac{d\mathbf{p}}{dt} = -\frac{\partial \mathcal{H}}{\partial \mathbf{q}}. \quad (\text{C19})$$

For a perfect numerical integrator, \mathcal{H} and hence $p(\mathbf{p}, \mathbf{q})$ are conserved during this integration, and integration over some time period t leads to a new sample of $(\mathbf{p}^*, \mathbf{q}^*)$ for the HMC chain. A numerical integration is necessarily inexact, and we retain or discard this sample using the Metropolis-Hastings probability of acceptance

$$\min [1, \exp(-\mathcal{H}(\mathbf{q}^*, \mathbf{p}^*) + \mathcal{H}(\mathbf{q}, \mathbf{p}))]. \quad (\text{C20})$$

The main implementation challenge in HMC is in the calculation of the gradient of the log likelihood with respect to the model parameters, so that the equations of motion can be integrated. Despite this complexity compared to simpler Metropolis-Hastings samplers, the addition of the Hamiltonian structure to the problem increases the chance of an accepted state during sampling in a high-dimensional space.

The only complication in the application to our problem is implementation of the system of constraints on the fractional parameters f_β , which must each be ≥ 0 and must satisfy $\sum f_\beta = 1$. The former constraint can be automatically satisfied by a change of variable from f_β to $q_\beta \equiv \log f_\beta$.

The simplex constraint is implemented by using the **RATTLE** algorithm for numerical integration of a constrained Hamiltonian system, as described by [Brubaker et al. \(2012\)](#). All of the derivatives of our likelihood, priors, and constraints are straightforward, and in fact amenable to the use of the automatic differentiation package **jax** ([Bradbury et al. 2018](#)).

D. COMPLETENESS ESTIMATES

To calculate the terms S_β in the likelihood in Equation 18 for the DES data given a population model, we need to execute the integrals over the selection probability $p(\mathcal{S}|\mathbf{c}, H, A, \mathbf{P})$ given in Equation 13c. Object discovery in *DES* uses detections on images taken in the *griz* bands ([Bernardinelli et al. 2020a, 2022](#)), and each dynamical class has its own observational biases, dominated, primarily, by a , q and I : larger- a objects can only be discovered when they are near perihelion (see, *e.g.* [Bernardinelli et al. 2020b](#), for a thorough discussion); objects at higher perihelia can only be detected with brighter H ; and populations with a higher density of high-inclination objects also have a larger area of the sky where objects can be discovered, which inherently changes their discoverability due to the large high ecliptic latitude coverage of the *DES* footprint.

The value of $p(\mathcal{S}|\mathbf{c}, H, A, \mathbf{P})$ for any specified values of the conditional variables can be estimated using the *DES* survey simulator². To conduct the specified integration of this, we need to posit a model for the distribution $p_\beta(\mathbf{c}, H, A, \mathbf{P})$ across the dynamical class under study. Our hypotheses provide models the distributions of \mathbf{c} , H_r , and A , but do not provide the full distribution of a dynamical class over orbital parameters. As a proxy model, we assume that the true distribution of non-resonant dynamical classes has azimuthal and temporal symmetry, *i.e.* the distributions over orbital parameters Ω and \mathcal{M} are uniform between 0 and 2π . We make the further assumption that argument of perihelion ω is uniform:

$$p(\Omega, \omega, \mathcal{M}) = u(\Omega)u(\omega)u(\mathcal{M}), \quad (\text{D21})$$

where u is uniform between 0 and 2π . Our choice of I and H_r distributions are described below, and depend on whether we are modeling the underlying distributions of I and H_r , or not. This leaves the a and e distribution of the true population unspecified. We will approximate this as the sum of a series of δ functions such that the dynamical distribution of our *observed* population would be exactly reproduced after applying the survey selection function, namely:

$$p(a, e, I, \Omega, \omega, \mathcal{M}, H_r, \mathbf{c}) = \sum_j \frac{\delta(a - a_j)\delta(e - e_j)}{p(\mathcal{S}|a_j, e_j, I, H_r, \mathbf{c})} p(\Omega, \omega, \mathcal{M}), \quad (\text{D22})$$

$$p(\mathcal{S}|a_j, e_j, I, H_r, \mathbf{c}) \equiv \int dI d\Omega d\omega d\mathcal{M} p(\mathcal{S}|a_j, e_j, I, \Omega, \omega, \mathcal{M}, H_r, \mathbf{c}) p(\Omega, \omega, \mathcal{M}). \quad (\text{D23})$$

In essence we bootstrap the observed population into a full population (for the purposes of conducting the integral in Equation 13c) but weighting each TNO orbit by the inverse of its selection rate for a chosen I , H_r , and color. When using the simulator to calculate each selection probability in Equation D23, we can give the simulated object a light curve amplitude A if desired.

For a resonant object in mean motion resonance $p:q$, we also need to find the subset of angles $\{\Omega, \omega, \mathcal{M}\}_{p:q} \subset [0, 2\pi)^3$ that produce a librating angle. To do so, we follow the procedure outlined in

² DESTNOSIM, <https://github.com/bernardinelli/DESTNOSIM>

Bernardinelli et al. (2022) to derive dynamical classifications for our real objects: we integrate the orbits of each synthetic object for 10 Myr and determine the fraction of time that the resonant angle

$$\sigma = p(\mathcal{M} + \omega + \Omega) - q(\mathcal{M}_N + \omega_N + \Omega_N) + (q - p)(\Omega + \omega) \quad (\text{D24})$$

librates. If the object librates for more than 50% of the time, we include it in the resonant subset; this is consistent with the criterion for a “resonant candidate” object in Bernardinelli et al. (2022). The subscript N refers to the relevant angles for Neptune. To reduce the computation complexity of the problem, only Neptune is treated as an active particle in the simulation.

Finally, we treat the inclinations I and absolute magnitudes H_r in three different ways, depending on the necessity of the model being evaluated:

- For the color distribution analysis of Section 2, we have that $p(I)p(H_r) \propto \sum_j \delta(H_r - H_{r,j})\delta(I - I_j)$;
- For the absolute magnitude distribution analysis, we maintain the inclination distribution as a δ function, but have a $p(H_r)$ uniform in the $3 \leq H_r \leq 10$ range;
- When simultaneously modelling the H_r and I distributions, we also consider an inclination distribution sinusoidally distributed in the $0^\circ \leq I \leq 90^\circ$ range. This choice leads to fewer clones at inclinations $I \geq 60^\circ$, where the *DES* distribution is approximately constant at a fixed magnitude (see Figure 5 of Bernardinelli et al. 2022) and no objects were discovered.

In the last case, we expect that the marginalized distribution $p(\mathcal{S}|I, H_r = 3)$ will represent the fraction of the area of the sky available to each population that is covered by the *DES* footprint at inclination I . In total, the estimates for this completeness functions required over 2 billion synthetic TNOs. We illustrate our completeness in Figure 14.

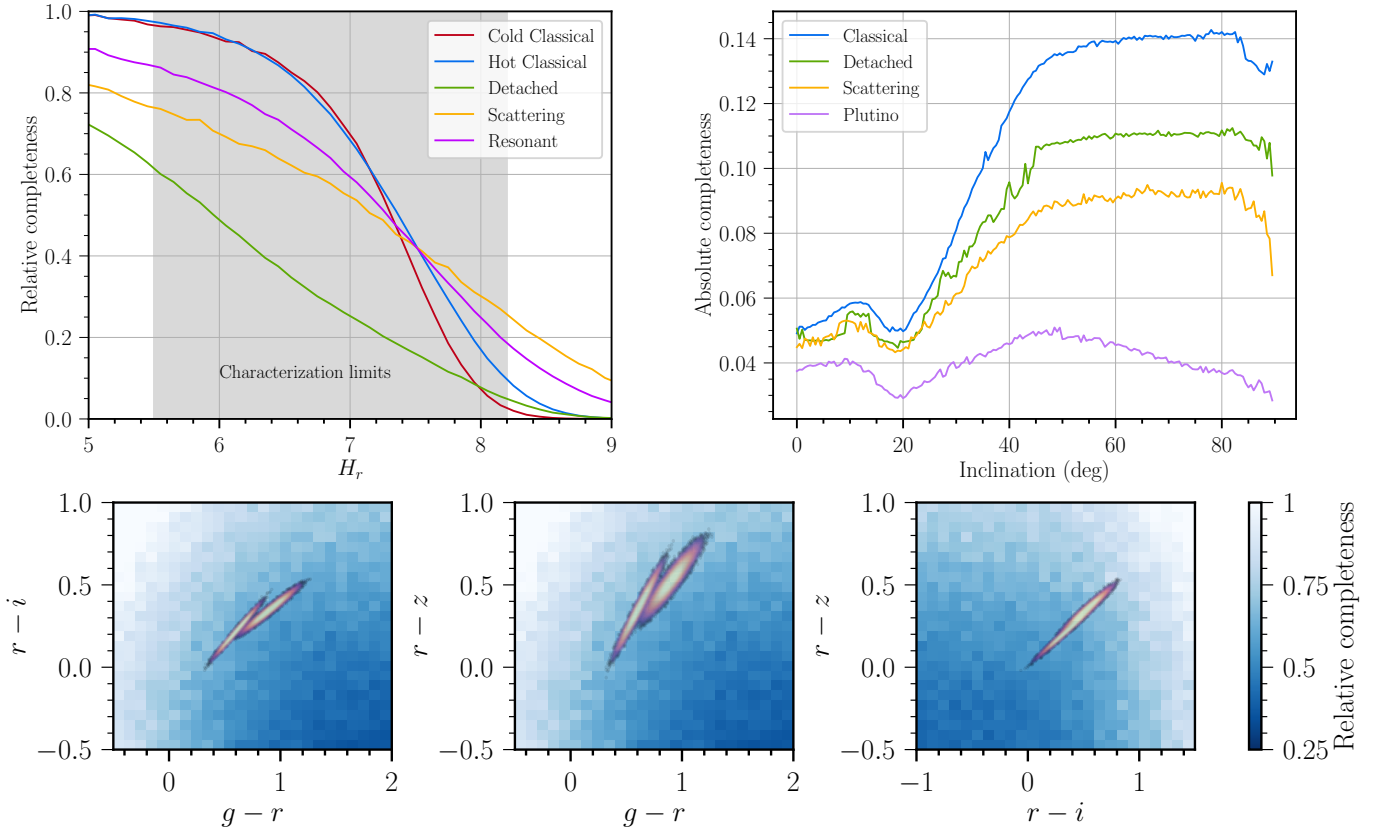


Figure 14. Completeness as a function of H_r (top left), inclination (top right) and the three color pairs (bottom) after marginalizing over the other relevant parameters. While the color and H_r figures show a relative completeness, so that the maximum value of the selection function is 1, the inclination completeness represents an absolute number that is indicative of the size of the *DES* footprint: *DES* covered $\approx 12\%$ of the sky, while the larger relative completeness accounts for object drifting into the survey footprint over the six years of the survey. The H_r and inclination completeness are subdivided as a function of orbital class and, for simplicity, we only show the Plutino case for the inclination distribution. In the color completeness panel, we also show the resulting color model as in Figure 1.

All Authors and Affiliations

PEDRO H. BERNARDINELLI ^{1,*} GARY M. BERNSTEIN ² T. M. C. ABBOTT³ M. AGUENA,⁴
S. S. ALLAM ⁵ D. BROOKS ⁶ A. CARNERO ROSELL ^{7,4,8} J. CARRETERO ⁹
L. N. DA COSTA,⁴ M. E. S. PEREIRA,¹⁰ T. M. DAVIS ¹¹ J. DE VICENTE ¹² S. DESAI ¹³
H. T. DIEHL ⁵ P. DOEL,⁶ S. EVERETT,¹⁴ B. FLAUGHER ⁵ J. FRIEMAN ^{5,15}
J. GARCÍA-BELLIDO ¹⁶ E. GAZTANAGA ^{17,18,19} R. A. GRUENDL,^{20,21} G. GUTIERREZ ⁵
K. HERNER ⁵ S. R. HINTON,¹¹ D. L. HOLLOWOOD,²² K. HONSCHIED ^{23,24}
D. J. JAMES ²⁵ K. KUEHN ^{26,27} O. LAHAV ⁶ S. LEE,²⁸ J. L. MARSHALL ²⁹
J. MENA-FERNÁNDEZ ³⁰ R. MIQUEL ^{31,9} J. MYLES,³² A. A. PLAZAS MALAGÓN ^{33,34}
S. SAMUROFF,^{35,9} E. SANCHEZ ¹² B. SANTIAGO,^{36,4} I. SEVILLA-NOARBE ¹² M. SMITH ³⁷
E. SUCHYTA ³⁸ G. TARLE ³⁹ D. L. TUCKER ⁵ V. VIKRAM,⁴⁰ A. R. WALKER ³
AND N. WEAVERDYCK^{41,42}

(THE *DES* COLLABORATION)

¹*DiRAC Institute, Department of Astronomy, University of Washington, 3910 15th Ave NE, Seattle, WA, 98195, USA*

²*Department of Physics and Astronomy, University of Pennsylvania, Philadelphia, PA 19104, USA*

³*Cerro Tololo Inter-American Observatory, NSF's National Optical-Infrared Astronomy Research Laboratory, Casilla 603, La Serena, Chile*

⁴*Laboratório Interinstitucional de e-Astronomia - LIneA, Rua Gal. José Cristino 77, Rio de Janeiro, RJ - 20921-400, Brazil*

⁵*Fermi National Accelerator Laboratory, P. O. Box 500, Batavia, IL 60510, USA*

⁶*Department of Physics & Astronomy, University College London, Gower Street, London, WC1E 6BT, UK*

⁷*Instituto de Astrofísica de Canarias, E-38205 La Laguna, Tenerife, Spain*

⁸*Universidad de La Laguna, Dpto. Astrofísica, E-38206 La Laguna, Tenerife, Spain*

⁹*Institut de Física d'Altes Energies (IFAE), The Barcelona Institute of Science and Technology, Campus UAB, 08193 Bellaterra (Barcelona) Spain*

¹⁰*Hamburger Sternwarte, Universität Hamburg, Gojenbergsweg 112, 21029 Hamburg, Germany*

¹¹*School of Mathematics and Physics, University of Queensland, Brisbane, QLD 4072, Australia*

¹²*Centro de Investigaciones Energéticas, Medioambientales y Tecnológicas (CIEMAT), Madrid, Spain*

¹³*Department of Physics, IIT Hyderabad, Kandi, Telangana 502285, India*

¹⁴*California Institute of Technology, 1200 East California Blvd, MC 249-17, Pasadena, CA 91125, USA*

¹⁵*Kavli Institute for Cosmological Physics, University of Chicago, Chicago, IL 60637, USA*

¹⁶*Instituto de Física Teórica UAM/CSIC, Universidad Autónoma de Madrid, 28049 Madrid, Spain*

¹⁷*Institut d'Estudis Espacials de Catalunya (IEEC), 08034 Barcelona, Spain*

¹⁸*Institute of Cosmology and Gravitation, University of Portsmouth, Portsmouth, PO1 3FX, UK*

¹⁹*Institute of Space Sciences (ICE, CSIC), Campus UAB, Carrer de Can Magrans, s/n, 08193 Barcelona, Spain*

²⁰*Center for Astrophysical Surveys, National Center for Supercomputing Applications, 1205 West Clark St., Urbana, IL 61801, USA*

²¹*Department of Astronomy, University of Illinois at Urbana-Champaign, 1002 W. Green Street, Urbana, IL 61801, USA*

²²*Santa Cruz Institute for Particle Physics, Santa Cruz, CA 95064, USA*

²³*Center for Cosmology and Astro-Particle Physics, The Ohio State University, Columbus, OH 43210, USA*

²⁴*Department of Physics, The Ohio State University, Columbus, OH 43210, USA*

²⁵*Center for Astrophysics | Harvard & Smithsonian, 60 Garden Street, Cambridge, MA 02138, USA*

²⁶*Australian Astronomical Optics, Macquarie University, North Ryde, NSW 2113, Australia*

²⁷*Lowell Observatory, 1400 Mars Hill Rd, Flagstaff, AZ 86001, USA*

²⁸*Jet Propulsion Laboratory, California Institute of Technology, 4800 Oak Grove Dr., Pasadena, CA 91109, USA*

²⁹*George P. and Cynthia Woods Mitchell Institute for Fundamental Physics and Astronomy, and Department of Physics and Astronomy, Texas A&M University, College Station, TX 77843, USA*

³⁰*LPSC Grenoble - 53, Avenue des Martyrs 38026 Grenoble, France*

³¹*Institució Catalana de Recerca i Estudis Avançats, E-08010 Barcelona, Spain*

³²*Department of Astrophysical Sciences, Princeton University, Peyton Hall, Princeton, NJ 08544, USA*

³³*Kavli Institute for Particle Astrophysics & Cosmology, P. O. Box 2450, Stanford University, Stanford, CA 94305, USA*

³⁴*SLAC National Accelerator Laboratory, Menlo Park, CA 94025, USA*

³⁵*Department of Physics, Northeastern University, Boston, MA 02115, USA*

³⁶*Instituto de Física, UFRGS, Caixa Postal 15051, Porto Alegre, RS - 91501-970, Brazil*

³⁷*Physics Department, Lancaster University, Lancaster, LA1 4YB, UK*

³⁸*Computer Science and Mathematics Division, Oak Ridge National Laboratory, Oak Ridge, TN 37831*

³⁹*Department of Physics, University of Michigan, Ann Arbor, MI 48109, USA*

40

⁴¹*Department of Astronomy, University of California, Berkeley, 501 Campbell Hall, Berkeley, CA 94720, USA*

⁴²*Lawrence Berkeley National Laboratory, 1 Cyclotron Road, Berkeley, CA 94720, USA*